UNIVERSITY OF SÃO PAULO
SÃO CARLOS SCHOOL OF ENGINEERING

THIAGO AUGUSTO LODI

Tungsten gallium-phosphate glasses for high energy radiation detection

São Carlos - SP
2023

THIAGO AUGUSTO LODI

Tungsten gallium-phosphate glasses for high energy radiation detection

Revised Version

Doctoral thesis presented to the São Carlos School of Engineering of the University of São Paulo, as a requirement for obtaining the title of PhD in Materials Science and Engineering.

Concentration area: Development, characterization, and application of materials.

Supervisor: Prof. Drª. Andrea S. S. de Camargo Alvarez Bernardez

São Carlos - SP

2023

Catalog card prepared by Patron Service at “Prof. Dr. Sergio Rodrigues Fontes Library” at EESC/USP

Lodi, Thiago Augusto
L823f Tungsten gallium-phosphate glasses for high energy radiation detection / Thiago Augusto Lodi; advisor Andrea S. S. de Camargo Alvarez Bernardez. -- São Carlos, 2023.

Doctoral (Thesis) – Graduate Program in Materials Science and Engineering and Concentration area in Development, characterization, and application of materials. -- São Carlos School of Engineering, at University of São Paulo, 2023.

1. Gallium phosphate glasses. 2. Tungsten. 3. Scintillators. 4. Tb^{3+}. 5. Broadband emission. I. Título.

Prepared by Eduardo Graziosi Silva- CRB-8/8907

FOLHA DE JULGAMENTO

Candidato: Bacharel **THIAGO AUGUSTO LODI.**

Título da tese: "Vidros tungstênio gálio-fosfato para detecção de radiação de alta energia".

Data da defesa: 03/10/2022.

Comissão Julgadora	**Resultado**
Profa. Associada **Andréa Simone Stucchi de Camargo Alvarez Bernardez (Orientadora)** (Instituto de Física de São Carlos/IFSC-USP)	Aprovado
Prof. Dr. **Marco Aurélio Cebim** (Universidade Estadual Paulista "Júlio de Mesquita Filho"/UNESP-Araraquara)	Aprovado
Prof. Dr. **Gael Yves Poirier** (Universidade Federal de Alfenas/UNIFAL)	Aprovado
Prof. Dr. **Eduardo Bellini Ferreira** (Escola de Engenharia de São Carlos/EESC-USP)	Aprovado
Prof. Dr. **Luiz Gustavo Jacobsohn** (Clemson University/Estados Unidos)	Aprovado

Coordenador do Programa de Pós-Graduação em Engenharia de Materiais:
Prof. Associado **Rafael Salomão**

Presidente da Comissão de Pós-Graduação:
Prof. Titular **Murilo Araujo Romero**

To my wife Ludimila for her patience, affection, and tireless support.

ACKNOWLEDGMENTS

First of all, I would like to express my deepest appreciation to my supervisor Prof. Dr. Andrea de Camargo for having me in her laboratory, and for her patience and guidance during this journey.

This study was financed in part by the Coordenação de Aperfeiçoamento de Pessoal de Nível Superior – Brasil (CAPES) – Grant Finance Code 001. Additionally, this endeavor would not have been possible without the financial support from the Brazilian research funding agencies CNPq and FAPESP.

I would like to extend my sincere thanks to the University of São Paulo, to São Carlos School of Engineering, and São Carlos Institute of Physics. Thanks should also go to Postgraduate Program in Materials Science and Engineering.

Special thanks to Prof. Dr. Hellmut Eckert, Prof. Dr. Tomaz Catunda, Prof. Dr. Luiz G, Jacobsohn, Prof. Dr. Marcos de O. Junior, Prof. Dra. Silvia H. Santagneli, Prof. Dr. Valmor R. Mastelaro, Dra. Jéssica F.M. dos Santos and Dr. Leonnam G. Merízio for their support in this project.

Words cannot express my gratitude to Dr. Gustavo Galleani. Thank you so much for the support, patience, and knowledge shared with me.

I would like to thank my friends, lab mates, colleagues and research team - Iago, Gabriel, Gustavo, Leonnam, Marylyn, Raquel, Pedro, Vinicius, Vitor and Walter - for the cherished time spent together in the lab, and in social settings.

I am very grateful to my friends Luana and Gustavo and also to my feline niece, Susie, for their love, support and bad movies on weekends.

I would like to express my gratitude and appreciation for Dr. Alysson Steimacher and by Dr. Franciana Pedrochi, whose guidance, support and encouragement in my first steps at the academy got me this far.

I would be remiss in not mentioning my family, especially my parents and brothers. Their belief in me has kept my motivation during all these years as a cientist (yes, a cientist).

And my biggest thanks to my wife Ludimila for all the support you have shown me through this research, without which I would have stopped these studies a long time ago. You have been amazing, and I will now organizer all plants of the room as I promised! I love you, sunshine!

"Life is not easy for any of us. But what of that? We must have perseverance and above all confidence in ourselves. We must believe that we are gifted for something and that this thing must be attained."

Marie Curie

RESUMO

LODI, T. A. **Vidros tungstênio gálio-fosfato para detecção de radiação de alta energia**. 115p. 2023. Tese (Doutor) – Escola de Engenharia de São Carlos, Universidade de São Paulo, São Carlos, 2022.

Cintiladores são materiais que convertem um único fóton de radiação ionizante de alta energia, como raios-X, raios γ, nêutrons, partículas α e β, em fótons UV-visíveis. Os detectores de cintilação, que geralmente consistem em um cintilador e um fotodetector, têm desempenhado um papel importante em aplicações de detecção de radiação, como em imagens industriais e médicas, segurança interna e experimentos de física de alta energia. Para ser usado como cintilador, um material deve conter centros luminescentes que são extrínsecos, quando dopados com íons ativos, como os íons trivalentes de terras raras, ou intrínsecos, quando a emissão se origina de centros moleculares ou defeitos de rede. Normalmente, os cintiladores são monocristais inorgânicos devido à sua alta densidade e excelente eficiência de emissão. No entanto, a síntese desses materiais, em tamanhos e formatos limitados, é extremamente custosa e demorada, dificultando a produção industrial em larga escala de mercado. Alternativamente, materiais de baixo custo que oferecem maiores possibilidades de moldagem, como vidros, têm sido investigados nesta aplicação. O vidro é um material extremamente versátil que, em geral, proporciona uma produção econômica e em larga escala, sendo facilmente processado em geometrias complexas, incluindo fibras ópticas especiais. Este projeto de doutorado teve como foco o desenvolvimento de vidros no sistema composicional $NaPO_3$-Ga_2O_3-Na_2WO_4 e sua caracterização detalhada do ponto de vista térmico, estrutural, espectroscópico e óptico, tendo em vista sua promissora aplicação como cintiladores. Os vidros foram obtidos com excelente qualidade óptica, muito boa estabilidade química e térmica, e foram caracterizados por Calorimetria de Varredura Diferencial (DSC), medidas de densidade volumétrica, difração de raios X, espectroscopia Raman, Ressonância Magnética Nuclear (RMN), Infravermelho por Transformada de Fourier (FT-IR), espectroscopia de fotoelétrons de raios-X (XPS), absorção UV-Vis, fotoluminescência (emissão e excitação) e radioluminescência. A robustez dos materiais associada à sua ótima resposta espectroscópica, óptica e radioluminescente indicam que são materiais promissores para dispositivos cintilantes, merecendo mais investigações e desenvolvimentos.

Palavras-chave: Vidros gálio-fosfato. Tungstênio. Cintiladores. Tb^{3+}. Emissão de banda larga.

ABSTRACT

LODI, T. A. **Tungsten gallium-phosphate glasses for high energy radiation detection**. 115p. 2023. Thesis (Doctor) – São Carlos School of Engineering, University of São Paulo, São Carlos, 2022.

Scintillators are materials that convert a single photon of high-energy ionizing radiation, like X-rays, γ-rays, neutrons, α and β particles, into UV-visible photons. Scintillation detectors, which usually consist of a scintillator and photodetector, have played an important role in radiation detection applications, such as in industrial and medical imaging, homeland security and high energy physics experiments. In order to be used as a scintillator, a material must contain luminescent centers which are either extrinsic, when doped with active ions such as the trivalent rare-earth ions, or intrinsic, when the emission originates from molecular centers or lattice defects. Typically, scintillators are inorganic single-crystals due to their high density and excellent emission efficiency. However, the synthesis of these materials, in limited sizes and shapes is extremely costly and time-consuming, hindering industrial production in large market scale. Alternatively, lower-cost materials which offer larger possibilities of shaping, such as glasses, have been investigated this application. Glass is an extremely versatile material that in general provides cost-effective, large-scale production, being easily processed into complex geometries, including special optical fibers. This doctorate project was focused on the development of glasses in the compositional system $NaPO_3$-Ga_2O_3-Na_2WO_4 and their detailed characterization from the thermal, structural, spectroscopic and optical viewpoints, in view of their promising application as scintillators. The glasses were obtained with excellent optical quality, very good chemical and thermal stability, and they were characterized by Differential Scanning Calorimetry (DSC), volumetric density measurements, X-ray diffraction, Raman spectroscopy, Nuclear Magnetic Resonance (NMR), Fourier Transform Infrared (FT-IR), X-ray photoelectron spectroscopy (XPS), UV-vis absorption, photoluminescence (emission and excitation) and radioluminescence. The robustness of the materials associated to its optimum spectroscopic, optical and radioluminescent response indicate that they are promising materials for scintillating devices, worth of further investigation and developments.

Keywords: Gallium phosphate glasses. Tungsten. Scintillators. Tb^{3+}. Broadband emission.

LIST OF FIGURES

LIST OF TABLES

SUMMARY

1 INTRODUCTION

Driven by advances in diagnostic medicine, growth in the number of nuclear power plants, as well as increasing investment in defense and national security, the development of the field of inorganic scintillators have increased considerably worldwide. It is estimated that the global inorganic scintillator market in 2022 will move approximately US$ 300 million, and could reach the US$ 385 million mark by the end of 2027 [1]. The growing popularity of inorganic scintillators can be explained by the diversity of requirements and applications enabled by these materials. Although some scintillating materials, such as the $Bi_4Ge_3O_{12}$ (BGO) crystal, present excellent performance in the detection of gamma rays (γ), some applications prioritize other requirements, such as the detection of X-rays and neutrons, for example [2].

Research aimed at the development of inorganic scintillators is still mostly focused on the use of single crystals, which present superior characteristics, such as high conversion efficiency and energy resolution. Although a large portion of the scintillator market is occupied by these materials, their fabrication process remains expensive, time-consuming and limiting in terms of the size and shape of the final product [3,4]. These limitations have triggered the interest for the development of scintillating glasses, which may constitute an alternative with lower cost production and easier manufacturing in different sizes and shapes (fibers, for example), in addition to allowing the incorporation of activator ions in high concentrations. [5,6]. Despite sharing properties similar to plastic scintillators, glass scintillators can exhibit higher densities, as well as superior thermal, mechanical, and chemical stability[7].

Intrinsic inorganic scintillators, either natural or synthetic, are those in which the luminescence involves ions or chemical groups that compose the scintillator material. The emission of extrinsic scintillators, on the other hand, originates from dopant ions, typically lanthanides, involving *f-f* and *f-d* transitions, such as Tb^{3+}, $Eu^{2+,}$ and Ce^{3+}. This doctorate project focused on the synthesis, structural, thermal, and optical characterization of a gallium-phosphate glass system doped with the transition metal W^{6+} and the lanthanide Tb^{3+}, which meets the basic requirements for application as a scintillator material, offering an additional alternative to monocrystalline scintillators.

1.1 Glass and glass transition (Tg)

Glasses can be considered one of the most versatile materials for the solution of several problems faced by humanity. The scientific progress on vitreous materials, such as the development of new compositions and synthesis technologies, has increased even more their applications span. Areas such as medicine, energy, and security have benefited immensely with the advent of biocompatible glasses [3], solid-state batteries [4], and the use of glasses for the storage of nuclear waste [5], for instance.

During the last two centuries, various definitions of glasses have been proposed and they are constantly evolving. It is however a common sense that glasses are amorphous materials, which do not exhibit long-range periodicity, and which present a glass transition phenomenon [6]. The most recent definition for glass was proposed by Zanotto, E. D and Mauro, J. C, in the article entitled *The glassy state of matter: Its definition and ultimate fate* [7], in which the authors define the material as "[…] a non-equilibrium, non-crystalline condensed state of matter that exhibits a glass transition. The structure of glasses is similar to that of their parent supercooled liquids (SCL), and they spontaneously relax toward the SCL state. Their ultimate fate is to solidify, i.e., crystallize". In addition to this definition, in this work, it is also possible to find other definitions for glassy materials.

One of the simplest ways to understand the formation and some of the main characteristics of glasses is through the enthalpy versus temperature diagram, as shown in Figure 1, where it is also possible to observe the difference in obtaining a crystalline and a non-crystalline solid. Liquids, when in equilibrium, exist only above the melting temperature (T_m) (line AB), being unable to crystallize in this region. When cooled from point B, two distinct phenomena can occur. For a slow cooling rate, the material in the liquid state will be subject to a crystallization process starting from the melting temperature (Tm). From this moment on, the enthalpy undergoes a significant reduction (line BC), followed by a reduction in temperature (line CD), resulting in a crystalline solid. If cooled at a relatively rapid rate, the material will behave differently since the crystallization process will no longer occur below Tm. In this case, the material passes from the liquid state to a supercooled liquid state (line BD), and as its temperature shifts in the B → E direction, its viscosity increases. As a consequence of the increasing viscosity, the rotational movements of the molecules become more limited until, when reaching the glass transition range, a sudden change in the material causes these

movements to be blocked. Both paths, EF or EG, represent a non-crystalline solid, and they only differ from each other in terms of the cooling rate to which they will be subjected.

Figure 1. Enthalpy versus temperature diagram for crystalline and non-crystalline solid formation, highlighting the regions of liquid, supercooled liquid, crystalline solid, and non-crystalline solid. Tg = glass transition temperature.

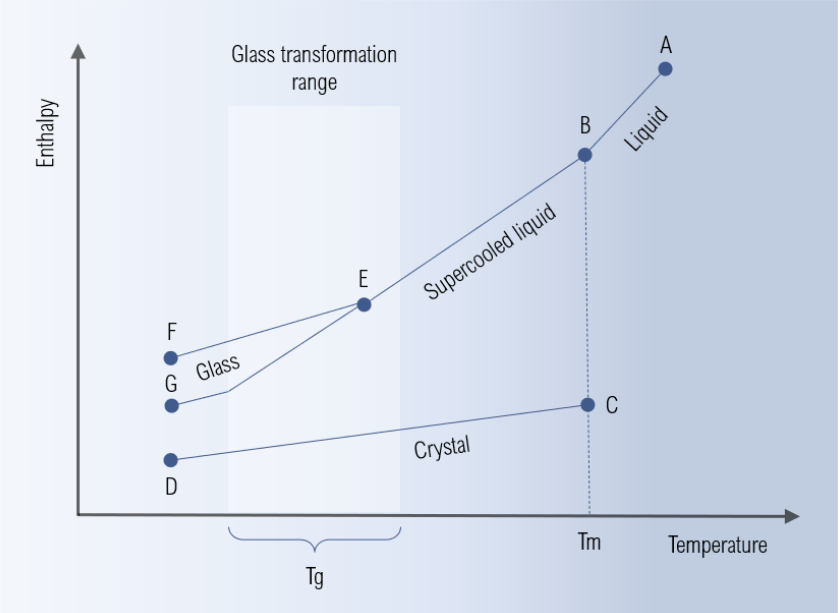

Source: Adapted from [7].

When referring to glassy materials for special applications, the chemical composition of the material plays a pivotal role in its final properties. The precursor materials used in the production of glasses are commonly divided into three categories: network formers, network modifiers, and intermediate species [8]. The network formers are considered the backbone of the network and can form glasses via common techniques. These precursors comprise the oxides B_2O_3, SiO_2, GeO_2, P_2O_5, As_2O_5, Sb_2O_5 and V_2O_5, among others. The first four are especially important and present in the manufacturing of comercial glasses. The modifying elements, in turn, are introduced into the glass matrix in order to modify its properties, such as reducing the melting temperature, for example. Among the main network modifiers are Na_2O, K_2O, CaO, SrO, BaO, and Ga_2O_3. The intermediate elements occupy the position between formers and modifiers, namely Al_2O_3, BeO, ZnO, CdO, PbO, TiO_2, among others [9].

1.2 Phosphate glasses

It is very common for glasses to be classified in groups or families, defined by their matrix composition. For instance the silicate glass family is composed of silicon dioxide (SiO_2), the borate glass family is mainly formed by boron oxide (B_2O_3) and derivatives and so on for phosphates, germanates, tellurites glasses, among others. These families differ from each other in physical and chemical properties, offering a large variety of application possibilities. Particularly, the phosphate family is of high technological relevance and is largely present in medical, photonic, and nuclear applications [10,11]. With the discovery of biocompatible glasses and glass-ceramics, systems containing phosphorus pentoxide (P_2O_5) as a forming element have been widely studied due to their high solubility in aqueous media which allows a controlled degradation rate required in applications such as tissue regeneration and engineering [12,13]. In the nuclear energy industry, phosphorus-based glasses are being studied as an alternative to borosilicate glasses in the storage of high-level nuclear radioactive waste [5,14].

At LEMAF, the Laboratory of Spectroscopy of Functional Materials, phosphate glasses have been studied for more than 15 years for applications that range from near-infrared laser active media to solid-state lighting and color displays [15–18]. More recently, efforts have been devoted to the study of these glasses as high energy radiation detectors. In addition to the very good glass-forming ability, low glass transition and melting temperatures, and good resistance to radiation when compared to silicate glasses, for example, phosphate glasses have desirable optical properties, such as the capacity to incorporate higher concentrations of rare earth (RE) ions than silicates and borates, and high transmittance in the ultraviolet (UV) region [19–23].

Phosphate glasses are organized into basic units of phosphorus tetrahedra (PO_4), resulting from the formation of sp^3 hybrid orbitals by the external P electrons ($3s^2\ 3p^3$). Each PO_4 tetrahedron is connected to the structure by sharing at most three of the four available vertices, through hydrogen bonds, since a double bond (P=O) is present in the structure [22,24]. Tetrahedrons are classified, in terms of connectivity, using Q^s terminology, where *s* can assume the values of 0, 1, 2, and 3, according to the number of shared vertices, as seen in Figure 2. For tetrahedra with three oxygens linked to phosphorus via a single bond, a Q^3 structure is formed. If only 2 oxygens are linked by single bonds, the structure is called Q^2, and so on. The oxygens of a PO_4 tetrahedron not bonded to another phosphorus are called terminal oxygens or non-bridging oxygens (NBO, or O_{NB}), while the P-O-P bond oxygens responsible for connecting the tetrahedra are known as bridged or bridging oxygens (O_B) [24,25].

Figure 2. Tetrahedral phosphate units in glasses.

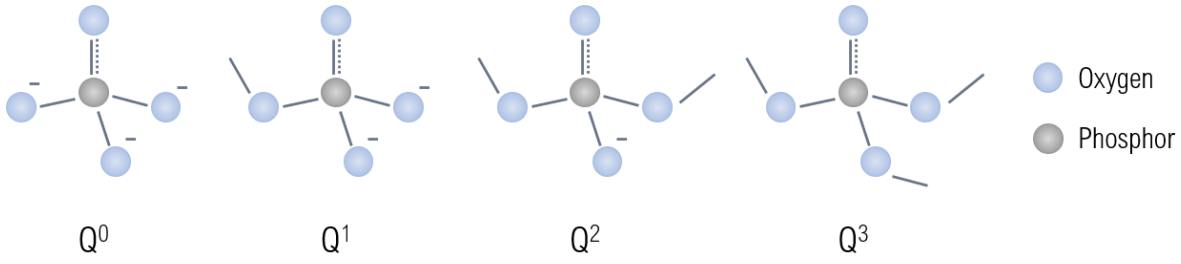

Source: Adapted from [26].

In the same way that water solubility is desirable for some applications, as mentioned above, the hygroscopicity of phosphate glasses can become a disadvantage for others. The low chemical durability attributed to phosphate glasses is due to the hydrophilic functional group – P = O that participates in the basic units of formation of these glasses [25,27–29]. However, the inconvenience of the hygroscopicity of these glasses can be overcome with the introduction of modifying and intermediate elements, which can alter the structure of the chains and drastically change the physical and chemical properties of the glass. The improvement of the chemical durability of phosphate glasses through the introduction of heavy metal oxides in the vitreous network has been the subject of numerous researches [11,28,30].

As previously described, the gallium element is classified, according to Sun, K. [29], as a network modifier. Considered a heavy metal oxide, when introduced into the glass matrix, Ga_2O_3 can influence several physical and chemical properties, such as the refractive index, the infrared transmission, the thermal expansion coefficient, the chemical durability, the glass transition temperature and the volumetric density, among others.

In addition to gallium oxide, the addition of transition metals in the vitreous network can promote interesting modifications from a technological point of view. Belonging to the 6th period of the periodic table, tungsten (W), is also classified as a network modifier element. The incorporation of tungsten atoms in the network confers interesting thermal, chemical, mechanical and optical properties. De Araujo, et al [31] observed that the addition of tungsten oxide in phosphate glasses improves the thermal stability as well as its chemical resistance. Another class of elements that act as network modifiers, attaining special characteristics to glasses are the lanthanide and transition metal ions, which will be discussed in the next section.

1.3 Lanthanide and transition metal ions

The rare-earth (RE) elements, according to the IUPAC classification [32], are a group of 15 chemical elements of the lanthanide series (elements with atomic number Z from 57 to 71), and two members of the IIIB group, Scandium and Yttrium due to their similarity in chemical behavior. The electronic configuration of these elements is based on the Xenon noble gas configuration $[Xe]6s^2 5d^1 4f^{n-1}$ or $[Xe]6s^2 4f^n$, with n = 1 to 14. The most common oxidation state for the rare earth ions is trivalent, forming the $TR_2^{3+}O_3^{2-}$ oxides. Some elements such as cerium (Ce), praseodymium (Pr), terbium (Tb), europium (Eu), and ytterbium (Yb) can present 2+ and 4+ oxidation states, however, these states are less stable compared to the trivalent.

Among the 17 elements classified as rare earth, only 13 of them (from Ce^{3+} to Yb^{3+}) are optically active, presenting absorption bands from ultraviolet (UV) to infrared (IR), due to intraconfigurational 4f - 4f transitions. The elements scandium (Sc) and yttrium (Y) are optically inactive, since their incomplete subshells are 3d and 4d, which can take part in chemical bonds. On the other hand, the elements La and Lu are considered optically inactive because they do not present electrons in the 4f subshell or have it completely filled, respectively.

Knowing that the $5s^2$ and $5p^6$ layers are completely filled according to the Pauli principle and have an average radius greater than the 4f layer, the electrons of the latter are shielded by the external layers, causing them to have little interaction with the chemical environment around the RE^{3+} ions. Because of this relative insensitivity to the host matrix environment, the spectra of RE ions translates into a “fingerprint” with very little variations in wavelength. The energy levels of the 4f electrons of RE^{3+} ions have been conveniently presented by Carnall et al.[33].

As previously mentioned, the absorption and emission bands of RE ions come from 4f-4f transitions, i.e., transitions between states of the same configuration. Therefore, they are forbidden by electric dipole mechanism, according to Laporte's rule [34]. For this reason, their corresponding bands are narrow, of lower intensity, and the excited states present longer luminescence decay lifetime, as compared to the allowed 4f-5d transitions. The reason they are observed, lies in the strong spin-orbit coupling in the RE ions which relaxes the parity rule of Laporte yielding transitions by the so-called “forced electric-dipole” mechanism [34].

Initially, spectroscopic studies of rare-earth ions were mostly carried out in crystalline hosts, with narrow absorption and emission bands. Since the 1950’s, however, and particularly after the 1960’s with the advent of the laser, the increased practical interest in materials of amorphous (or glassy) nature has reversed this situation. In these materials, the embedded RE ions present inhomogeneously broadened absorption, excitation and emission bands due to a

distribution of different chemical environments at their siting. In other words, since glassy lack long-range structural order and periodicity, the active ions experiencing distinct neighborhood, undergo different perturbation of the free ion Hamiltonian, generating sets of energy levels that are separated by small energy values, so that the observed bands result from a convolution of such contributions. Rather than being a disadvantage, the spectral broadening actually broadens the application of glasses in the field of photonics and optoelectronics, in broadband amplifiers, video devices, sensors, high-density optical memory devices, light-emitting diodes (LEDs), etc. [32]

In this project we have focused on the study of Tb^{3+} doped glasses because this ion fulfils the technological need for intense emission in the green spectral region [35]. The most intense emission of Tb^{3+} is centered at approximately 545 nm (green), however, emissions in the blue, yellow, and orange can also be observed. These four emissions are assigned to transitions from the $^5D_4$ excited state to the lower energy lying ^7F_J states (J = 6, 5, 4, and 3). As the $^5D_4 \rightarrow {}^7F_5$ transition is predominant over the other emissions, the luminescence of the Tb^{3+} ion is usually green to the naked eye [15].

Another luminescent center explored in this work was tungsten. Isolated in 1781 by Scheele and Bergmann from a mineral known as scheelite ($CaWO_4$), the tungsten element occurs in the scheelite and wolframite form, and their complexes, which have a formally empty *d* shell yielding often intense broad-band emission in the visible region of the electromagnetic spectrum. $CaWO_4$, scheelite crystal structure is well known for its intense luminescence in the visible region. For 75 years it was one of the most expressive commercial scintillators used in X-ray photography as an intensifying screen. This is mainly due to its excellent ability to absorb X-rays and convert them into radiation. However, the SrWO4 crystal, which like $CaWO_4$ has a scheelite structure, does not exhibit luminescence at room temperature. Thus, the challenge in developing these tungstates for applications in optoelectronic devices such as LEDs, lasers, and/or scintillators, has become the object of study of numerous research laboratories[36].

1.4 Radiation and radiation detectors

The physical phenomenon of radiation can be understood as energy in transit, that is, the propagation of a particle or electromagnetic wave from one point to another in space. Radiation can be categorized in different ways, as to the source, the type (ionizing and non-ionizing) and the effects induced by it [37].

When interacting with matter, radiation communicates with atoms and molecules by exchanging energy with them. This exchange can result in different phenomenon such as scattering, absorption, excitation or ionization. When the energy is transferred in a sufficient way to strip an electron from its original atom or molecule resulting in the creation of a pair of ions, the energy is said to have been transferred by ionization. Energy transfer by excitation, in turn, occurs when electrons, previously in their original arrangement, are promoted to an excited orbital state. Both processes are explored in the construction of radiation detectors, however, as it is more commonly used, the transfer of radiation by ionization is responsible for the term "ionizing radiation", often used to refer to emissions from radioactive materials [2,37].

As for the type, radiation can be classified as ionizing and non-ionizing. Non-ionizing radiation is of low-energy and incapable of removing an electron from an atom or molecule. This type of radiation includes radio waves, microwaves, infrared, visible, and soft ultraviolet, which are located on the left side of the electromagnetic spectrum schematized in Figure 3, with energies below 10^2 eV. Ionizing radiation, in turn, has enough energy to ionize atoms and molecules, being able to strip electrons from them. The minimum energy for this type of radiation is approximately 10 eV.

Figure 3. Schematic electromagnetic spectrum highlighting ionizing and non-ionizing radiation. The wavelengths and energy values scale shows approximated values.

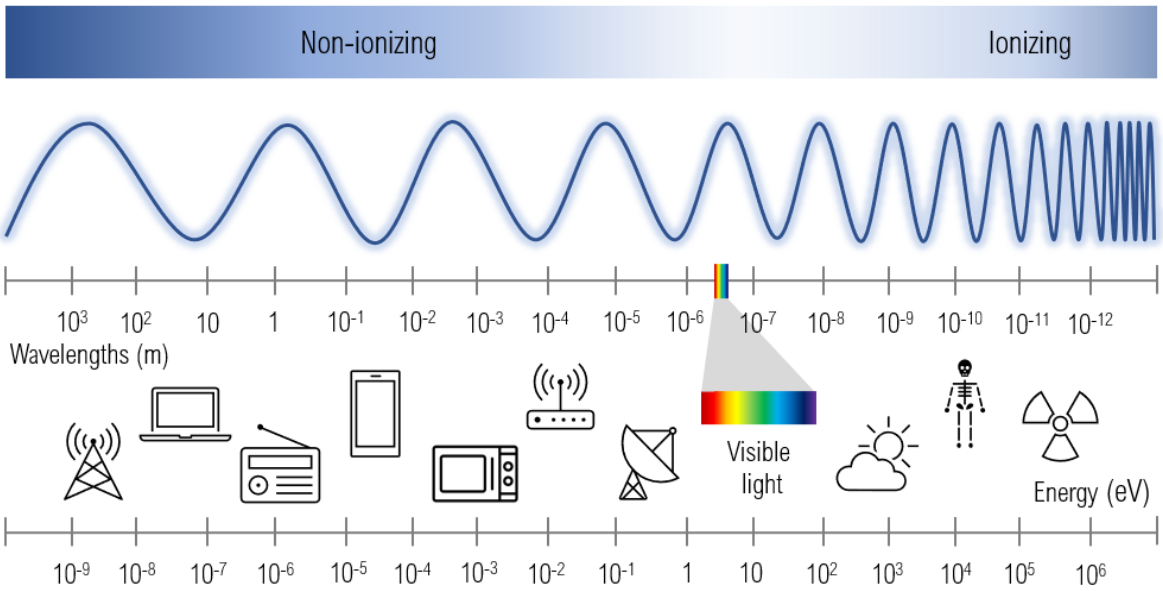

Source: Adapted from [2].

The first event of detection of ionizing radiation dates from November 1895, when the German physicist and engineer Wilhelm Röntgen, while carrying out experiments with Crookes tubes, earlier used in the discovery of cathode rays, noticed that when using a piece of cardboard covered with Barium platinocyanide [$(BaPt(CN)_4$] a greenish light was observed [38,39]. This observation rose the interest of Röntgen, who later covered the entire tube with a casing reflective to visible light, concluding that the tube itself was responsible for the generation of a new type of radiation, which he decided to call “ X-ray". After the discovery, Röntgen started a series of new experiments, among them replacing a fluorescent screen with a photographic plate susceptible to X-rays. In this experiment, the physicist took what is now one of the most interesting images in science, an image of his wife's hand (Figure 4). At this moment, radiography was born and six years later, in 1901, Röntgen received the first Nobel Prize in Physics for his findings [38].

Figure 4. Wilhelm Roentgen's x-ray photograph of his wife's hand in 1896.

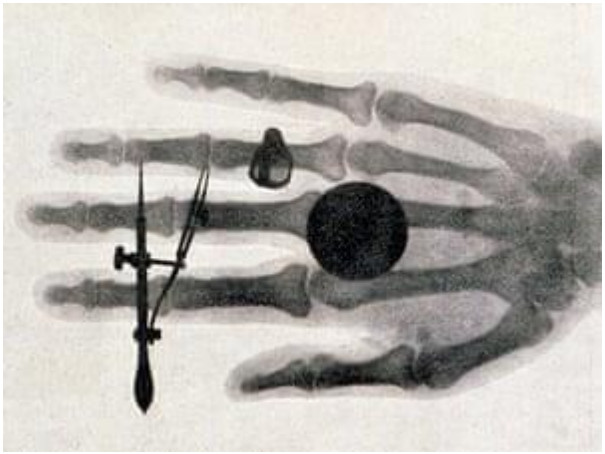

Source: [40]

Driven by Röntgen's studies, the French physicist Antoine-Henri Becquerel, in 1896, accidentally discovered, while studying uranium compounds, that the rays emitted by the element were able to penetrate and be detected by photographic plates. It was later understood that this phenomenon was not caused by the newly discovered X-ray, but by another type of radiation, gamma radiation (γ). Based on these discoveries, investigations began for the development of devices capable of detecting those new forms of radiation [2].

Radiation detection generally occurs through the loss of energy to the detector material, i.e. a high energy particle must interact with the material used for detection, transferring energy to it. This same mechanism supports the principles of gas detectors, semiconductors, organic

and inorganic detectors [41]. As previously mentioned, ionizing radiation has enough energy to strip electrons from atoms and molecules, and as long as this energy exceeds the ionization potential of a given gas, it can be used as a detector of ionizing radiation.

Gas detectors respond to radiation by passing electrical currents induced by ionization. A typical gas detector consists of a volume of gas contained between two electrodes (cathode and anode) that have a voltage difference between them. Under normal circumstances, the gas acts as an insulating material, however, when irradiated, it causes electrons generated by ionization to be attracted to the anode and ionized atoms to the cathode. This phenomenon results in a momentary flow of electric current that is capable of providing information about the analyzed radiation, such as energy and intensity [42]. Among the main gas, detectors are ionization chambers, proportional counters, and Geiger-Müller (GM) counters [42,43]. In general, gas detectors have proved to be extremely useful in numerous applications, however, some factors limit their applications. The GM counter, developed around 1913 by Hans Geiger and later improved by Geiger and Walther Müller, for example, is a simple, robust and inexpensive detector, however, nowadays, for most applications, they are replaced by other types of detectors, once they have low detection efficiency for X and γ rays [42].

Featuring a detection mechanism similar to that of a gas detector, liquid detectors make use of liquid noble gases and have some advantages over gas detectors, such as good energy absorption due to high density, high spatial resolution, and the possibility of being used in large volumes, resulting in a relatively low cost [2,41].

Another class of detectors for ionizing radiation detectors is semiconductor-based. Because the solid materials used in this type of detector have a density of up to 5000 times greater than that of gases, semiconductor detectors exhibit high stopping power, which makes them very efficient in detecting X-rays and γ-rays. The main representatives of this class of detectors are silicon (Si) and germanium (Ge).

By way of comparison, semiconductor-based detectors are not only more efficient in absorbing radiation, but also in producing an electrical output signal ten times greater than a gas detector. Despite their advantages, semiconductor detectors have disadvantages that may limit their use, such as the presence of a background signal from the electric current induced by room temperature and the presence of impurities that disturb the arrangement of atoms in the matrix [2,42].

1.5 Scintillation detectors

As previously mentioned, radiation detector devices can make use of mainly two distinct mechanisms, ionization or excitation. Unlike the detectors mentioned above, in some materials subjected to the absorption of radiation, part of the energy can be released in the form of visible light in the decay process. These materials are called scintillators, and detectors built based on them are commonly called scintillation detectors or just scintillators [37].

The process of detecting radiation through scintillation involves complex mechanisms but it can be generally simplified into four basic steps outlined in Figure 5 [2,44]:

i. Interaction of radiation with matter, that is, with the scintillating material;
ii. Energy transfer to the luminescent center;
iii. The luminescent center relaxes from the excited state to the ground state, resulting in the emission of photons;
iv. The signal is detected by a photodetector.

When the high-energy particle interacts with a scintillating material, it can generate an electron-hole pair. The multiplication of these electrons and holes occurs through radiative decay (secondary X-rays), non-radiative decay (Auger processes), in addition to electron-electron inelastic scattering. This first stage is known as Absorption/multiplication. When the electrons and holes generated in the previous step dissipate their kinetic energy through interactions with the lattice or with other electrons, they thermalize to the lower part of the conduction band and upper part of the valence band, respectively.

In the second stage, known as Transport, the energy of the carriers must migrate before the recombination or being transferred to the luminescent center, since the radiation absorption site, in most cases, does not coincide with the dopant site.

The third and final stage is called relaxation/emission when the luminescent center, already in its excited state, releases its energy through non-radiative processes, or in the form of a low-energy photon [44,45]. In the case of intrinsic scintillators, the direct recombination of electron-hole pairs (excitons) is responsible for the emission, while the extrinsic scintillator depends on an activator that induces an impurity energy level located at the band gap of the host lattice.

Figure 6 shows an illustration of a typical scintillation detector. In general, an ionizing radiation with an energy of the order of keV - MeV reaches the scintillator material, which in turn absorbs the radiation converting it into several visible photons. These photons are detected by a photodetector and later converted into an electrical signal [46].

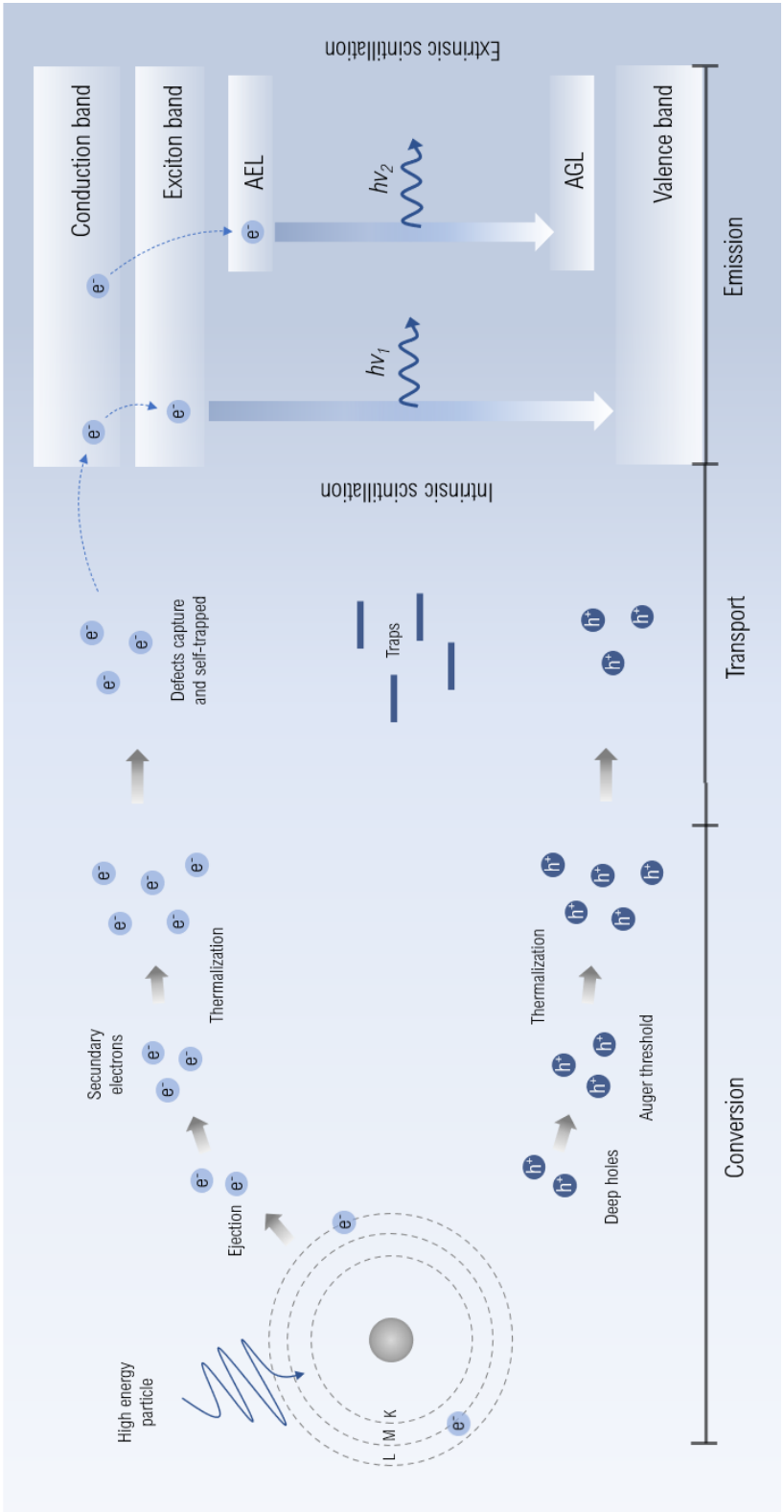

Figure 5. Schematic illustration of the scintillation mechanism in inorganic scintillators. AEL: Activator excited level and AGL: Activator ground level.

Source: Adapted from: [45]

The conversion efficiency of a scintillator is not a very efficient one in the order of 10 to 15%. However, this low conversion efficiency is overcome through the use of high-count photodetectors, such as photomultiplier tubes (PMTs) and photodiodes [2].

Figure 6. Illustration of a typical scintillation detector.

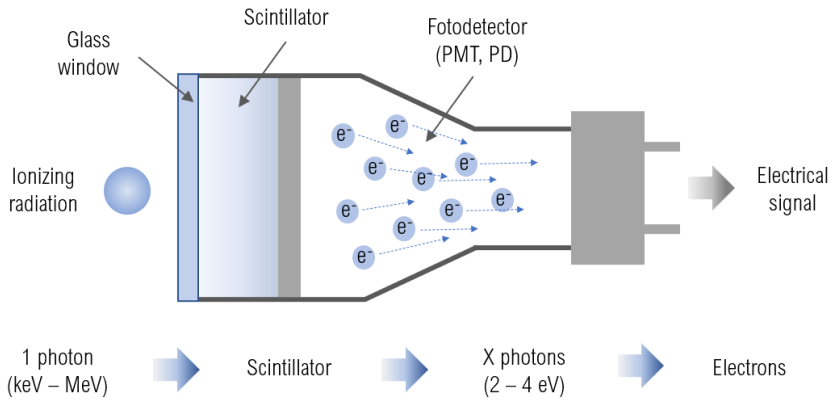

Source: Adapted from [46].

In general, scintillating materials must meet the following requirements:

i. Convert the energy of charged particles into detectable light;
ii. The conversion must be linear, that is, the emitted light must be proportional to the deposited energy;
iii. The material must be transparent at the emission wavelength;
iv. The luminescence decay time must be relatively short;
v. The material must have good optical quality and allow fabrication in various shapes and sizes;
vi. Present a refractive index close to that of silicate glasses (1.5) in order to allow a good coupling between the scintillator material and the photodetector [43].

None of the scintillator materials can satisfy simultaneously all the criteria, and the choice of the ideal material for a given application must take these and other factors into account. Although scintillator materials can come in different forms and types, they are generally divided into two large groups: organic and inorganic scintillators.

Organic scintillators can be solid, liquid or gaseous, which is considered one of their greatest advantages, allowing them to be produced in any geometry and therefore customized for specific applications [2,41].

The fluorescence process in organic scintillators is the result of transitions in the energy levels of a single molecule and can be observed from a given molecular species, regardless of its physical state. This contrasts, for example, with inorganic crystalline scintillators (discussed below), which require a regular crystal lattice as the basis for the scintillation process.

Organic scintillators may also be available in three different forms: plastic, liquid, and crystalline scintillators. Plastic scintillators, one of the main representatives of the organic class, are explored for a variety of applications, mainly in those that require fast decay time.

In addition, because they are considered relatively inexpensive, plastic scintillators are chosen when a large volume of detectors is required. These materials are commercially available in a wide selection of sizes and shapes [43], are chemically stable, and exhibit high optical quality. However, among its main disadvantages are non-linearity in light emission, mechanical instability, and vulnerability to radiation damage [2].

Most inorganic scintillators are crystalline, significantly denser, and have higher atomic numbers when compared to organic scintillators, which makes them attractive for applications that require high stopping power of incident radiation. In addition, these materials, in general, exhibit greater light emission when affected by ionizing radiation [19].

For each application served by inorganic scintillators, different requirements may be desired. However, in general, an ideal scintillator should have fast decay (<100 ns), a high luminous yield (> 40,000 photons/MeV), a high volumetric density (> 6g/cm^3), be easily produced in large volumes and variable shapes, as well as having a low production cost [44].

Table 1 shows the properties of some of the most commonly used inorganic scintillators, two representative glass scintillators (Li (Ce) and Glass:Tb Glass), and a plastic scintillator, for comparison purposes.

Table 1. Properties of some inorganic scintillators, and an organic (plastic) scintillator for comparison. Adapted from [43].

Scintillator	Density ($g.cm^{-3}$)	λ emission (nm)	Refractive index	Lifetime (μs)	Yield (photon/MeV)
NaI:Tl	3,67	415	1,85	0,23	38000
BGO	7,13	480	2,15	0,30	8200
$CdWO_4$	6,1	420	1,94	1,1	15000
GSO (Ce)	6,71	440	1,85	0,056	9000
$LaBr_3$ (Ce)	5,29	380	2,1	0,026	63000
Vidro Li (Ce)	2,64	400	1,59	0,05 - 0,1	3500
Glass:Tb	3,03	550	1,5	3000 - 5000	50000
Plastic Scintillator (NE102A)	1,03	423	1,58	0,002	10000

The thallium-doped sodium iodide crystal [NaI(Tl)] is the main representative of the inorganic scintillator detector class. This status is mainly due to its high light output (approximately 40,000 photon/MeV), emission in the blue region, low cost production and availability in large crystals. These characteristics enable its use in numerous applications such as diagnostic medicine, physics, and environmental sciences. However, the NaI:Tl crystal is highly hygroscopic, requiring that the detector device necessarily be built in a sealed structure, that is, protected from humidity [2].

The $B_4Ge_3O_{12}$ crystal, commonly abbreviated as BGO, has a high density (7.13 $g.cm^{-3}$) and higher absorption efficiency when compared to other scintillating crystals devoted to detection of γ radiation. Furthermore, the BGO crystal does not have the drawback of hygroscopicity presented by NaI:Tl. However, its luminous efficiency is only 10-20% compared to the latter [2,43].

The Ce-doped GSO (Gd_2SiO_5) and LaBr3 crystals share properties such as fast decay, however, they have lower light yield and are relatively more expensive than NaI:Tl. It is also worth mentioning that $LaBr_3$ has a higher hygroscopicity than NaI:Tl [2,47].

It is possible to observe that even the most commercially used scintillators exhibit at least one undesirable property. NaI:Tl is highly hygroscopic and has a low density. BGO and GSO exhibit low light output. Despite these shortcomings, each of these scintillators discussed above has achieved large commercial success, which highlights the breadth of requirements and variety of applications these materials can meet.

The majority of inorganic scintillators are produced using crystal growth techniques such as Bridgman and Czochralski. Both methods are based on melting the precursor reagents followed by pulling the melt (Czochralski) or slow cooling (Bridgman) [48]. The major disadvantage of these methods is the slowness since the crystal pulling rate does not exceed a few millimeters per hour, making the final product very expensive [37]. It is in this regard that the more facile, lower cost production of glasses comes at hand.

1.6 Glass scintillators

The interest in glasses as a scintillating material dates back to the late 1950s, when independent works began to be developed by researchers Anderson [49] in the United Kingdom, Ginther [50][51] in the USA, among others. The main objective of most of these studies was the detection of thermal neutrons. To this end, numerous silica-based glasses, as well as several dopants were studied, until reaching a composition based on SiO_2, MgO, Al_2O_3 and LiO_2, doped with Ce_2O_3, which exhibited a reasonable luminous yield, ten times greater than a previously developed phosphate glass doped with the same Ce^{3+} content [19]. These preliminary studies triggered the development of numerous commercial glass scintillators, such as the GS1/2/3 and GS10/20/30 series, commercialized by the largest scintillator materials industries.

Another series of commercially available scintillating glasses is the KG1/2/3, which was based on the work of Coceva [52]. As with the GS series, the glasses studied by Coceva belong to the silicate glass family, however, they do not contain aluminum and magnesium and have higher concentrations of lithium.

Although scintillating glasses were initially developed for the detection of neutrons, the research soon expanded to include detection of other types of ionizing radiation, such as X-rays and γ-rays. For several years, research on scintillating glasses focused on borosilicate glasses [53–55], however, due to low luminous efficiency and additional disadvantages as radiation-induced photodarkening [56], recent research has focused on the improvement and discovery of new compositions. The growing and constant interest in these devices is a result of the need,

mainly, for materials in the form of fibers (e.g. for nuclear trace detectors) and economical detectors capable of being produced in large volumes and scales [19]. These considerations bring us back to phosphate compositions, which have been considered very promising hosts for scintillation detectors, due to the before mentioned advantages of low melting temperatures, the ability to incorporate higher RE ion concentration, and high emission efficiency [56].

Among the main RE active ions used as emitting centers are Ce^{3+}, Eu^{2+}, Eu^{3+}, Dy^{3+} and Tb^{3+}. Currently, Ce^{3+} is considered the main emitting center of inorganic scintillators due to its wide emission band in the visible region attributed to the 5d-4f transition and its lifetime in the order of nanoseconds. However, Ce^{3+} may exhibit the phenomenon of self-suppression of luminescence that occurs when trivalent cerium is oxidized to Ce^{4+}. The occurrence of this phenomenon causes a high reduction in the light output of the scintillator. Unlike Ce^{3+}, Tb^{3+} does not exhibit this phenomenon, since the oxidation of Tb^{3+} to Tb^{4+} is thermodynamically less favored [57]. For this reason, this ion was chosen as a dopant in this doctorate study.

REFERENCES

[1] Global Inorganic Scintillators Market Size, Share, Trends, COVID-19 Impact and Growth, Market Data Forecast. (2022). https://www.marketdataforecast.com/market-reports/inorganic-scintillators-market (accessed June 4, 2022).

[2] S.N. Ahmed, Physics and Engineering of Radiation Detection, 2º Edition, 2015.

[3] L.L. Hench, The story of Bioglass®, J Mater Sci Mater Med. 17 (2006) 967–978. https://doi.org/10.1007/s10856-006-0432-z.

[4] M.H. Braga, C. M Subramaniyam, A.J. Murchison, J.B. Goodenough, Nontraditional, Safe, High Voltage Rechargeable Cells of Long Cycle Life, J Am Chem Soc. 140 (2018) 6343–6352. https://doi.org/10.1021/jacs.8b02322.

[5] Y.P. Sun, X. bin Xia, Y.B. Qia, Z.Q. Zhao, H.J. Ma, X.Y. Liu, Z.H. Qian, Properties of phosphate glass waste forms containing fluorides from a molten salt reactor, Nuclear Science and Techniques. 27 (2016) 1–7. https://doi.org/10.1007/s41365-016-0059-9.

[6] J.E. Shelby, Introduction to Glass Science and Technology, 2ª Edition, 2005.

[7] E.D. Zanotto, J.C. Mauro, The glassy state of matter: Its definition and ultimate fate, J Non Cryst Solids. 471 (2017) 490–495. https://doi.org/10.1016/j.jnoncrysol.2017.05.019.

[8] Z.H. Jiang, Q.Y. Zhang, The structure of glass: A phase equilibrium diagram approach, Prog Mater Sci. 61 (2014) 144–215. https://doi.org/10.1016/j.pmatsci.2013.12.001.

[9] W.H. Zachariasen, The atomic arrangement in glass, J Am Chem Soc. 54 (1932) 3841–3851. https://doi.org/10.1021/ja01349a006.

[10] A. Łapa, M. Cresswell, I. Campbell, P. Jackson, W.H. Goldmann, R. Detsch, A.R. Boccaccini, Gallium- and Cerium-Doped Phosphate Glasses with Antibacterial Properties for Medical Applications, Adv Eng Mater. 22 (2020) 1901577. https://doi.org/10.1002/adem.201901577.

[11] H. Kofuji, T. Yano, M. Myochin, K. Matsuyama, T. Okita, S. Miyamoto, Chemical Durability of Iron-phosphate Glass as the High Level Waste from Pyrochemical Reprocessing, Procedia Chem. 7 (2012) 764–771. https://doi.org/10.1016/j.proche.2012.10.116.

[12] A. Kiani, N.J. Lakhkar, V. Salih, M.E. Smith, J. v. Hanna, R.J. Newport, D.M. Pickup, J.C. Knowles, Titanium-containing bioactive phosphate glasses, Philosophical Transactions of the Royal Society A: Mathematical, Physical and Engineering Sciences. 370 (2012) 1352–1375. https://doi.org/10.1098/rsta.2011.0276.

[13] B. Cabal, L. Alou, F. Cafini, R. Couceiro, D. Sevillano, L. Esteban-Tejeda, F. Guitián, R. Torrecillas, J.S. Moya, A new biocompatible and antibacterial phosphate free glass-ceramic for medical applications, Sci Rep. 4 (2014) 1–9. https://doi.org/10.1038/srep05440.

[14] L.A. Boatner, B.C. Sales, Lead iron phosphate glass as a containment medium for disposal of high-level nuclear waste, 4.847.008, 1986. https://patents.google.com/patent/US4847008A/en.

[15] C.R. Kesavulu, A.C. Almeida Silva, M.R. Dousti, N.O. Dantas, A.S.S. de Camargo, T. Catunda, Concentration effect on the spectroscopic behavior of Tb3+ ions in zinc phosphate glasses, J Lumin. 165 (2015) 77–84. https://doi.org/10.1016/j.jlumin.2015.04.012.

[16] M.R. Dousti, G.Y. Poirier, A.S.S. de Camargo, Structural and spectroscopic characteristics of Eu^{3+}-doped tungsten phosphate glasses, Opt Mater (Amst). 45 (2015) 185–190. https://doi.org/10.1016/j.optmat.2015.03.033.

[17] M.R. Dousti, G.Y. Poirier, A.S.S. de Camargo, Tungsten sodium phosphate glasses doped with trivalent rare earth ions (Eu^{3+}, Tb^{3+}, Nd^{3+} and Er^{3+}) for visible and near-infrared applications, J Non Cryst Solids. 530 (2020). https://doi.org/10.1016/j.jnoncrysol.2019.119838.

[18] G. Galleani, C. Doerenkamp, S. Santagneli, C.J. Magon, A.S.S. de Camargo, H. Eckert, Compositional Optimization of Emission Properties for Rare-Earth Doped Fluoride Phosphate Glasses: Structural Investigations via NMR, EPR, and Optical Spectroscopies, Journal of Physical Chemistry C. (2019). https://doi.org/10.1021/acs.jpcc.9b10851.

[19] D. Wisniewski, L.A. Boatner, J.O. Ramey, M. Wisniewska, J.S. Neal, G.E. Jellison, Exploratory research on the development of novel Ce^{3+} -activated phosphate glass scintillators, IEEE Trans Nucl Sci. 55 (2008) 3692–3702. https://doi.org/10.1109/TNS.2008.2007567.

[20] S. Nikl, M. ; Nitsch, K. ; Mihokova, E. ; Solovieva, N. ; Mares, J. A. ; Fabeni, P. ; Pazzi, G. P. ; Martini, M. ; Vedda, A. ; Baccaro, Efficient radioluminescence of the doped Na – Gd phosphate glasses, Appl Phys Lett. 77 (2000) 2159–2161. https://doi.org/10.1063/1.1315337.

[21] D. He, C. Yu, J. Cheng, S. Li, L. Hu, Energy transfer between Gd^{3+} and Tb^{3+} in phosphate glass, Journal of Rare Earths. 29 (2011) 48–51. https://doi.org/10.1016/S1002-0721(10)60392-4.

[22] R.K. Brow, Review: the structure of simple phosphate glasses, J Non Cryst Solids. 263 (2000) 1–28. https://doi.org/10.1016/S0022-3093(99)00620-1.

[23] G. Galleani, S.H. Santagneli, Y. Messaddeq, M. de Oliveira, H. Eckert, Rare-earth doped fluoride phosphate glasses: structural foundations of their luminescence properties, Phys. Chem. Chem. Phys. 19 (2017) 21612–21624. https://doi.org/10.1039/C7CP03927A.

[24] M.O. Keeffe, A. Navrotsky, Structure and Bonding in Crystals, 1981.

[25] G.K. Marasinghe, M. Karabulut, C.S. Ray, D.E. Day, D.K. Shuh, P.O. Allen, M.L. Saboungi, M. Grimsditch, D. Haeffner, Properties and structure of vitrified iron phosphate nuclear wasteforms, J Non Cryst Solids. 263 (2000) 146–154. https://doi.org/10.1016/S0022-3093(99)00631-6.

[26] J.D. Musgraves, J. Hu, L. Calvez, Handbook of Glass, 1ª Edition, 2019.

[27] S. Ibrahim, M.M. Morsi, Effect of increasing Fe_2O_3 content on the chemical durability and infrared spectra of (25 - x) Na_2O-x Fe_2O_3-25PbO-50SiO_2 glasses, Mater Chem Phys. 138 (2013) 628–632. https://doi.org/10.1016/j.matchemphys.2012.12.030.

[28] H. Hamzah, R. Arifin, S.K. Ghoshal, Reduction of hygroscopicity in zinc-calcium-phosphate glass via iron-oxide incorporation, Solid State Phenomena. 268 SSP (2017) 82–86. https://doi.org/10.4028/www.scientific.net/SSP.268.82.

[29] K. Sun, Fundamental Condition of Glass Formation, Journal of the American Ceramic Society. 30 (1947) 277–281. https://doi.org/10.1111/j.1151-2916.1947.tb19654.x.

[30] D.E. Day, Z. Wu, C.S. Ray, P. Hrma, Chemically durable iron phosphate glass wasteforms, J Non Cryst Solids. 241 (1998) 1–12. https://doi.org/10.1016/S0022-3093(98)00759-5.

[31] C.C. de Araujo, W. Strojek, L. Zhang, H. Eckert, G. Poirier, S.J.L. Ribeiro, Y. Messaddeq, Structural studies of $NaPO_3$-WO_3 glasses by solid state NMR and Raman spectroscopy, J Mater Chem. 16 (2006) 3277–3284. https://doi.org/10.1039/b605971f.

[32] N.G. Connelly, R.M. Hartshorn, T. Damhus, A.T. Hutton, Nomenclature of inorganic chemistry IUPAC Recommendations 2005, RSC Publishing, 2005.

[33] W.T. Carnall, G.L. Good, K. Rafnak, R.S. Rana, A systematic analysis of the spectra of lanthanides doped into single crystals LaF_3, J Chem Phys. 90 (1989) 3443–3457. https://doi.org/10.1063/1.455853.

[34] O. Laporte, W.F. Meggers, Some rules of spectral structure, J Opt Soc Am. 11 (1925) 459–463. https://doi.org/10.1364/JOSA.11.000459.

[35] N. Wantana, E. Kaewnuam, Y. Ruangtaweep, D. Valiev, S. Stepanov, K. Yamanoi, H.J. Kim, J. Kaewkhao, Radio, cathodo and photoluminescence investigations of high density WO_3-Gd_2O_3-B_2O_3 glass doped with Tb^{3+}, Radiation Physics and Chemistry. 164 (2019) 108350. https://doi.org/10.1016/j.radphyschem.2019.108350.

[36] S.L. Pôrto, E. Longo, P.S. Pizani, T.M. Boschi, L.G.P. Simões, S.J.G. Lima, J.M. Ferreira, L.E.B. Soledade, J.W.M. Espinoza, M.R. Cássia-Santos, M.A.M.A. Maurera, C.A. Paskocimas, I.M.G. Santos, A.G. Souza, Photoluminescence in the $Ca_xSr_{1-x}WO_4$ system at room temperature, J Solid State Chem. 181 (2008) 1876–1881. https://doi.org/10.1016/j.jssc.2008.04.015.

[37] P. Lecoq, A. Gektin, M. Korzhik, Inorganic Scintillators for Detector Systems, Second edi, Springer, Berlim, Germany, 2017.

[38] F.N. Flakus, Radiation detection Detecting and measuring ionizing radiation - a short history, IEAE Bulletin. 23 (1981) 31–36.

[39] R.F. Mould, The early history of x-ray diagnosis with emphasis on the contributions of physics 1895-1915, Phys Med Biol. 40 (1995) 1741–1787. https://doi.org/10.1088/0031-9155/40/11/001.

[40] Jim Powell, Wilhelm Roentgen discovers the x-ray - a picture from the past, The Guardian. (2013).

[41] L. Cerrito, Radiation and detectors : introduction to the physics of radiation and detection devices, 1ª Edition, 2017.

[42] S.R. Cherry, J.A. Sorenson, M.E. Phelps, Physics in Nuclear Medicine, 4ª Edition, 2012.

[43] G.F. Knoll, Radiation Detection and Measurement, 4ª Edition, WILEY John Wiley & Sons, Inc., 2010.

[44] G. Bizarri, Scintillation mechanisms of inorganic materials: From crystal characteristics to scintillation properties, J Cryst Growth. 312 (2010) 1213–1215. https://doi.org/10.1016/j.jcrysgro.2009.12.063.

[45] Y. Zhou, J. Chen, O.M. Bakr, O.F. Mohammed, Metal Halide Perovskites for X - ray Imaging Scintillators and Detectors, (2021). https://doi.org/10.1021/acsenergylett.0c02430.

[46] T. Yanagida, Inorganic scintillating materials and scintillation detectors, Proc Jpn Acad. 94 (2018) 75–97. https://doi.org/10.2183/pjab.94.007.

[47] C.W.E. van E. Delft, Inorganic scintillators in medical imaging, Phys Med Biol. 85 (2002) R85–R106. https://doi.org/10.1016/S0168-9002(03)01542-0.

[48] J. Glodo, Y. Wang, R. Shawgo, C. Brecher, R.H. Hawrami, J. Tower, K.S. Shah, New Developments in Scintillators for Security Applications, Phys Procedia. 90 (2017) 285–290. https://doi.org/10.1016/j.phpro.2017.09.012.

[49] D.G. Anderson, J. Dracass, T.P. Flanagan, Luminescent Glasses for use in the Detection of Nuclear Radiation, Journal of Electronics and Control. 7 (1959) 463–464. https://doi.org/10.1080/00207215908937233.

[50] R.J. Ginther, J.H. Schulman, Glass Scintillators, IRE TRANSACTIONS ON NUCLEAR SCIENCE. 5 (1958) 92–95. https://doi.org/10.1109/TNS2.1958.4315633.

[51] R.J. Ginther, New Cerium Activated Scintillating Glasses, IRE Transactions on Nuclear Science. NS-7 (1960) 28–31. https://doi.org/10.1109/TNS2.1960.4315731.

[52] C. Coceva, Pulse-shape discrimination with a glass scintillator, Nuclear Instruments and Methods. 21 (1963) 93–96. https://doi.org/10.1016/0029-554X(63)90092-2.

[53] C. Jiang, Q. Zeng, Scintillation luminescence of cerium-doped borosilicate glasses containing rare-earth oxide, Hard X-Ray, Gamma-Ray and Neutron Detector Physics II. 4141 (2000) 316–323. https://doi.org/10.1117/12.407593.

[54] M.W. Kielty, M. Dettmann, V. Herrig, M.G. Chapman, M.R. Marchewka, A.A. Trofimov, U. Akgun, L.G. Jacobsohn, Investigation of Ce^{3+} luminescence in borate-rich borosilicate glasses, J Non Cryst Solids. 471 (2017) 357–361. https://doi.org/10.1016/j.jnoncrysol.2017.06.022.

[55] Z. Fu, P. Xu, Y. Yang, C. Li, H. Lin, Q. Chen, G. Yao, Y. Zhou, F. Zeng, Study on luminescent properties of Ce^{3+} sensitized Tb^{3+} doped gadolinium borosilicate scintillating glass, J Lumin. 196 (2018) 368–372. https://doi.org/10.1016/j.jlumin.2017.12.070.

[56] Y. Yao, L. Liu, Y. Zhang, D. Chen, Y. Fang, G. Zhao, Optical properties of Ce^{3+} doped fluorophosphates scintillation glasses, Opt Mater (Amst). 51 (2016) 94–97. https://doi.org/10.1016/j.optmat.2015.11.026.

[57] X. Sun, M. Gu, M. Zhang, S. Huang, Influence of CeO_2 on scintillating properties of Tb^{3+} -doped silicate glasses, Journal of Rare Earths. 28 (2010) 340–344. https://doi.org/10.1016/S1002-0721(09)60267-2.

[58] I.C. Pinto, G. Galleani, L.G. Jacobsohn, Y. Ledemi, Y. Messaddeq, A.S.S. de Camargo, Fluorophosphate glasses doped with Eu^{3+} and Dy^{3+} for X-ray radiography, J Alloys Compd. 863 (2021) 158382. https://doi.org/10.1016/j.jallcom.2020.158382.

[59] T. Yamashita, Y. Ohishi, Concentration and temperature effects on the spectroscopic properties of Tb^{3+} doped borosilicate glasses, J Appl Phys. 102 (2007) 123107. https://doi.org/10.1063/1.2821789.

[60] T.O. Sales, R.J. Amjad, C. Jacinto, M.R. Dousti, Concentration dependent luminescence and cross-relaxation energy transfers in Tb^{3+} doped fluoroborate glasses, J Lumin. 205 (2019) 282–286. https://doi.org/10.1016/j.jlumin.2018.09.031.

[61] A.D. Sontakke, K. Biswas, K. Annapurna, Concentration-dependent luminescence of Tb^{3+} ions in high calcium aluminosilicate glasses, J Lumin. 129 (2009) 1347–1355. https://doi.org/10.1016/j.jlumin.2009.06.027.

2 OBJECTIVES

The general objective of this doctorate research project was the development and characterization of novel tungsten gallium-phosphate glasses doped with Tb^{3+} ions in different concentrations for application as scintillators in high-energy radiation detectors. The following steps were set as goals to be achieved:

i. Development of glasses based on the $(NaPO_3)_{80-x}(Ga_2O_3)_{20}(Na_2WO_4)_x$ composition with high chemical stability and optimum optical properties.
ii. Structural characterization of the glasses via DSC, FT-IR, Raman and solid state NMR techniques seeking for the understanding of the former and modifier elemental roles.
iii. Determination of the best NaPGaW matrix compositions for posterior Tb^{3+}-doping, based on the structural analysis.
iv. Photophysical characterization of the glasses through UV-vis absorption, and steady-state and time resolved excitation and emission.
v. Evaluation of the potential of the undoped and doped NaPGaW glasses as intrinsic and extrinsic scintillator, when subjected to ultraviolet and X-ray excitations.

3 OUTLINE

This thesis reports an exploratory investigation of the NaPGaW vitreous system from the point of view of its thermal, structural, spectroscopic, and optical properties for potential application of these materials as vitreous scintillators. The obtained results are exposed in the text in the form of a collection of articles published during the development of the project, which is divided into the following three main parts:

i. **Study of the thermal and structural properties of new gallium tungsten-phosphate glasses**. The first part of the research reports the thermal and structure properties of the new tungsten gallium-phosphate glass composition synthesized by the traditional melt-quenching technique. Solid-state NMR studies were carried out in collaboration with Prof[a] Silvia Helena Santagneli, Prof. Marcos de Oliveira Jr. e Prof. Hellmut Eckert. The compilation of these studies was published in the J. of Non-Crystalline Solids, under the title *Preparation, Characterization, and*

Structural Studies of New Sodium Gallium Tungstate Phosphate Glasses (DOI: 10.1016/j.jnoncrysol.2022.122100).

ii. **Evaluation of the intrinsic emission of undoped gallium tungsten-phosphate glasses for application as a scintillator detector.** In this part of the research, the broadband emission of the tungsten complexes in the undoped glasses was reported. A new series of NaPGaW glasses were synthesized to study the influence of the Na_2WO_4 content on the intrinsic scintillator properties. Furthermore, the emission dependence on temperature was evaluated to determine de capacity of the NaPGaW to be explored as a cryogenic scintillator. This work was published in the J. of Non-Crystalline Solids under the title *Tungsten gallium-phosphate glasses as promising intrinsic scintillators* (DOI: 10.1016/j.jnoncrysol.2022.122097).

iii. **Study of Tb^{3+} doped tungsten gallium-phosphate as an extrinsic scintillator.** In the last part of the research, NaPGaW glasses were doped with Tb^{3+} aiming to study the optical and structural properties of these glasses, as well as to evaluate their potential for application as slow-event scintillators. A manuscript with the results obtained were published in the J. Alloys and Compounds, under the title *Promising Tb^{3+}-doped gallium tungsten-phosphate glass scintillator: Spectroscopy, energy transfer and UV/X-ray sensing* (DOI: 10.1016/j.jallcom.2022.164016).

4 PREPARATION, CHARACTERIZATION, AND STRUCTURAL STUDIES OF NEW SODIUM GALLIUM TUNGSTATE PHOSPHATE GLASSES

Thiago A. Lodi[a], Gustavo Galleani[a], Marcos de O. Junior[a], Silvia H. Santagneli[b], Hellmut Eckert[a], Andrea S.S de Camargo[a]

[a] São Carlos Institute of Physics, University of São Paulo, Av. Trabalhador Saocarlense 400, São Carlos, SP, 13566-590, Brazil.

[b] Institute of Chemistry, São Paulo State University/UNESP, Prof. Francisco Degni, 55, Araraquara, SP, 14800-060, Brazil.

DOI: *10.1016/j.jnoncrysol.2022.122100*

ABSTRACT

A new glass forming region in the quaternary system Na_2O-P_2O_5-WO_3-Ga_2O_3 along the composition line $(NaPO_3)_{80-x}(Ga_2O_3)_{20}(Na_2WO_4)_x$ (x = 0, 5, 10, 15, 20 and 25 mol%) has been prepared and characterized by X-ray diffraction, Differential Scanning Calorimetry (DSC), Raman scattering and ^{31}P, ^{23}Na and ^{71}Ga nuclear magnetic single and double resonance NMR techniques. The partial substitution of the $NaPO_3$ component by Na_2WO_4 produces a significant increase of molar volume (decreased oxygen packing density), whereas the glass transition temperatures T_g pass through a shallow maximum near x = 10 to 15. While in the x = 0 sample the structure is dominated by Q^1 units linked to gallium in four-, five- and six-coordination, the gradual substitution of phosphate by tungstate effects significant network reconstruction, eliminating P-O-P linkages the concentration of which is found to be greatly diminished above the x = 10 level. While the structure of these glasses is dominated by Q^0 units, connected to both gallium and tungstate species, $^{71}Ga\{^{31}P\}$ REDOR data suggest significant decreases in the extent of gallium-phosphorus connectivity with increasing Na_2WO_4 content. Finally, monotonic changes in both ^{23}Na chemical shifts and ^{23}Na-^{31}P second moment values, $M_{2(Na\text{-}P)}$, indicate that the anionic surroundings of the sodium ions evolve from a pure phosphate to a mixed phosphate/tungstate environment.

4.1 Introduction

Over the past centuries, glasses have been applied extensively in several areas of knowledge due to their wide versatility. Their excellent mechanical and chemical stability combined with their unique optical properties has been explored to design many advanced technological applications, in areas as diverse as such as nuclear waste storage, smartphone screens, light source design, optical sensors, bioglass implants for skin and bone regeneration, drug delivery, self-cleaning and bactericidal surfaces, etc [1–4]. The alkaline/alkaline-earth phosphate glasses are particularly interesting due to their low melting and glass transition temperatures, high thermal expansion coefficients, biocompatibility, and wide transmission region from the UV to the far-IR range [5,6]. However, the high hygroscopicity of phosphate glasses may be a disadvantage depending on the final application. One way to overcome this problem is to include intermediate oxides such as Al_2O_3 and Ga_2O_3 [5].

Recently, gallium-phosphate glasses have attracted attention due to their thermal, chemical and mechanical stability. In the binary $(Ga_2O_3)_x$ - $(NaPO_3)_{1-x}$ system, the incorporation of Ga_2O_3 leads to a dramatic increase of the glass transition temperature (Tg), albeit in a non-linear fashion [7]. Gallium phosphate based glasses are also promising for accommodating luminescent rare-earth and transition metal dopants, for sensors, lasers and white-light generation. The design of optimal glass compositions relies on structure/property correlations elucidated by detailed structural studies. For the system $(NaPO_3)_{1-x}$ $(Ga_2O_3)_x$, Ren and Eckert [7] were able to study the structural organization by a number of complementary solid-state NMR techniques, highlighting the role of the intermediate oxide Ga_2O_3 both as a network former and as a network modifier in the structural organization of phosphate glasses [7,8]. Hee et al. [6] reported that while there is considerable similarity between the structural and property characteristics of gallo- and aluminophosphate glasses, the incorporation of gallium has certain advantages that can be profitably used in optical applications. Specifically, the substitution of the Al^{3+} by the larger Ga^{3+} can open the glass network to better accommodate the rare-earth ions, which is pivotal for photonic applications. Also, the higher hyperpolarizability of Ga^{3+} compared to Al^{3+} may also increase the possibility of accessing non-linear optical properties [6].

The addition of different modifiers has been investigated in order to create a synergy between thermal/chemical stability, structural and optical properties. In this context, tungsten oxide-containing phosphate glasses are of great interest due to their superior chemical stability

compared to alkali phosphate glasses, their ability to incorporate high concentrations of rare-earth ions, and because of their special photochromic and electrochromic properties [9,10]. For example, de Araujo et al. [9] reported for the $NaPO_3$ - WO_3 glass system, that the addition of tungsten to $NaPO_3$ creates P-O-W linkages that initially crosslink between the one-dimensional metaphosphate chains, and at higher concentrations transform the structure into a three-dimensional network based on interlinked PO_4 tetrahedral units and WO_6 polyhedra. This system is characterized by a strong increase in glass transition temperature as a function of WO_3 content. On the other hand, binary glass of composition $0.5LiPO_3$-$0.5Na_2WO_4$ show only a moderately increased Tg value (353 °C) in comparison to pure $LiPO_3$ glass (325 °C) (Figure S1). Finally, the addition of tungsten oxide to phosphate glasses can provide interesting properties for applications as scintillators, as the higher atomic number element in the formulation effects increased density. Concerning the optical properties, tungsten containing glasses generally present a broad emission band in the visible range, which can be explored for single-phase white lighting [11].

To date, the structural consequences of imparting the above functional characteristics to phosphate glasses by the combined presence of tungsten and gallium oxide remain unknown. Here we report the results of a systematic structural study of a new gallium tungsten-phosphate glass system with composition $(NaPO_3)_{80-x}(Ga_2O_3)_{20}(Na_2WO_4)_x$, via Raman scattering and multinuclear solid-state NMR techniques.

4.2. Experimental section

Glass synthesis. The starting powdered materials were sodium hexametaphosphate, $NaPO_3$ (Aldrich 65-70% P_2O_5 basis), gallium oxide, Ga_2O_3 (Aldrich 99.99% pure) and $Na_2WO_4.2H_2O$ (Aldrich 99% pure). All the $(NaPO_3)_{80-x}(Ga_2O_3)_{20}(Na_2WO_4)_x$ (x = 0, 5, 10, 15, 20 and 25 mol%) glasses were prepared by conventional melt-quenching methods. Stoichiometric batches of the solid starting materials were melted in a platinum crucible at 1000-1100 ºC (depending on the composition), for 1h, under air atmosphere. Immediately after the quenching, the melt was poured into a preheated stainless-steel mold at 280 ºC. To minimize the thermal and mechanical stresses, the glasses were annealed at 300 °C for 4 h and then slowly cooled to ambient temperature. The annealing temperature chosen for this purpose was high enough to permit thermal relaxation to remove mechanical stresses, but low enough to avoid crystallization.

Glass characterization. The amorphous state of each sample was confirmed by X-ray diffraction, using a RIGAKU Rotaflex RU200B (Cu Kα, λ= 1.54434 Å) X-ray diffractometer. Differential scanning calorimetry (DSC) measurements were conducted with a TA Instruments model 2910 calorimeter on 25 ± 5mg glass pieces within aluminum pans, using a heating rate of 10ºC min^{-1}, under N_2 atmosphere, with a maximum error of ± 2 °C for Tg and Δt. Glass densities were measured using the Archimedes principle using distilled water as the immersion fluid. The oxygen molar volume (Vo) for all glasses was calculated using the relation,

$$Vo = \frac{M}{\rho}\left(\frac{1}{\Sigma x_i n_i}\right) = \frac{M}{\rho\,(3 \times x_{NaPO_3} + 3 \times x_{Ga_2O_3} + 4 \times x_{Na_2WO_4})} \quad (1)$$

These values were used to calculate the oxygen packing density (OPD), which is a measure of tightness of packing of the oxide network, using the expression,

$$OPD = 1000C\,\frac{\rho}{M} \quad (2)$$

where C is the number of oxygen atoms per formula unit and M is the molecular weight.
The Raman spectra were obtained using a LabRam HR spectrometer, Horiba-Jobin Yvon, at room temperature. The 632 nm line from an He/Ne laser was focused on the samples by an optical microscope using a long work distance 50x objective.

Solid-state NMR. Solid state ^{31}P and ^{23}Na NMR studies were carried out on a Bruker Avance III spectrometer operating at 400 MHz (magnetic flux density 9.4 T), equipped with a 4 mm magic-angle spinning (MAS) probe. ^{31}P MAS NMR spectra were recorded at a spinning frequency of 14.0 kHz using π/2 pulses of 3.3 μs length and a relaxation delay of 240 s. Double-quantum (DQ-) filtered spectra were obtained in a separate set of measurements, using the 1-D refocused INADEQUATE method, resulting in the selective detection of only those ^{31}P nuclei that are involved in a P–O–P linkage (Q^1, Q^2 or Q^3 units). In this experiment, the two-bond indirect ^{31}P - ^{31}P spin–spin coupling involving the covalently linked ^{31}P nuclei is used to create a double-quantum coherence, which is subsequently reconverted to detectable magnetization. The latter can then be detected selectively, because of its special coherence pathway [12,13], while the signals of Q^0 units not involved in P-O-P linkages are suppressed by appropriate receiver phase cycling. Experimental conditions were: spinning speed 14.0 kHz, π/2 pulse length 3.0 μs and a relaxation delay of 60 s. The mixing time for DQ coherence creation was

16.6 ms, corresponding to a value of the indirect coupling constant $^{2}J(^{31}P–^{31}P)$ of 30 Hz. Chemical shifts were referenced against 85% H_3PO_4. ^{23}Na MAS-NMR spectra were recorded using short pulses of 1 μs length at a spinning speed of 14.0 kHz and a relaxation delay of 2 s. Chemical shifts are reported relative to a 1 M NaCl aqueous solution (0 ppm). $^{23}Na\{^{31}P\}$ rotational echo double resonance (REDOR) experiments were done at 9.4 T, at a MAS frequency of 14.0 kHz using the sequence of Gullion and Schaefer [12]. The optimum π pulse lengths for the decoupling channel were obtained by maximizing the REDOR difference signal ΔS at a fixed dephasing time. Optimum values were 2.6 and 6.0 μs for ^{23}Na and ^{31}P, respectively. XY-4 phase cycling was used for the ^{31}P recoupling π-pulses. Approximate second moments M_2(Na-P) were obtained by applying a parabolic fit to the REDOR data within the range $\Delta S/S_0 \leq 0.2$, according to the expression [13].

$$\frac{\Delta S}{S_0} = \frac{4}{3\pi^2} f (N T_R)^2 M_{2(\mathrm{Na-P})} \qquad (3)$$

where the calibration factor f depends on the experimental conditions applied and can be determined by conducting the experiment on a crystalline reference compound with similar spin dynamics, for which the M2 values can be computed from the crystal structure. $^{31}P\{^{23}Na\}$ Rotational Echo Adiabatic Passage Double Resonance (REAPDOR) experiments [14] were carried out using a typical value for ^{31}P π-pulse duration of 6.0 μs and a spinning frequency of 14.0 kHz. A recycle delay of 60 s was applied in combination with a pre-saturation train of 10 π/2 pulses. Dipolar recoupling was achieved by ^{23}Na pulses applied at a nutation frequency of 96 kHz (measured directly on the samples) and for a duration of 1/3 of the rotor period. ^{71}Ga MAS-NMR spectra were measured on a Bruker Avance Neo spectrometer (magnetic flux density 14.1 T), using a 1.3 mm probe operated at a spinning speed of 60.0 kHz. Spectra were acquired with a rotor synchronized t_p-τ-2t_p Hahn echo-type pulse sequence. The pulse length *tp* was optimized by maximizing echo intensity. 80000 scans were accumulated with a relaxation delay of 0.25 s. Chemical shifts are referenced to 1M $Ga(NO_3)_3$ solutions, using solid GaP (307 ppm) as a secondary reference [15] $^{71}Ga\{^{31}P\}$REDOR measurements were done on the same spectrometer, using a 2.5 mm triple resonance probe, operated at a spinning speed of 15.0 kHz, using ^{31}P and ^{71}Ga nutation frequencies of 125 and 132 kHz, respectively. Parabolic fitting to eq. (1) was used in an analogous way to determine M_2(Ga-P) values.

4.3 Results, data analysis, and interpretation

Glass Properties. All prepared glasses are colorless, transparent, and bubble-free, as shown in Fig. S2. Densities and molar volumes are listed in Table 1.

Figure 1 shows that the density increases with the increasing Na_2WO_4 content from 3.05 to 3.74 $g.cm^{-3}$, owing to the concomitant molecular weight increase. The molar volumes, V_m, also increase from 39.05 to 47.03 $cm^3.mol^{-1}$ when the Na_2WO_4 content rises from 0 to 25 mol%. Concomitant increases of density and molar volumes as a function of composition have been reported earlier [16,17], and can be attributed to changes in oxygen packing density, caused by profound structural changes to be addressed in detail below [18].

Figure 1. Composition dependence of the density and the molar volume of $(NaPO_3)_{80-x}(Ga_2O_3)_{20}(Na_2WO_4)_x$ (x = 0, 5, 10, 15, 20 and 25 mol%) glasses and fits using a linear function, describing the linear increase of density and molar volume with Na_2WO_4 molar content in glass.

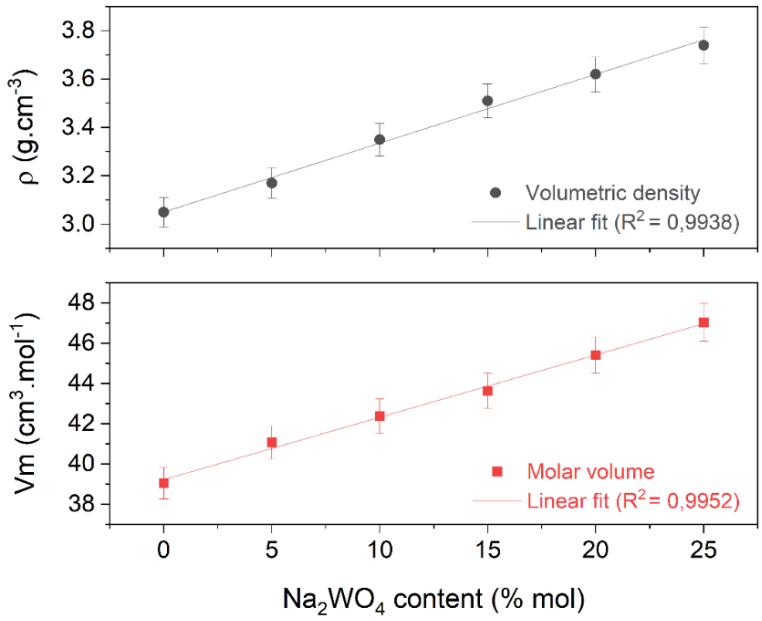

Table 3. Physical and thermal properties of $(NaPO_3)_{80-x}(Ga_2O_3)_{20}(Na_2WO_4)_x$ (x = 0, 5, 10, 15, 20 and 25 mol%) glasses.

Sample	x (mol %)	ρ (g.cm^{-3})	V_m (g.mol^{-1})	V_o (cm^3/mol)	OPD (mol/L)	T_g (ºC)	T_x (ºC)	ΔT (ºC)
NaPGa	0	3.05	39.05	13.02	76.83	396	512	116
NaPGaW5	5	3.17	41.08	13.47	74.24	400	490	90
NaPGaW10	10	3.35	42.39	13.67	73.14	407	511	104
NaPGaW15	15	3.51	43.63	13.85	72.19	411	521	110
NaPGaW20	20	3.62	45.42	14.19	70.46	401	515	114
NaPGaW25	25	3.74	47.03	14.47	69.10	394	512	118

X-ray diffraction data of all the glass samples are presented in Figure S3. The absence of sharp peaks over the range 2θ = 5° to 80° confirms the non-crystalline state of all the prepared glass samples. The partial substitution of $NaPO_3$ by Na_2WO_4 does not affect the amorphous state of the samples, but alters the appearance of the diffraction pattern, signifying the strong effect of the electron-rich tungstate component on the scattering pattern.

Differential Scanning Calorimetry (DSC). Figure 2 (a) shows the effect of Na_2WO_4 content (mol %) on the glass transition temperature (T_g) and the evolution of the thermal stability against crystallization ($\Delta T = T_x - T_g$). With successive substitution of $NaPO_3$ by Na_2WO_4, the T_g values stay nearly constant, passing through a shallow maximum near 10-15% mol of Na_2WO_4, and decrease at higher Na_2WO_4 levels. Similar behavior was observed by Manzani *et al.* [19] in the $NaPO_3$-WO_3-Bi_2O_3 glass system and by Poirier *et al*, [10] in the (80-0.8x) $NaPO_3$ - (20-0.2x) BaF_2-$x WO_3$ ternary system. Finally, we note that the sample containing 5% Na_2WO_4 shows a higher propensity for crystallization than the other glass samples.

Figure 2. (a) Compositional dependence of T_g and ΔT measured for $(NaPO_3)_{80-x}(Ga_2O_3)_{20}(Na_2WO_4)_x$ (x = 0, 5, 10, 15, 20 and 25 mol%) glasses as a function of Na_2WO_4 concentration. (b) DSC of NaPGaW20 glass (representative sample), showing the T_g and T_x determination procedure.

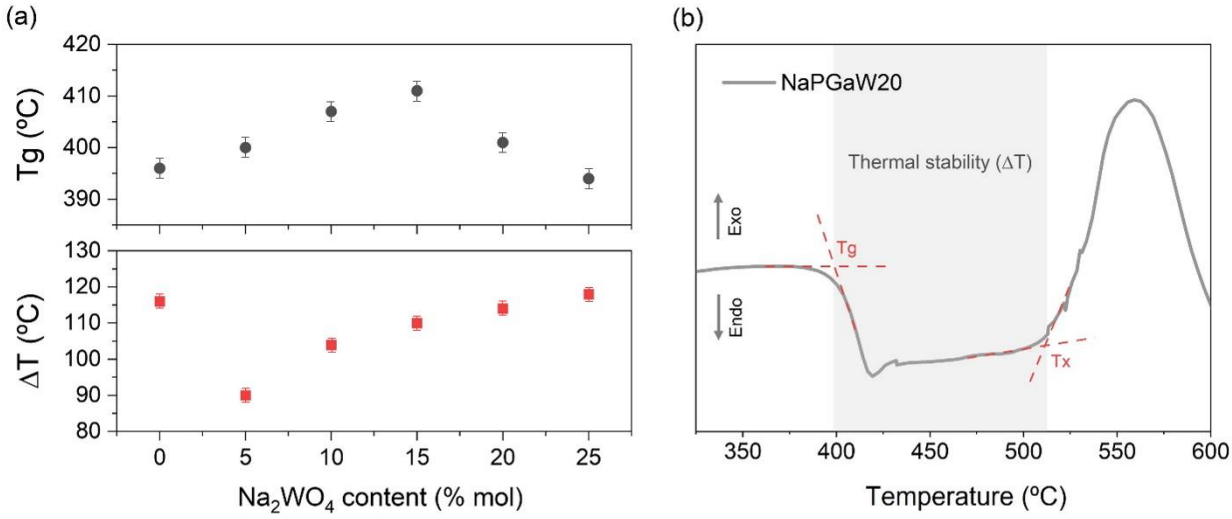

Raman spectra are depicted in Fig. 3. Peak assignments and associated references are listed in Table 2. Each Raman spectrum was deconvoluted using Gaussian functions to obtain the position of the bands (Figure S4). However, these deconvolutions only have qualitative character and the observed areas can only be compared on a relative basis between samples. The Raman spectra can be divided into two regions: (I) 200 - 700 cm^{-1} and (II) 700 - 1400 cm^{-1}. For the x = 0 glass (NaPGa), scattering peaks in region (I) are mainly attributed to different gallium-containing units. The band located near 340 - 350 cm^{-1} is assigned to vibrations involving six-coordinate gallium (GaO_6 units), [20] while the bands located at 500 and 630 cm^{-1} are attributed to bending [21] and stretching vibrations involving four-coordinate gallium (GaO_4 units). The GaO_6 vibrations appear in the same range as some torsional modes involving P-O-P linkages making it difficult to identify the latter in the spectra of Ga containing glasses [22]. Furthermore, in the low frequency region (I), bending modes involving W-O linkages [23] contribute to the spectra and become dominant with increasing Na_2WO_4 content. In the region (II) the band around 750 cm^{-1} is attributed to stretching vibrations of P-O-P linkages of Q^1 units [21]. With the gradual substitution of $NaPO_3$ by Na_2WO_4, numerous spectral changes are observed, mainly in the region (II), starting with the disappearance of the band centered at 750 cm^{-1}. Furthermore, in NaPGaW5 a sharp band at approximately 910 cm^{-1} appears, which may be attributed to (W=O or W–O) bond vibrations associated with either 4-, 5-, or 6-coordinate W atoms [9,23]. The assignment favored in the literature is to WO_4^{2-} groups, given that this band is present in the Raman spectra of crystalline reference compounds containing

tetrahedrally coordinated W atoms, such as M_2WO_4 (M=Li, Na, spinel structure) or $CaWO_4$ (scheelite structure) but not in the spectrum of octahedrally coordinated WO_3 [10, 23-25]. As the Na_2WO_4 concentration is increased the band broadens and shifts towards higher wave numbers (930 cm^{-1}); in addition, a band near 865 cm^{-1} appears. The band at 1000-1050 cm^{-1}, attributed to the symmetric vibration of the terminal P-O bonds in PO_3 (Q^1) units gradually decreases with the successive substitution of $NaPO_3$ by Na_2WO_4. On the other hand, the band around 1100 cm^{-1}, which was attributed by Velli et al. to the asymmetric stretching mode of Q^1 groups, appears to persist up to the highest Na_2WO_4 content studied (25 mol%) [26].

Figure 3. Raman spectra of $(NaPO_3)_{80-x}(Ga_2O_3)_{20}(Na_2WO_4)_x$ (x = 0, 5, 10, 15, 20 and 25 mol%) glasses.

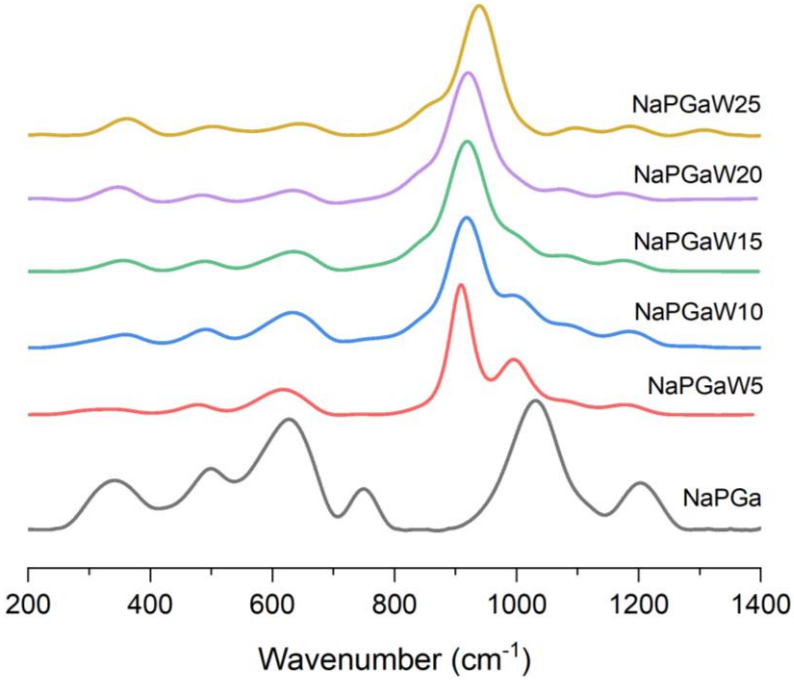

Table 4. Identified Raman bands observed in $(NaPO_3)_{80-x}(Ga_2O_3)_{20}(Na_2WO_4)_x$ (x = 0, 5, 10, 15, 20 and 25 mol%) glasses and their assignments.

Wavenumber (cm^{-1})	Vibrational mode assignments	Ref.
280 - 300	WO_6 bending vibrations	[23]
340 - 350	GaO_6 vibration mode	[20]
500	GaO_4 bending vibrations	[21]
630	GaO_4 stretching vibrations	[21]
750	P−O−P stretching vibrations	[21]
870-910	(W=O or W–O^-) bond vibrations, WO_4^{2-} groups	[9,23]
1000-1050	PO_3^{2-} symmetric stretching vibrations of Q^1 units	[26]
1100	PO_3^{2-} asymmetric stretching vibrations of Q^1 units	[26]
1200	PO_2^- symmetric stretching vibrations of Q^2 units or P=O vibration	[26]

^{31}P MAS NMR and ^{31}P REFOCUSED INADEQUATE EXPERIMENTS

Figure 4 shows the results from single-pulse ^{31}P MAS NMR experiments for all the NaPGaW glasses studied in this work. The spectra are broad and poorly resolved, suggesting a wide distribution of local environments. To facilitate the deconvolutions 1D refocused INADEQUATE data (Figure 5) were measured for some representative glasses. This experiment detects only those phosphorus species involved in P-O-P bonds, thereby producing useful constraints for peak deconvolutions.

For the W-free 80 $NaPO_3$ – 20 Ga_2O_3 glass, the ^{31}P MAS NMR spectrum looks very close to the one published by Ren and Eckert [7] who had also previously suggested a deconvolution based on a Refocused INADEQUATE experiment. However, as indicated in the Supporting Materials Section the Refocused INADEQUATE spectrum of our present sample looks slightly different, suggesting a different deconvolution model (Figure S5). Assisted by the Refocused INADEQUATE experiment, the present spectrum could be deconvoluted into seven components at 10, 5, 3.3, -1.1, -5.3, -11.2 and -17.8 ppm. The components at 10, 3.3 and -1.1 ppm belong to Q^0 species, whereas the resonances at 5, -5.3, -11.2 and -17.8 ppm have P-

O-P connectivity and can be attributed to Q^1 species linked to different numbers of gallium neighbors (i.e., Q^1_{0Ga}, Q^1_{1Ga}, Q^1_{2Ga} units) and Q^2 species linked to one gallium neighbor.

Spectra of samples containing Na_2WO_4 present increased complexity and decreased resolution. This must be attributed to additional lineshape components arising from the appearance of new phosphate species, having W atoms in the second coordination sphere. The deconvolutions shown in Figure 5 must be considered tentative. They were constrained by the parameters obtained from the Refocused INADEQUATE experiments, however, because of the limited resolution only estimates of the overall fractional areas of the Q^0 and the Q^1 species can be given. Table 3 summarizes the corresponding lineshape parameters and the Q^1 and Q^0 fractional areas (in %). As, with increasing *x*, $NaPO_3$ is substituted by Na_2WO_4 there is a clear trend towards decreasing P-O-P connectivity, indicating successive depolymerization of the phosphate network, leading to a dominance of $Q^0_{mW,Ga}$ units (see also Figure S6). In the glasses with $x \geq 15$ Q^1_{1Ga} and Q^1_{2Ga} units are almost completely absent. The Refocused INADEQUATE spectra show mostly a minor component near +3 ppm, which most likely arises from $P_2O_7^{4-}$ dimers of Q^1_{0Ga} species, and a weak shoulder near -8 ppm, which may be attributed to a Q^1 component interacting with both gallium and tungsten oxide units.

The compositional evolution observed in the ^{31}P MAS-NMR spectra in the present system is analogous to the ones observed in the binary systems $NaPO_3$-Ga_2O_3, [7] and $NaPO_3$-WO_3 [9] where it reflects the conversion of P-O-P into P-O-Ga (or P-O-W) linkages eventually resulting in the $Q^{(0)}_{mW}$ / $Q^{(0)}_{mGa}$ units that are also found in crystalline $NaWO_2PO_4$ [27], $Ga(PO_3)_3$ [7], and $GaPO_4$ [7].

Figure 4. ^{31}P MAS NMR spectra of $(NaPO_3)_{80-x}(Ga_2O_3)_{20}(Na_2WO_4)_x$ (x = 0, 5, 10, 15, 20 and 25 mol%) glasses under study, showing the proposed deconvolution model into Gaussian line shape components.

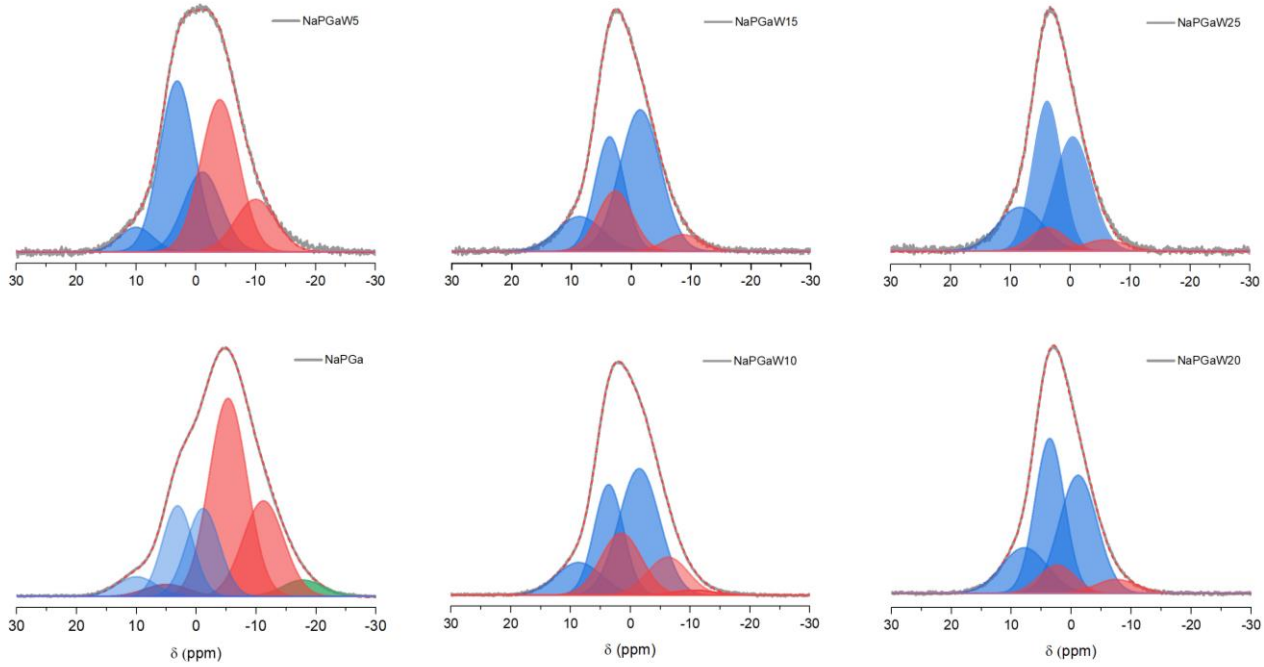

Figure 5. a-f: Single pulse ^{31}P MAS NMR spectra (a, c and e) and Refocused INADEQUATE spectra (b, d, f), of $(NaPO_3)_{80-x}(Ga_2O_3)_{20}(Na_2WO_4)_x$ (x = 0, 5, 10 mol%) glasses. *The spectra were deconvoluted using the appropriate number of Gaussian line shape components.* Q^0, Q^1 and Q^2 units are depicted in blue, red and green colors, respectively. g, h: experimental single-pulse (black) and Refocused INADEQUATE (red) spectra of $(NaPO_3)_{80-x}(Ga_2O_3)_{20}(Na_2WO_4)_x$ (x = 15 and 25 mol%) glasses.

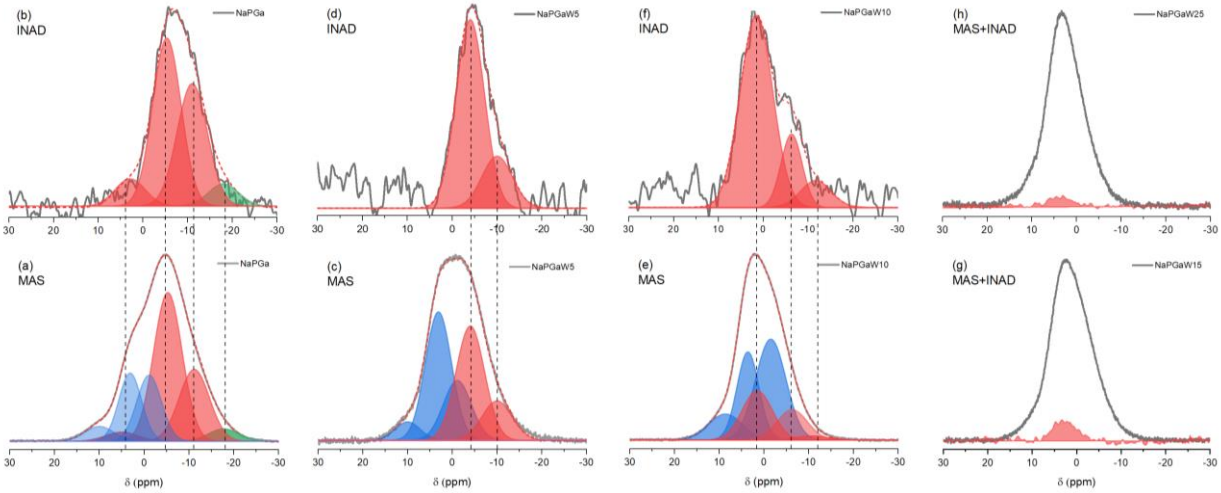

Table 3. ^{31}P NMR spectral fitting parameters of $(NaPO_3)_{80-x}(Ga_2O_3)_{20}(Na_2WO_4)_x$ (x = 0, 5, 10, 15, 20 and 25 mol%) glasses.

Sample	x (mol %)	Phosphorus species	δ_{iso}^{cs} (ppm) ±0.05ppm	FWHM (ppm) ±0.3	Area (mol%) ±2%
NaPGa	0	Q^0_{1Ga}	10.0	7.7	4
		Q^1	5.0	8.5	4
		Q^0_{2Ga}	3.1	6.0	14
		Q^0_{3Ga}	-1.1	6.5	15
		Q^1_{1Ga}	-5.3	7.5	39
		Q^1_{2Ga}	-11.2	8.0	20
		Q^2_{1Ga}	-17.8	8.0	4
NaPGaW5	5	Q^0_{1Ga}	10.0	6.6	4
		$Q^0_{2Ga,}Q^1_{0Ga}$	3.1	6.9	34
		Q^0_{3Ga}	-1.1	7.4	16
		Q^1_{1Ga}	-4.0	7.5	34
		Q^1_{2Ga}	-10.0	8.0	12
NaPGaW10	10	Q^0_{1Ga}	8.6	8.9	10
		Q^0_{2Ga}	3.6	5.8	22
		$Q^0_{m(Ga+W),}$	1.5	8.0	33
		$Q^1_{m(Ga+W)}$	-1.5	8.0	22
		$Q^1_{m(Ga+W)}$	-6.3	8.0	12
		$Q^1_{m(Ga+W)}$	-10.7	8.0	1
NaPGaW15	15	Q^0_{1Ga}	8.6	8.9	12
		Q^0_{2Ga}	3.6	5.8	25
		Q^1_{0Ga}	2.7	6.9	17
		$Q^0_{m(Ga+W)}$	-1.5	8.0	42
		$Q^1_{m(Ga+W)}$	-8.7	7.2	4
NaPGaW20	20	Q^0_{1Ga}	7.9	8.9	16
		Q^0_{2Ga}	3.6	5.8	36
		Q^1_{0Ga}	2.4	7.3	8
		$Q^0_{m(Ga+W)}$	-1.1	7.4	35
		$Q^1_{m(Ga+W)}$	-7.5	8.0	5

NaPGaW25	25	Q^0_{1Ga}	8.4	8.9	17
		Q^0_{2Ga}	3.9	5.8	37
		Q^1_{0Ga}	3.7	6.9	7
		$Q^0_{m(Ga+W)}$	-0.4	7.4	35
		$Q^1_{m(Ga+W)}$	-5.8	8.0	4

^{23}Na MAS NMR and ^{23}Na{^{31}P} REDOR. Representative ^{23}Na MAS NMR spectra are shown in Figure 6. All the NaPGaW glasses exhibit a single broad ^{23}Na resonance with a maximum near −12 ppm. The line shape shows the characteristic asymmetric form arising from a wide distribution of quadrupolar coupling constants, influencing the signal of the central $m = {}^{1}/_{2} \leftrightarrow m = -{}^{1}/_{2}$ transition of the quadrupolar ^{23}Na nucleus as described by second-order perturbation theory. The average isotropic chemical shifts ($\langle\delta_{iso}^{cs}\rangle$) obtained from Czjzek line shape fits are listed in Table 4; in addition, the average magnitudes of the quadrupolar coupling constants, $\langle\langle|C_Q|\rangle\rangle$, deduced from the distribution width of the Czjzek model, are given [28]. Generally, these data are consistent with only slight changes in the sodium environment. They show consistently that the average ^{23}Na quadrupolar coupling constant is independent of composition, while there is a definitive (albeit weak) trend of increasing chemical shift with increasing Na_2WO_4 content. This latter result is consistent with a random anion distribution, in which the anionic environment of the sodium ions changes gradually from a pure phosphate to a mixed phosphate/tungstate coordination.

Figure 6. ^{23}Na MAS NMR spectra of representative $(NaPO_3)_{80-x}(Ga_2O_3)_{20}(Na_2WO_4)_x$ (x = 0, 5, 10, 15, 20 and 25 mol%) glasses and simulations based on the Czjzek distribution model.

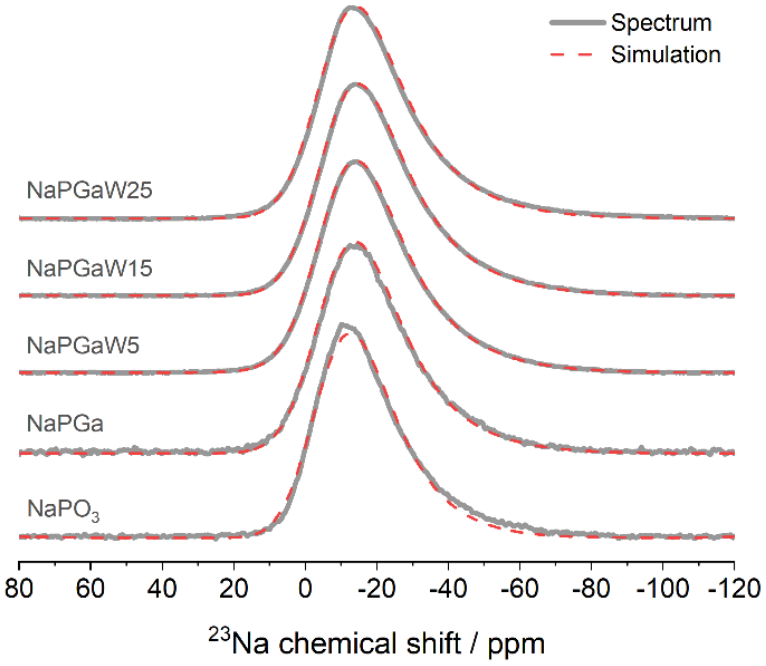

Table 4. ^{23}Na isotropic chemical shifts $<\delta_{iso}^{cs}>$ and average magnitudes of quadrupolar coupling constants $\langle|C_Q|\rangle$ obtained by Czjzek fits [28] of the ^{23}Na MAS NMR spectra, and second moments $M_{2(Na-P)}$ and $M_{2(Ga-P)}$ measured via ^{23}Na{^{31}P} and ^{71}Ga{^{31}P} REDOR, respectively, of $(NaPO_3)_{80-x}(Ga_2O_3)_{20}(Na_2WO_4)_x$ (x = 0, 5, 10, 15, 20 and 25 mol%) glasses. The reported values for $M_{2(Na-P)}$ are uncorrected whereas the $M_{2(Ga-P)}$ measured by ^{71}Ga{^{31}P}REDOR are corrected using the calibration factor f = 0.68, obtained by comparison of the experimental data for a polycrystalline $Ga(PO_3)_3$ sample and the calculated value based on the crystal structure [29], using the Van Vleck equation [30]. Values marked by asterisks are from reference 7. n.m.- not measured.

Sample	$<\delta_{iso}^{cs}>$ (ppm) ±0.5 ppm	$\langle\|C_Q\|\rangle$ (MHz) ±0.2 MHz	$M_{2(Na-P)}$ (10^6 rad^2 s^{-2}) ±10%	$M_{2(Ga-P)}$ (10^6 rad^2 s^{-2} ± 10%)
$Ga(PO_3)_3$	-	-	-	11.1
$NaPO_3$	-2.0(-1.6*)	1.3 (2.0*)	(3.7*)	-
NaPGa	-2.9(-4.3*)	1.3(1.9*)	(3.0)(3.3*)	11.4
NaPGaW5	-3.2	1.3	(2.9)	11.4
NaPGaW10	n.m	n.m	n.m	9.2
NaPGaW15	-3.8	1.3	(2.6)	n.m

NaPGaW20	n.m	n.m	n.m	8.1
NaPGaW25	-3.9	1.2	(2.2)	6.1

This hypothesis can be tested more rigorously on the basis of $^{23}Na/^{31}P$ magnetic dipole-dipole interactions via the $^{23}Na\{^{31}P\}$ REDOR measurements shown in Figure 7. The $\Delta S/S_0$ values were obtained by integrating the entire line shape and the approximate second moments $M_{2(Na\text{-}P)}$ were obtained by applying a parabolic fit to the REDOR data within the range $\Delta S/S_0 \leq 0.2$, according to Eq. 3. The corresponding dipolar second moments extracted from these measurements, $M_{2(Na-P)}$, are listed in Table 4. In principle the values have to be corrected by calibrating the method with a model compound. As in the present study only compositional trends were of interest, only uncalibrated $M_{2(Na\text{-}P)}$ values are listed. Clearly, $M_{2(Na\text{-}P)}$ shows the expected linear decrease with increasing Na_2WO_4 content (decreasing P/Na ratio), consistent with a random anion distribution. Thus, as tungstate content increases the WO_4^{2-} ions contribute increasingly to the second coordination sphere of the sodium ions, leading to a diminished strength of Na/P interactions. On the other hand, qualitative $^{31}P\{^{23}Na\}$ REAPDOR data (Figure 8) indicate that the second coordination sphere of phosphorus with the sodium cations remains unaltered within experimental error in this compositional series.

Figure 7. $^{23}Na\{^{31}P\}$ REDOR dephasing curves of representative $(NaPO_3)_{80-x}(Ga_2O_3)_{20}(Na_2WO_4)_x$ (x = 0, 5, 15 and 25 mol%) glasses. Solid curves show parabolic fits to the REDOR data within the range $\Delta S/S_0 \leq 0.2$, according to Eq. 3.

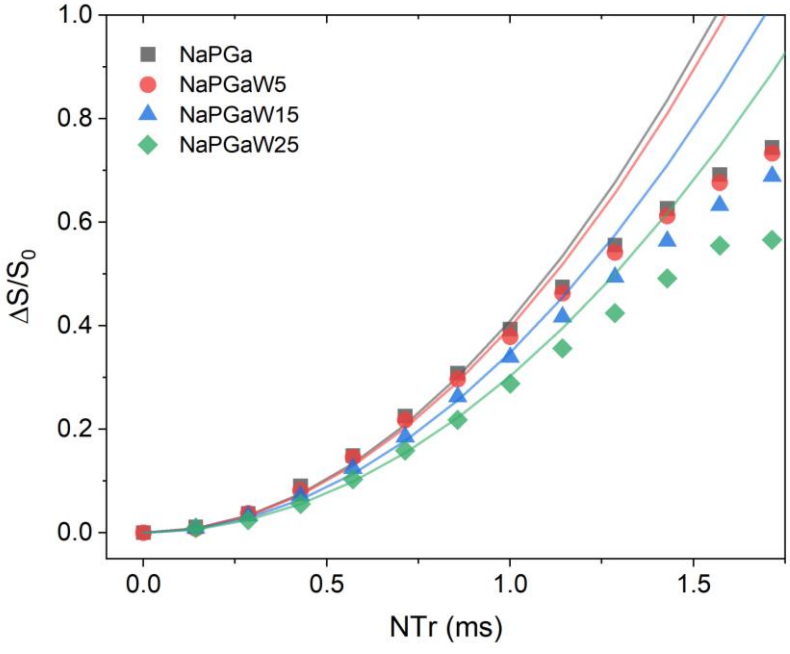

Figure 8. $^{31}P\{^{23}Na\}$ REAPDOR dephasing curves of vitreous $NaPO_3$ and representative $(NaPO_3)_{80-x}(Ga_2O_3)_{20}(Na_2WO_4)_x$ (x = 0, 5, 15 and 25 mol%) glasses.

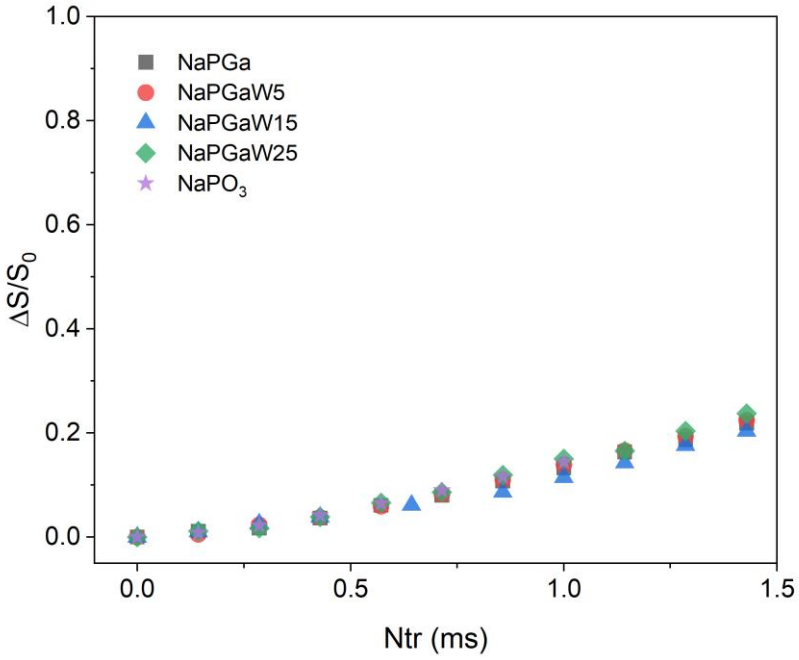

^{71}Ga MAS NMR and ^{71}Ga{^{31}P} REDOR. Figure 9 shows the results from ^{71}Ga MAS-NMR. The spectrum observed for the x = 0 sample agrees very well with the one published earlier [7]. All the glasses exhibit three different signals with peak maxima near 100, 10, and -50 ppm, which can be assigned to four-, five- and six- coordinate gallium species. The relative quantification of these distinct sites is not possible in the present case, as owing to strong anisotropic quadrupolar broadening and a distribution of electric field gradient components, the signals are asymmetrically broadened and show significant spectral overlap with each other and with the spinning sidebands. Qualitatively, the data suggest that with increasing x the Ga(VI) concentration decreases initially, passes through a minimum at x = 10 and then increases again. This result correlates well with the ^{31}P MAS-NMR data, which indicate a significant re-building of the structure at the x = 10 % composition.

Figure 9. ^{71}Ga MAS NMR spectra of the central transition region of $(NaPO_3)_{80-x}(Ga_2O_3)_{20}(Na_2WO_4)_x$ (x = 0, 5, 10, 15, 20 and 25 mol%) glasses.

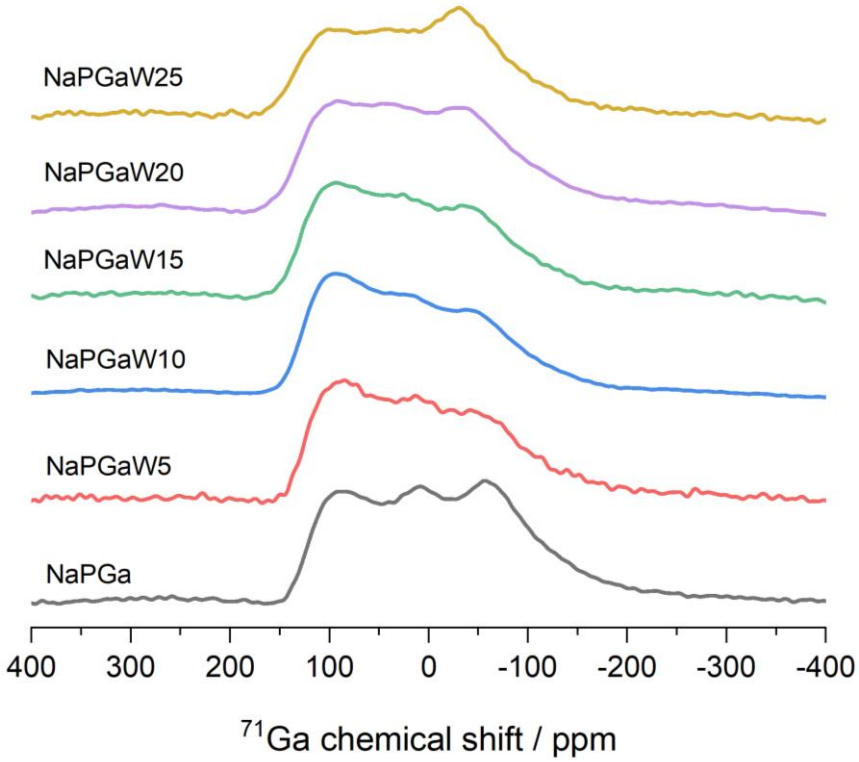

Figure 10 shows results from ^{71}Ga{^{31}P} REDOR experiments. Only average $M_{2(Ga\text{-}P)}$ values according to the parabolic fit to the REDOR data, eq. (3) are estimated by integrating the whole ^{71}Ga central transition signal, as the individual Ga(IV), Ga(V), and Ga(VI) contributions are impossible to separate, owing to the overlap of MAS central peaks with one another and with spinning sidebands arising from the anisotropic second-order quadrupolar broadening effects. However, dipolar ^{31}P recoupling did not affect the overall lineshape appearance (data not shown), indicating that the ^{71}Ga-^{31}P dipolar interactions are of comparable strengths for the gallium species in all three of their different coordination states.

For the x = 0 glass a $M_{2(Ga-P)}$ value of 11.4×10^6 rad^{2}s^{-2} was determined, which is in good agreement with the values previously reported by Ren and Eckert [7].They report a value of 8.4×10^6 rad^{2}s^{-2}, which can be corrected to 11.2×10^6 rad^{2}s^{-2}, estimating a calibration factor f = *0.75* based on the experimental values reported by them for the $Ga(PO_3)_3$ crystalline compound. With increasing Na_2WO_4 content, $M_{2(Ga\text{-}P)}$ decreases significantly (Table 4), indicating that the ^{71}Ga-^{31}P dipole coupling is significantly decreased as other atoms (tungsten and/or gallium) are appearing in appreciable numbers in the second coordination sphere of Ga^{3+}. A similar observation has been made in binary Ga_2O_3-$NaPO_3$ glasses, where a drop in $M_{2(Ga\text{-}P)}$

at high Ga contents could be related to the onset the formation of clusters forming Ga-O-Ga linkages [7].

Figure 10. ^{71}Ga{^{31}P} REDOR dephasing curves of representative $(NaPO_3)_{80-x}(Ga_2O_3)_{20}(Na_2WO_4)_x$ (x = 0, 5, 10, 20 and 25 mol%) glasses. Solid curves show parabolic fits to the REDOR data within the range $\Delta S/S_0 \leq 0.2$, according to Eq. 3.

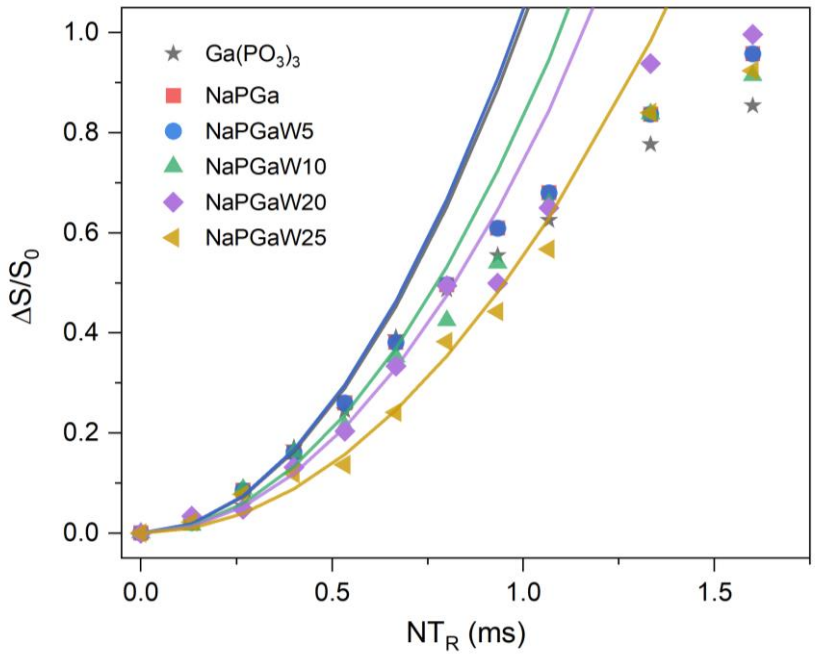

4.4 Discussion

The NMR results discussed above reveal that the successive replacement of $NaPO_3$ by Na_2WO_4 in the $(NaPO_3)_{80-x}(Ga_2O_3)_{20}(Na_2WO_4)_x$ system leads to a progressive reduction of the number of P-O-P linkages. While the average Ga coordination number remains virtually unchanged, the REDOR data indicate significant changes in the local Ga connectivity and sodium coordination, while the effect of on the glass transition temperature is only moderate. To understand the behavior displayed in Figure 2a, a discussion in connection with previous results obtained on the base glass system $(100\text{-}y)NaPO_3 - yGa_2O_3$ [7], is instructive. In that system the gallium species are present in four-, five-, and six-coordination, forming Ga^4, Ga^5 and Ga^6 units with the second coordination sphere dominated by meta-, pyro, and orthophosphate species, Q^2, Q^1, and Q^0, respectively. The structure of glasses with $y < 15$ is dominated by Q^2 and Q^1 species, and Ga is dominantly six-coordinated, while in glasses with $y > 15$ Q^0 species dominate and a higher fraction of gallium is four-coordinated [7].

As shown in reference 7 the value of the glass transition temperature in this binary glass system is strongly correlated with the fraction [BO] of oxygen atoms that are bridging between network former units. T_g increases steeply within the concentration range $0 \leq y \leq 15$, as the cross-linking of

metaphosphate chains by six-coordinate gallium produces increasing amounts of Ga-O-P linkages with increasing Ga_2O_3 content. In contrast, within the interval $15 \leq y \leq 20$ T_g remains virtually constant, i.e. independent of y. This is the region for which the ^{71}Ga NMR data indicate the dramatic reduction in average Ga coordination number mentioned above. The latter effect balances the increase in [BO] due to the increased $Ga_2O_3/NaPO_3$ ratio in a way that [BO] remains more or less constant in this interval [7]. At y-values > 20 (corresponding to $Ga_2O_3/NaPO_3$ ratios > 0.25) the Ga coordination change is completed and [BO] keeps increasing again, along with an analogous trend in the T_g values. The composition y = 20 ($Ga_2O_3/NaPO_3$ ratio of 0.25), forms the base glass of the present ternary system, $(NaPO_3)_{80-x}(Ga_2O_3)_{20}(Na_2WO_4)_x$. Here the partial replacement of the $NaPO_3$ component by Na_2WO_4 implies an effective increase in the $Ga_2O_3/NaPO_3$ ratio to 20/(80-x), ranging from 0.27 (x = 5) to 0.36 (x = 25). Thus, the increase of T_g as a function of x seen in Figure 2 can be explained again in terms of an increase in [BO]. The subsequent decrease of T_g for the samples with x = 0.2 and 0.25 cannot be rationalized in this fashion. We speculate that in this concentration range the tungstate species, assumed to be WO_4^{2-} ions become structurally increasingly relevant, contributing not only to an increase in molar volume but also to a decrease in thermal stability. Finally. the good chemical stability of these glasses can be attributed to the depletion of P-O-P linkages, which are known to be hydrolytically sensitive.

4.5 Conclusions

In summary the results of the present study indicate that in the glass system $(NaPO_3)_{80-x}(Ga_2O_3)_{20}(Na_2WO_4)_x$ (x = 0, 5, 10, 15, 20 and 25 mol%) the partial substitution of the $NaPO_3$ component by Na_2WO_4 results in significant network reconstruction, resulting in an increase of molar volume (decreased oxygen packing density), accompanied by a slight increase in T_g values, which pass through a shallow maximum near x = 10 to 15. Q^1 units, containing P-O-P linkages are successively depleted and found to be in low concentrations above the x = 10 level. While the structure of these glasses is dominated by Q^0 units, connected to both gallium and tungstate species, ^{71}Ga{^{31}P} REDOR data suggest significant decreases in the extent of gallium-phosphorus connectivity with increasing Na_2WO_4 content. Finally, monotonic changes in both ^{23}Na chemical shifts and $M_{2(Na-P)}$ values indicate that the anionic surroundings of the sodium ions evolve from a pure phosphate to a mixed phosphate/tungstate environment.

ACKNOWLEDGMENTS

Authors would like to acknowledge the Brazilian funding agencies FAPESP (CEPID Project 2013/07793-6), and CNPq grant number 311828/2021-3 (ASSC), 310870/2020-8 (HE) and 311069/2020-7 (M.O.Jr.). GG acknowledges financial support from FAPESP grant 2018/03931-9, for a postdoctoral fellowship. S.H.S. thanks for financial support by a SPEC-FAPESP grant, process number 15/22828-6.

AUTHOR CONTRIBUTIONS

Thiago A. Lodi: Conceptualization, Data curation, Methodology, Investigation, Data curation, Writing- Original draft preparation.: **Gustavo Galleani**: Conceptualization, Data curation, Investigation, Writing - Reviewing and Editing. **Marcos de O. Junior***:* Data curation, Investigation, Writing- Reviewing and Editing. **Silvia H. Santagneli:** Data curation, Investigation, Writing- Reviewing and Editing. **Hellmut Eckert:** Data curation, Investigation, Writing- Reviewing and Editing, Funding. **Andrea S. S. de Camargo:** Conceptualization, Writing- Reviewing and Editing, Supervision, Funding.

REFERENCES

[1] Caurant, D.; Majérus, O. *Glasses and Glass-Ceramics for Nuclear Waste Immobilization*; 2021; Vol. 2–3. https://doi.org/10.1016/B978-0-12-818542-1.00090-4.

[2] Hench, L. L. The Story of Bioglass®. *J Mater Sci Mater Med* **2006**, *17* (11), 967–978. https://doi.org/10.1007/s10856-006-0432-z.

[3] Bhemarajam, J.; Prasad, P. S.; Mohan Babu, M.; Prasad, M. Spectroscopic and Optical Investigations on Er^{3+}/Yb^{3+}co-Doped Bismuth–Boroleadlithium Glasses for Solid State Laser Applications. *Opt Mater (Amst)* **2021**, *122* (PA), 111657. https://doi.org/10.1016/j.optmat.2021.111657.

[4] El-Meliegy, E.; Farag, M. M.; Knowles, J. C. Dissolution and Drug Release Profiles of Phosphate Glasses Doped with High Valency Oxides. *J Mater Sci Mater Med* **2016**, *27* (6), 1–10. https://doi.org/10.1007/s10856-016-5711-8.

[5] Guesmia, N.; Hamzaoui, M.; Beghdadi, L.; Soltani, M. T.; Ligny, D. De. Glass Formation, Physical and Structural Investigation Studies of the (90-x) Sb_2O_3-10WO_3-X$NaPO_3$ Glasses. *Mater Today Commun* **2022**, *30* (January), 103226. https://doi.org/10.1016/j.mtcomm.2022.103226.

[6] Hee, P.; Christensen, R.; Ledemi, Y.; Wren, J. E. C.; Dussauze, M.; Cardinal, T.; Fargin, E.; Kroeker, S.; Messaddeq, Y. Properties and Structural Investigation of Gallophosphate Glasses by ^{71}Ga and ^{31}P Nuclear Magnetic Resonance and Vibrational Spectroscopies. *J Mater Chem C Mater* **2014**, *2* (37), 7906–7917. https://doi.org/10.1039/c4tc01024h.

[7] Ren, J.; Eckert, H. Intermediate Role of Gallium in Oxidic Glasses: Solid State NMR Structural Studies of the Ga_2O_3-$NaPO_3$ System. *J Phys Chem C* **2014**, *118* (28), 15386–15403. https://doi.org/10.1021/jp504023k.

[8] Caron, A.; Doumert, B.; Tricot, G. The xGa_2O_3-(100 - x)$NaPO_3$ Glass System: Preparation, Properties and Structural Analysis by Solid State NMR. *Mater Chem Phys* **2014**, *147* (3), 1165–1170. https://doi.org/10.1016/j.matchemphys.2014.06.074.

[9] de Araujo, C. C.; Strojek, W.; Zhang, L.; Eckert, H.; Poirier, G.; Ribeiro, S. J. L.; Messaddeq, Y. Structural Studies of $NaPO_3$-WO_3 Glasses by Solid State NMR and Raman Spectroscopy. *J Mater Chem* **2006**, *16* (32), 3277–3284. https://doi.org/10.1039/b605971f.

[10] Poirier, G.; Messaddeq, Y.; Ribeiro, S. J. L.; Poulain, M. Structural Study of Tungstate Fluorophosphate Glasses by Raman and X-Ray Absorption Spectroscopy. *J Solid State Chem* **2005**, *178* (5), 1533–1538. https://doi.org/10.1016/j.jssc.2004.10.032.

[11] Lodi, T. A.; dos Santos, J. F. M.; Galleani, G.; Jacobsohn, L. G.; Catunda, T.; de Camargo, A. S. S. Promising Tb^{3+}-Doped Gallium Tungsten-Phosphate Glass Scintillator: Spectroscopy, Energy Transfer and UV/X-Ray Sensing. *J Alloys Compd* **2022**, *904*, 164016. https://doi.org/10.1016/j.jallcom.2022.164016.

[12] Gullion, T.; Schaefer, J. Rotational-Echo Double-Resonance NMR. *J Magn Reson* **2011**, *213* (2), 413–417. https://doi.org/10.1016/j.jmr.2011.09.003.

[13] Bertmer, M.; Eckert, H. Dephasing of Spin Echoes by Multiple Heteronuclear Dipolar Interactions in Rotational Echo Double Resonance NMR Experiments. *Solid State Nucl Magn Reson* **1999**, *15* (3), 139–152. https://doi.org/10.1016/S0926-2040(99)00050-8.

[14] Ba, Y.; Kao, H. M.; Grey, C. P.; Chopin, L.; Gullion, T. Optimizing the ^{13}C-^{14}N REAPDOR NMR Experiment: A Theoretical and Experimental Study. *J Magn Reson* **1998**, *133* (1), 104–114. https://doi.org/10.1006/jmre.1998.1422.

[15] Han, O. H.; Timken, H. K. C.; Oldfield, E. Solid-State "Magic-Angle" Sample-Spinning Nuclear Magnetic Resonance Spectroscopic Study of Group III-V (13-15) Semiconductors. *J Chem Phys* **1988**, *89* (10), 6046–6052. https://doi.org/10.1063/1.455418.

[16] Hammad, A. H.; Marzouk, M. A.; ElBatal, H. A. The Effects of Bi_2O_3 on Optical, FTIR and Thermal Properties of SrO-B_2O_3 Glasses. *Silicon* **2016**, *8* (1), 123–131. https://doi.org/10.1007/s12633-015-9283-x.

[17] Farouk, M.; Samir, A.; Ibrahim, A.; Farag, M. A.; Solieman, A. Raman, FTIR Studies and Optical Absorption of Zinc Borate Glasses Containing WO_3. *Appl Phys A* **2020**, *126* (9), 1–8. https://doi.org/10.1007/s00339-020-03890-y.

[18] Gunhakoon, P.; Thongklom, T.; Sopapan, P.; Laopaiboon, J.; Laopaiboon, R.; Jaiboon, O. Influence of WO_3 on Elastic and Structural Properties of Barium-Borate-Bagasse-Cassava Rhizome Glass System. *Mater Chem Phys* **2020**, *243* (October 2019), 122587. https://doi.org/10.1016/j.matchemphys.2019.122587.

[19] Manzani, D.; Araújo, C. B. de; Boudebs, G.; Messaddeq, Y.; Ribeiro, S. J. L. The Role of Bi_2O_3 on the Thermal, Structural, and Optical Properties of Tungsten-Phosphate Glasses. *J Phys Chem B* **2013**, *117*, 408−414. https://doi.org/10.1021/jp3097296.

[20] Guérineau, T.; Loi, L.; Petit, Y.; Danto, S.; Fargues, A.; Canioni, L.; Cardinal, T. Structural Influence on the Femtosecond Laser Ability to Create Fluorescent Patterns in Silver-Containing Sodium-Gallium Phosphate Glasses. *Opt Mater Express* **2018**, *8* (12), 3748. https://doi.org/10.1364/ome.8.003748.

[21] Hee, P.; Christensen, R.; Ledemi, Y.; Wren, J. E. C.; Dussauze, M.; Cardinal, T.; Fargin, E.; Kroeker, S.; Messaddeq, Y. Properties and Structural Investigation of Gallophosphate Glasses by ^{71}Ga and ^{31}P Nuclear Magnetic Resonance and Vibrational Spectroscopies. *J Mater Chem C Mater* **2014**, *2* (37), 7906–7917. https://doi.org/10.1039/c4tc01024h.

[22] Belkébir, A.; Rocha, J.; Esculcas, A. P.; Berthet, P.; Gilbert, B.; Gabelica, Z.; Llabres, G.; Wijzen, F.; Rulmont, A. Structural Characterization of Glassy Phases in the System Na_2O-Ga_2O_3-P_2O_5 by MAS and Solution NMR and Vibrational Spectroscopy: II. Structure of the Phosphate Network. *Spectrochim Acta A Mol Biomol Spectrosc* **2000**, *56* (3), 435–446. https://doi.org/10.1016/S1386-1425(99)00117-1.

[23] Munhoz, J. F. V. L.; Santagneli, S. H.; de Oliveira, M.; Rodrigues, A. C. M.; Eckert, H.; Nalin, M. Glasses in the $NaPO_3$-WO_3-NaF Ternary System: Preparation, Physical Properties and Structural Studies. *J Non Cryst Solids* **2019**, *505* (September 2018), 379–389. https://doi.org/10.1016/j.jnoncrysol.2018.10.043.

[24] Manzani, D.; Fernandes, R. G.; Messaddeq, Y.; Ribeiro, S. J. L.; Cassanjes, F. C.; Poirier, G. Thermal, Structural and Optical Properties of New Tungsten Lead-Pyrophosphate Glasses. *Opt Mater (Amst)* **2011**, *33* (12), 1862–1866. https://doi.org/10.1016/j.optmat.2011.02.041.

[25] Dousti, M. R.; Poirier, G. Y.; de Camargo, A. S. S. Tungsten Sodium Phosphate Glasses Doped with Trivalent Rare Earth Ions (Eu^{3+}, Tb^{3+}, Nd^{3+} and Er^{3+}) for Visible and near-Infrared Applications. *J Non Cryst Solids* **2020**, *530*. https://doi.org/10.1016/j.jnoncrysol.2019.119838.

[26] Velli, L. L.; Varsamis, C. P. E.; Kamitsos, E. I. Structural Investigation of Metaphosphate Glasses. *Phys Chem Glasses* **2005**, *46* (June), 178–181.

[27] Möncke, D.; Eckert, H. Review on the Structural Analysis of Fluoride-Phosphate and Fluoro-Phosphate Glasses. *J Non Cryst Solids X* **2019**, *3* (l), 100026. https://doi.org/10.1016/j.nocx.2019.100026.

[28] d'Espinose de Lacaillerie, J. B.; Fretigny, C.; Massiot, D. MAS NMR Spectra of Quadrupolar Nuclei in Disordered Solids: The Czjzek Model. *J Magn Reson* **2008**. https://doi.org/10.1016/j.jmr.2008.03.001.

[29] Anissimova, N.; Glaum, R. Refinement of the Superstructure of C-Type Gallium Tris(Metaphosphate), $Ga(PO_3)_3$. *Z Anorg Allg Chem* **1998**, *624* (12), 2029–2032. https://doi.org/10.1002/(SICI)1521-3749(1998120)624:12<2029::AID-ZAAC2029>3.0.CO;2-Q.

[30] van Vleck, J. H. The Dipolar Broadening of Magnetic Resonance Lines in Crystals. *Phys Rev* **1948**, *74*, 679. https://doi.org/10.1103/PhysRev.74.1168.

5 TUNGSTEN GALLIUM-PHOSPHATE GLASSES AS A PROMISING INTRINSIC SCINTILLATOR

Thiago A. Lodi[a,*], Gustavo Galleani[a], Leonnam G. Merízio[a], Luis G. Jacobsohn[b], Valmor R. Mastelaro[a], Andrea S. S. de Camargo[a,*]

[a] São Carlos Institute of Physics, University of São Paulo, Av. Trabalhador Saocarlense 400, São Carlos, SP, 13566-590, Brazil.

[b] Department of Materials Science and Engineering, Clemson University, 515 Calhoun Dr, Clemson, SC, 29634, United States of America.

DOI: *10.1016/j.jnoncrysol.2022.122097*

ABSTRACT

Tungsten gallium phosphate glasses with composition $NaPO_3$-$20Ga_2O_3$-xNa_2WO_4 (x = 0, 1, 3, 5 and 10% mol) were synthesized by the melt-quenching technique with high chemical stability and excellent optical properties and evaluated as potential scintillators. Fourier-transform infrared measurements showed a decrease in the amount of OH groups for increasing Na_2WO_4 contents, while X-ray photoelectron spectroscopy revealed the presence of sole W^{6+} species. Optical transmission measurements showed a high level of transmittance of ~90% over a broad spectral range from 400 to 2500 nm. Luminescence was found to correspond to a broad emission characteristic of the WO_4^{2-} complex that can be excited by ultraviolet and X-rays with average lifetimes ranging from 32 to 20 ms. At cryogenic temperatures, the NaPGaW glasses showed a significant increase in the luminescence emission.

5.1 Introduction

Ionizing radiation, such as X-rays, is present in medical, scientific and security applications such as radiography, crystallography, elemental identification and surveillance [1]. Particularly, the materials science research has been greatly benefited opening a new era of X-rays imaging analysis [2]. In order to ensure effective and safe use of X-rays, proper handling, detection, and dose determination are paramount. In terms of X-ray detection, most of the detectors are based on the scintillation phenomenon which consists in the conversion of the ionizing radiation into ultraviolet (UV)-visible light [3]. Scintillation can be categorized as either extrinsic when optically active ions are doped into the scintillator host material, or intrinsic when functional groups within the structure of the material are responsible for the light emission. Whichever the mechanism, the emission from the scintillator is collected and converted into an electrical signal by highly sensitive photomultiplier tubes (PMT) [2,4].

Traditional crystalline scintillators present optimum performance but the manufacturing methods of single crystals are usually complex, costly, time-consuming and limited with respect to obtaining large size materials, hindering widespread commercial use of scintillators. The advantages of the chemical stability, lower fabrication cost, already-in-place high-volume industrial fabrication of glasses, in various sizes and shapes are strong incentives for the development of new glass scintillators [5]. Glass compositions containing tungsten oxy-anionic complexes such as $[WO_6]^{6-}$ and $[WO_4]^{2-}$ can be a particularly promising alternative for monocrystalline intrinsic scintillators. Their emission generates a high number of photons over a broad spectral region possibly resulting in superior signal-to-noise ratios and short integration times. To the best of our knowledge, tungsten gallium-phosphate glasses have not been investigated as scintillators. In this work, we report on the fabrication and characterization of glasses in the compositional system $NaPO_3$ - Ga_2O_3 - Na_2WO_4 with variable concentration of tungsten as potential scintillators for X-ray detection.

5.2 Experimental procedure

Tungsten gallium-phosphate glasses, hereafter abbreviated as NaPGaW, were prepared via the melt-quenching technique according to the stoichiometric compositions (80 - x) $NaPO_3$ - 20 Ga_2O_3 - x Na_2WO_4 (x = 0, 1, 3, 5 and 10% mol) as summarized in Table 1. The powders of the raw materials were thoroughly mixed in an agate mortar and melted in a platinum crucible

in a furnace at 1000 - 1050 ºC, depending on the Na_2WO_4 content. Approximately 8 × 8 mm^2 and 2.5 mm thick polished plates of the NaPGaW glasses were used for the optical transmittance, absorption, Fourier-transform infrared (FTIR) absorption, photoluminescence excitation (PLE) and emission (PL) measurements at room temperature. For the photophysical characterization, we secured that all the studied samples had the same dimensions. For the X-ray photoelectron spectroscopy (XPS) and radioluminescence (RL) measurements, the glasses were powdered and used in powder form.

Table 5. Glass label and nominal composition (mol%) of NaPGa and NaPGaW glasses.

Glass label	Nominal composition (mol%)		
	$NaPO_3$	Ga_2O_3	Na_2WO_4
NaPGa	80	20	-
NaPGaW1	79	20	1
NaPGaW3	77	20	3
NaPGaW5	75	20	5
NaPGaW10	70	20	10

FTIR analysis was carried out with an Agilent Cary 630 FTIR operating in attenuated total reflection (ATR) mode. XPS analysis was performed with a spectrometer ScientaOmicron ESCA+ XPS equipped with a high-performance hemispherical analyzer (EAC2000) with monochromatic Al Kα radiation ($h\nu$ = 1486.6 eV) as the excitation source. XPS spectra were recorded at constant pass energy of 20 eV with 0.05 eV per step for the high-resolution spectra and the data were analyzed using the CASA XPS software. The optical transmission and absorption measurements were carried out using a UV–Vis-NIR Perkin-Elmer double-beam spectrometer model Lambda 1050 in the range 250-2500 nm, with a spectral resolution of 1 nm. The PLE and PL spectra of NaPGaW glasses were recorded with a HORIBA Jobin Yvon spectrofluorometer model Fluorolog-3 equipped with a 450 W CW Xenon arc lamp as the excitation source. The excited state lifetime values were measured in the same spectrofluorometer using a pulsed Xe lamp, and the decay curves were analyzed using the DAS6 software. Temperature-dependent experiments (80-300 K) were carried using the same spectrometer (Fluorolog-3) coupled to a temperature controller model Linkam THMS600. RL

measurements were recorded with a Freiberg Instruments Lexsyg Research spectrofluorometer using a Varian Medical Systems VF-50J X-ray tube with a tungsten target as the X-ray source. More details can be found in [6].

5.3 Results and discussion

Figure 1(a) shows a photograph of a representative NaPGaW glass in ambient light highlighting its high optical transmittance, and 1(b) shows the luminescence of the whole series of glasses under UV excitation where the glasses were placed in ascending order of Na_2WO_4 content (left to right). The first glass shown on the left in Figure 1(b) does not have Na_2WO_4 in its composition. All NaPGaW glasses are colorless, transparent, and are non-hygroscopic.

Figure 1. Photographs of the NaPGa and NaPGaW glass samples: (a) a representative glass in ambient light and (b) the whole series of luminescent glasses under UV light (300 nm).

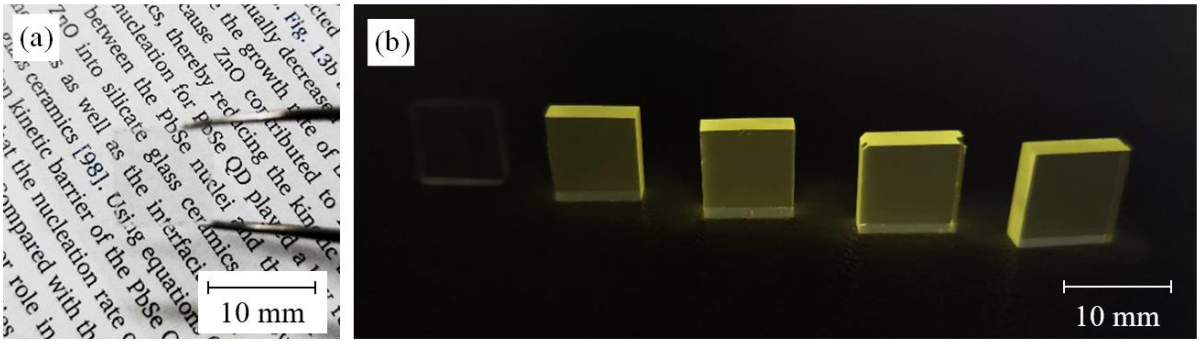

Fourier Transform Infrared (FTIR). FTIR spectra of NaPGa and NaPGaW glasses in the frequency region between 4000 and 700 cm^{-1} are presented in Figure 2. A broad band centered at approximately 3300 cm^{-1} (a) can be observed, which is attributed to symmetric stretching of O-H groups in H_2O molecules present in the glass structure [4]. In the inset, a magnified view of this region is presented, evidencing the decrease in this band as a function of Na_2WO_4 content. This indicates the increase in chemical stability of the NaPGaW glasses for increasing Na_2WO_4 contents. The band located between 2300 and 2200 cm^{-1}, observed in the spectra of all glasses, is assigned to molecular CO_2 present in the atmosphere [7]. The band centered at 1640 cm^{-1} (b) is assigned to the bending vibration mode of OH groups [4,8]. The low relative intensity of the OH- related bands indicates the excellent quality of the NaPGaW glasses. In the frequency range 1300 to 650 cm^{-1}, four bands can be observed. The band at 1150 cm^{-1} (c), evident in the spectra of the NaPGa, NaPGaW5 and NaPGaW10 samples, is attributed

to the asymmetric vibration of PO_4 units. The band at 1050 cm^{-1} (d) is attributed to symmetric stretching modes of tetrahedral Q^0 groups $(PO_4)^{3-}$ [9], while the band at 870 cm^{-1} is assigned to P-O-P asymmetric bending vibrations. These last three bands do not change significantly with increasing Na_2WO_4 content. A different behavior can be noticed at 750 cm^{-1}, a band attributed to the presence of symmetric stretching modes of the bridging oxygen (O_B) bonded to a phosphorus atom in a Q^2 phosphate tetrahedron [10]. This band disappears when Na_2WO_4 is added, indicating that the addition of Na_2WO_4 favors the depolymerization of the phosphate network.

Figure 2. FTIR spectra of representative glasses. The inset shows a magnified view of the region where the stretching mode of OH is located.

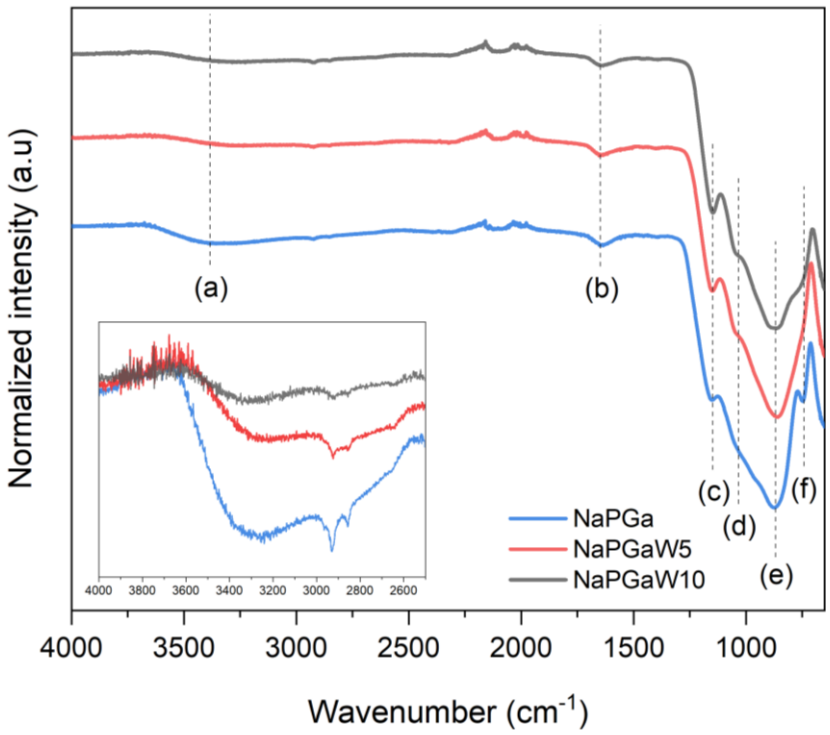

X-ray photoelectron spectroscopy (XPS). Seeking for a better comprehension of the origin of the broadband emission of NaPGaW glasses (discussed below), an investigation of the samples by high-resolution XPS was carried out. Figure 3 shows the W 4f (a), Ga 2p (b), and P 2p (c) XPS spectra of the representative glass NaPGaW5. In the XPS spectrum of W 4f level, two peaks centered at 37.7 and 35.6 eV are fitted by Lorentzian-Gaussian and are attributed to the W $4f_{5/2}$ and W $4f_{7/2}$ levels of the W^{6+} ion, respectively. The presence of other oxidation states of W was not observed, confirming that the broadband observed in the visible

region is attributed to hexavalent tungsten. Furthermore, Figures 3 (b) and (c) presents the XPS spectra of the Ga 2p and P 2p core levels, respectively. For the Ga 2p core level, two peaks centered at 1145.2 and 1118.3 eV can be observed, which are, respectively, the binding energy (E_b) of electrons in the $2p_{1/2}$ and $2p_{3/2}$ levels of gallium in the Ga^{3+} valence state [11]. The XPS spectrum of the P 2p core level (see Fig 11c), in turn, is decomposed into two peaks with E_b = 134.2 and 133.1 eV and with an energy difference between these peaks ΔE_b = 0.9 eV, ΔE_b characteristic of $2p_{1/2}$ and P $2p_{3/2}$ [12]. The binding energies of these elements for all glass samples can be found in Table 2, which clearly shows that there are no significant changes as a function of the Na_2WO_4 content. Interestingly, we did not observe any significant change in the W 4f spectrum of the NaPGaW10 glass that could corroborate our hypothesis of the presence of different W species in this glass in comparison to the other glasses with lower concentrations of Na_2WO_4. We tentatively attribute this to the small concentration of the other W species coupled to the sensitivity of the XPS detection system.

Figure 3. XPS high-resolution spectra of a) tungsten 4f, b) gallium 2p, and c) phosphor 2p of the NaPGaW5 glass.

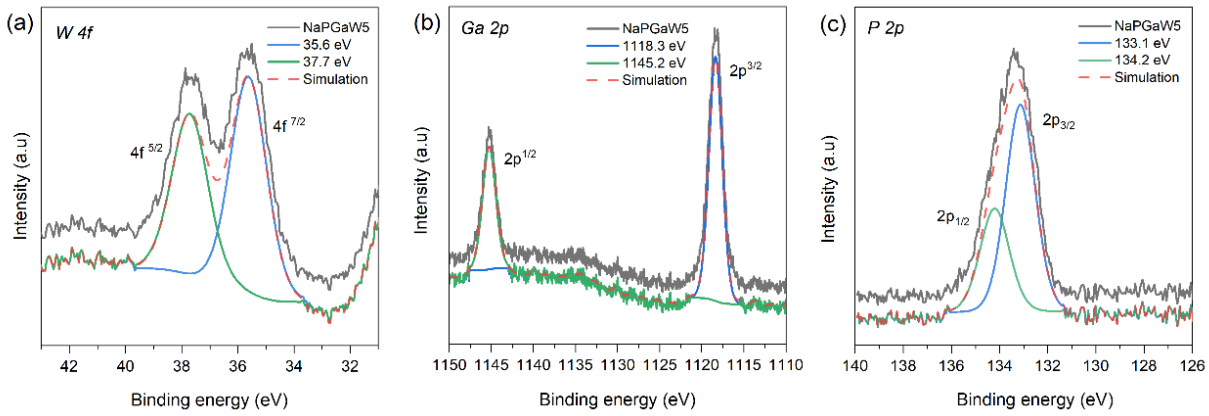

Table 2. Peak positions (in eV) obtained from curve fitting of the P 2p, Ga 2p, and W 4f XPS spectra of the NaPGa and NaPGaW glasses.

Glass label	Peak position (eV)		
	W 4f	Ga 2p	P 2p
NaPGa	-	1144.8 1118.0	133.9 132.9
NaPGaW1	37.6 35.5	1145.1 1118.2	134.0 133.0
NaPGaW3	37.7 35.5	1145.2 1118.3	134.0 133.0
NaPGaW5	37.7 35.6	1145.2 1118.3	134.1 133.2
NaPGaW10	37.6 35.5	1145.2 1118.3	134.0 133.0

Optical Transmission Spectroscopy. Figure 4 shows the transmission spectra of NaPGaWx (x = 0, 1, 3, 5 and 10 mol%) glasses. All the samples exhibit high transparency (≈ 90%) in the 400 to 2500 nm range, indicating that these glasses can be absorption free hosts for various rare-earth ions. By increasing the content of Na_2WO_4, the absorption edge of the NaPGaW glasses shifts towards longer wavelengths (*cf.* Fig. 4). This shift can be explained by the increase of the covalent character of the vitreous network, which is attributed to the insertion of WO_n polyhedra between PO_4 units of the phosphate network [13]. Since the optical energy gap arises from the electronic transitions from the conduction band to the valence band, it can

be inferred that the progressive incorporation of Na_2WO_4 in the vitreous network reduces the optical energy gap between these bands.

Figure 4. (a) Transmittance spectra of the NaPGaW glasses in the UV, visible, and near-infrared ranges and (b) redshift in function of tungsten content.

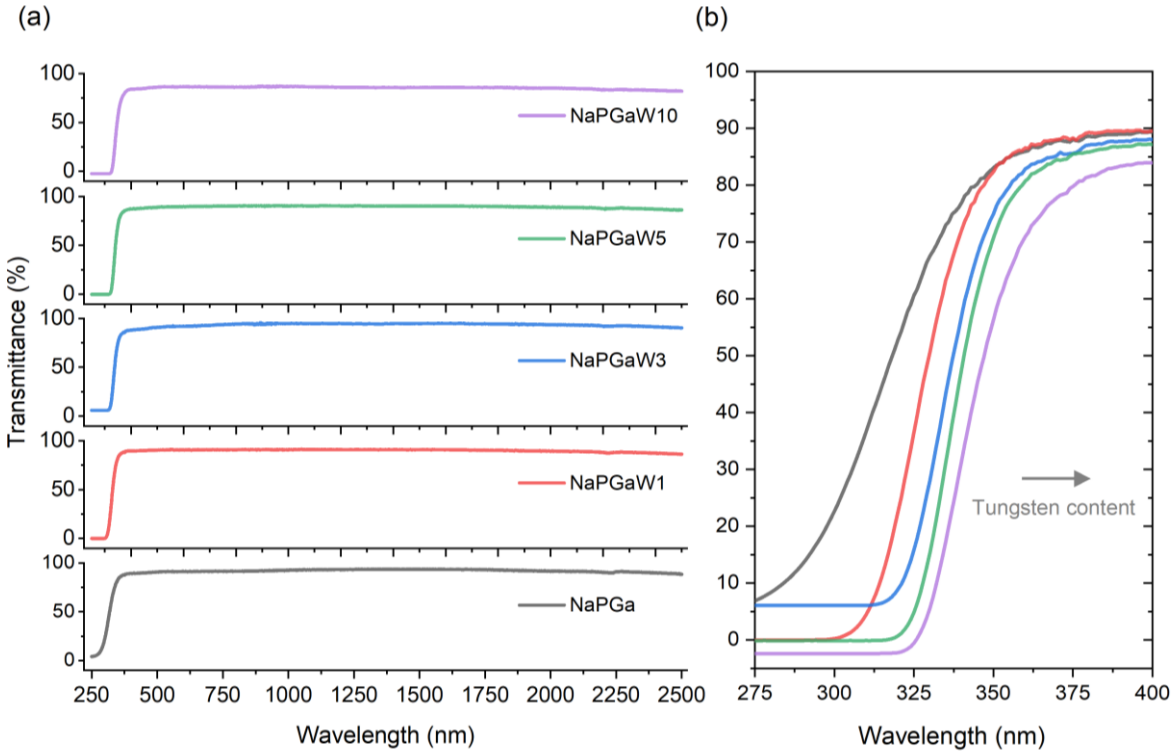

Photoluminesce excitation and emission. The photoluminescence excitation and emission spectra of NaPGa and NaPGaW glasses at room temperature are shown in Figure 5. It is noted that the excitation spectra obtained by monitoring the emission at 570 nm could only be collected starting at 280 nm due to limitations of the spectrofluorometer detector. Consequently, only the excitation spectrum of the NaPGaW5 glass is presented for illustrative purposes.

Figure 5. PLE excitation spectrum of NaPGaW5 monitoring the emission at 570 nm (dashed green line), and PL emission of NaPGa and NaPGaW glasses measured under excitation at 290 nm (solid lines).

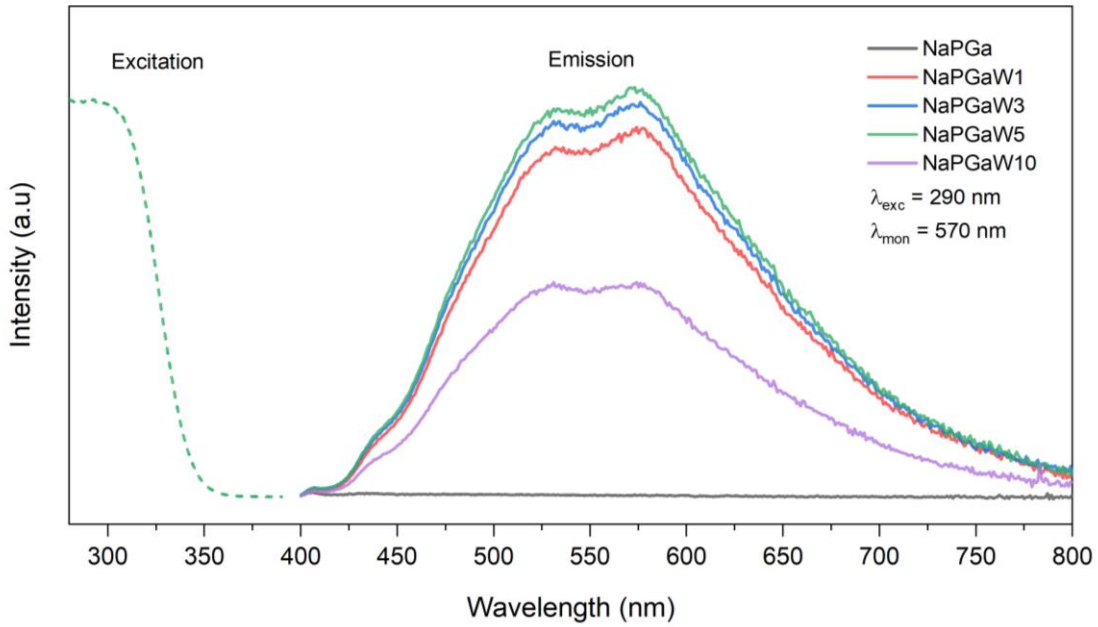

In phosphors, crystals, and films of tungstates like $CaWO_4$, $BaWO_4$, $SrWO_4$, and $PbWO_4$ [14-16], the excitation band covers a broad range within the 200 ~ 350 nm spectral region, peaking at about 280 nm. This excitation band is ascribed to the charge transfer band (CTB) from the oxygen 2p orbitals to one of the empty tungsten 5d orbitals within the WO_4^{2-} groups. This is consistent with our results shown in Fig. 5.

The emission spectra of the NaPGa and NaPGaW glasses were collected upon excitation at 290 nm (solids lines in Fig. 6). The glass without Na_2WO_4 (black line) does not present emission in this region, confirming the emission observed in the other glasses to be related to the tungstate groups. The NaPGaW*x* glasses with x = 1, 3, 5, and 10 mol% Na_2WO_4 present a broad emission in the spectral range from 420 to 800 nm. The origin of the broad visible emission band presented by tungstates, as well as molybdates, is quite polemical in the literature. It is generally accepted, however, that the emission of tungstates and molybdates like Na_2WO_4, $CaWO_4$, and $CaMoO_4$ with scheelite structure results from the radiative recombination of self-trapped excitons (STEs) localized at WO_4^{2-} molecular ions [16-18]. It is also known that Na_2WO_4 is built up by isolated tetrahedral WO_4^{2-} units and that all the bonds in the structure are terminal (i.e., two W=O and two W-O^- [19]), as schematized in Figure 6. As indicated in the energy level diagram of Fig. 6, when excited by short wavelength radiation ($^1A_1 \rightarrow {}^1T_1, {}^1T_2$ transitions) the WO_4^{2-} complex yields two emissions at 460 nm and at 520 nm. The

blue emission ($^3T_2 \rightarrow {}^1A_1$ transition) is attributed to the WO_4 tetrahedron while the green one ($^3T_1 \rightarrow {}^1A_1$) is attributed to WO_3 defect centers associated with oxygen vacancies, however, sometimes it is attributed to intrinsic transitions in the WO_4^{2-} complex [20]. These two emissions are clearly present in the spectra of NaPGaW glasses. Furthermore, a component between 600 - 650 nm also seems to be convoluted in the spectra of Figure 5, which has been previously observed and is believed to originate from the transitions in a WO_3 group or higher tungstate complexes, which once again indicates the presence of a variety of tungsten species in the glasses [15,20].

Figure 6. *Left:* Structure of Na_2WO_4 and WO_4^{2-} tetrahedra. *Right:* Schematic energy level diagram (not to scale) of the emission processes in the WO_4^{2-} complex in the scheelite structure**.**

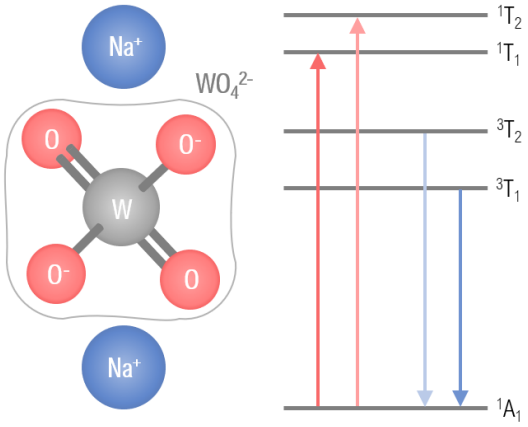

Another interesting aspect shown in Fig. 5 is the fact that the intensity of the broad emission band increases with the increasing concentration of Na_2WO_4 up to 5 mol%, and then decreases for higher concentrations. We hypothesize that for higher tungsten concentrations, the formation of additional anionic species such as the complex W_2O_7 is highly probable and the variations in intensity are related to the relative contributions of these different species.

To evaluate the colorimetric performance of the NaPGaW glasses, the emission colors were analyzed using the Commission Internationale de l'Eclairage (CIE, 1931) chromaticity coordinates (x, y). For the most emissive NaPGaW5 glass, the CIE coordinates are shown in Figure 7. They are x = 0.38 and y = 0.46 while the correlated color temperature (CCT) equals 4300 K. The other glasses showed no significant differences in the values of chromaticity coordinates and color temperature and thus are not shown in Figure 7.

Figure 7. CIE 1931 diagram of the representative NaPGaW5 glass.

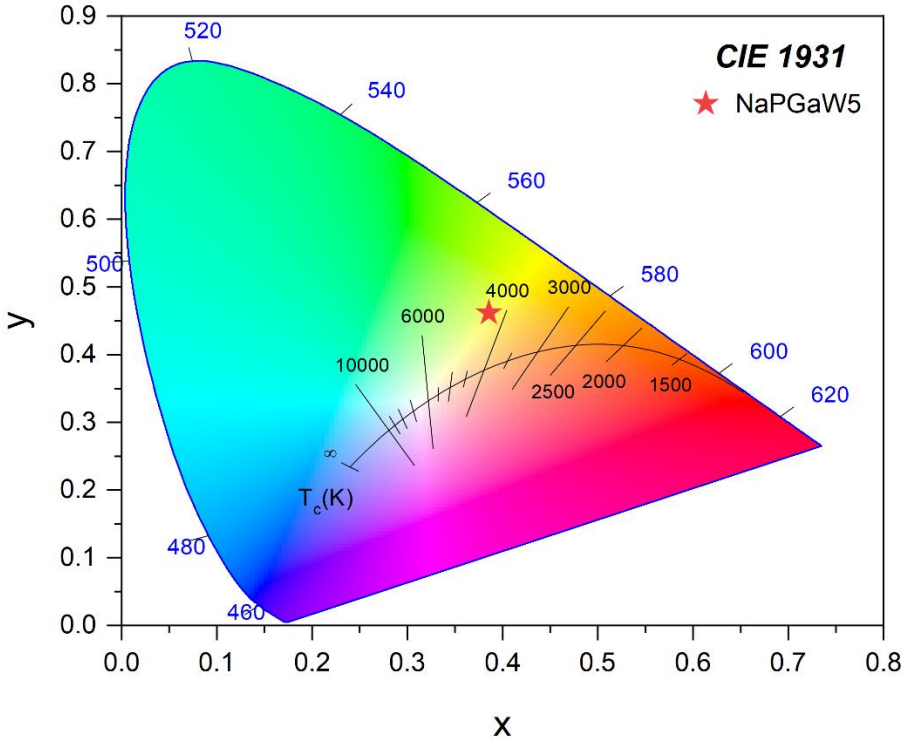

Motivated by an increasing number of applications of scintillators at low temperatures, like cryogenic experiments searching for rare events [21-23], we investigated the luminescence of NaPGaW glasses over a wide temperature range, as the luminescence resulting from STEs is a process that exhibits strong temperature dependence. Figure 8(a) shows the variation of the PL emission response of NaPGaW5 glass over the 80-300 K temperature range. At lower temperatures, the lack of thermal energy favors radiative recombination and higher emission intensities are expected. Figure 8(b) shows the integrated emission intensity as a function of the temperature for the NaPGaW5 glass. At 80 K, the integrated intensity is about 16x higher than at room temperature. In Fig. 8(c), it is possible to observe that a progressive inhomogeneous broadening of the band on the high energy side takes place for temperatures above 80 K indicating vibronic coupling [24].

Figure 8. (a) Temperature dependence of the emission of representative glass NaPGaW5 in the 300 – 80 K temperature range under 290 nm excitation. (b) Integrated area of the broad emission band of the NaPGaW5 glass as a function of temperature (80-300 K). (c) Normalized PL emission of the NaPGaW5 glass as a function of the temperature.

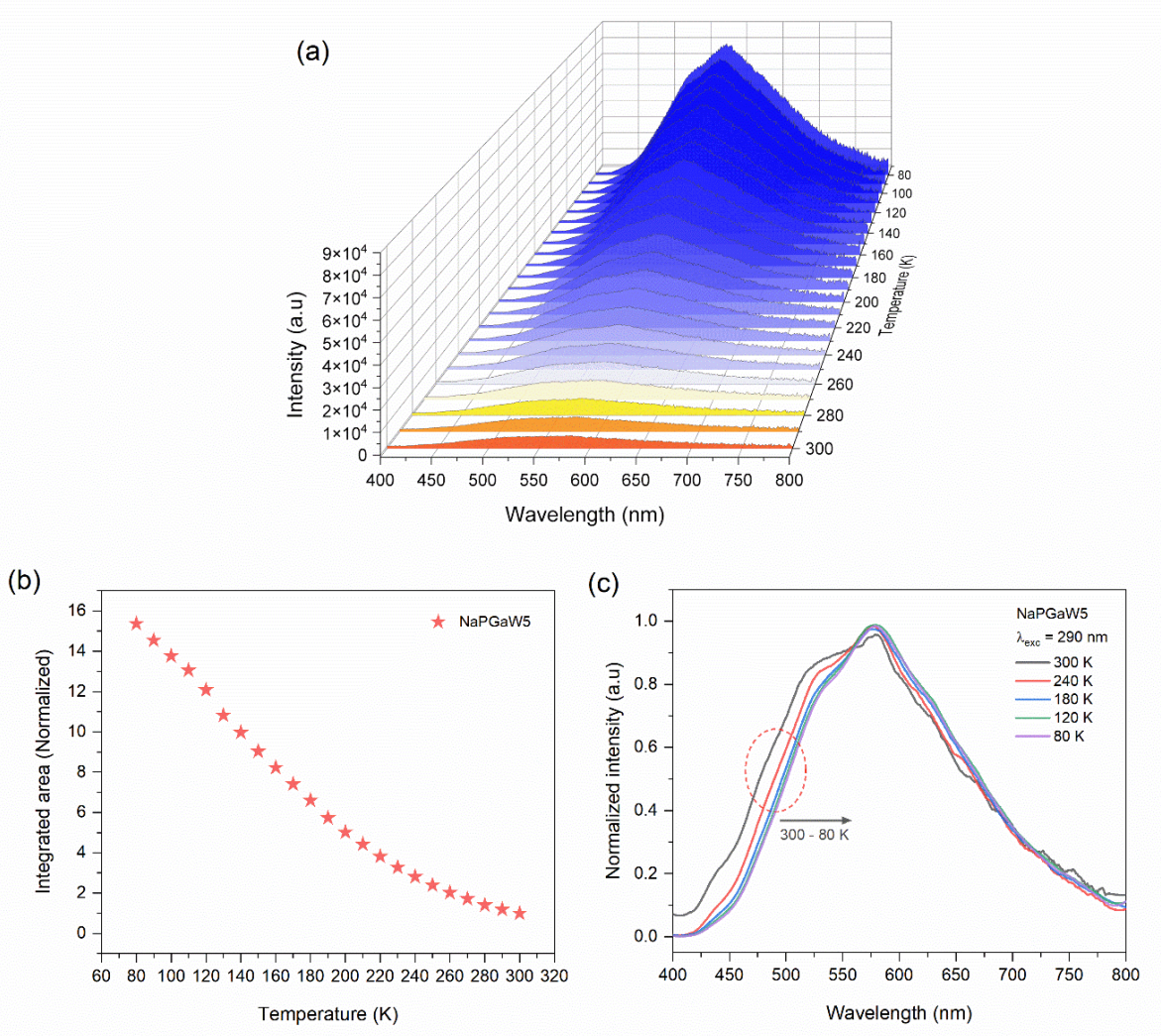

Luminescence decay lifetime. The luminescence decay curve of the NaPGaW5 glass measured at room temperature is shown in Figure S1 along with the curve of the pulsed laser decay (at 290 nm). Considering that the broad emission has contributions from more than one luminescence center, the lifetime decay curves were interpreted as a distribution of decay times. The decay curves were fitted with three exponentials and taking into account the different weights, with the resulting lifetime values ranging from 32 to 20 μs being considered as average values (Fig. 9). Overall, the average lifetime decreases for higher Na_2WO_4 contents, in agreement with previous reports in the literature for tungstate glasses and crystals [25,26].

Notably, a good compromise between emission intensity and a short lifetime is achieved by the NaPGaW5 glass.

Figure 9. Average lifetime values as a function of the Na_2WO_4 content. The dash-dotted line in the figure is a guide for the eyes.

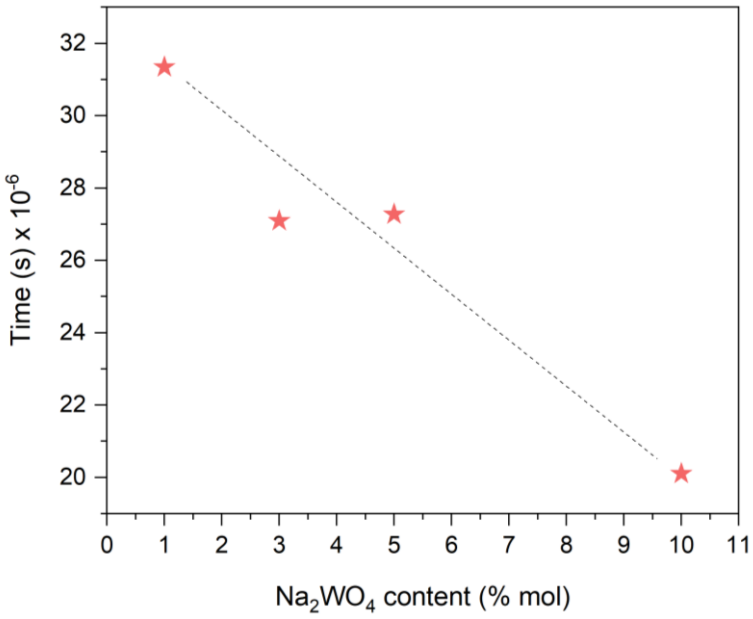

Radioluminescence. To evaluate the capability of NaPGaW glasses to detect X-rays, RL spectra of all samples were obtained at room temperature, as shown in Figure 10. A broad band centered at approximately 550 nm was observed, similar to the one observed upon UV excitation. As discussed in the UV case, the NaPGa glass did not present emission in this spectral region. Contrary to the case of the $PbWO_4$ scintillator, in which the emission mechanism arises from Pb^{2+} and $WO4^{2-}$ ions and energy transfer mechanisms between radiating centers lead to a fast decaying but low intensity scintillation at room temperature, in the case of the present glasses the emission originates from the radiative recombination of self-trapped excitons (STEs) localized at WO_4^{2-} ions [27,28]. The emission intensity increases with increasing concentration of tungsten oxide up to 5 mol% and then decreases for higher concentrations, as also observed for UV excitation. Whatever the excitation mechanism, UV or X-rays, the emission bands of the NaPGaW glasses match very well with the spectral sensitivity region of Si photodetectors and photomultipler tubes, being in the same spectral region of the emission of the well and long known scintillators $Bi_4Ge_3O_{12}$ (BGO) and $CdWO_4$ [28,29].

Figure 20. Radioluminescence spectra of the NaPGaW glasses under X-ray excitation.

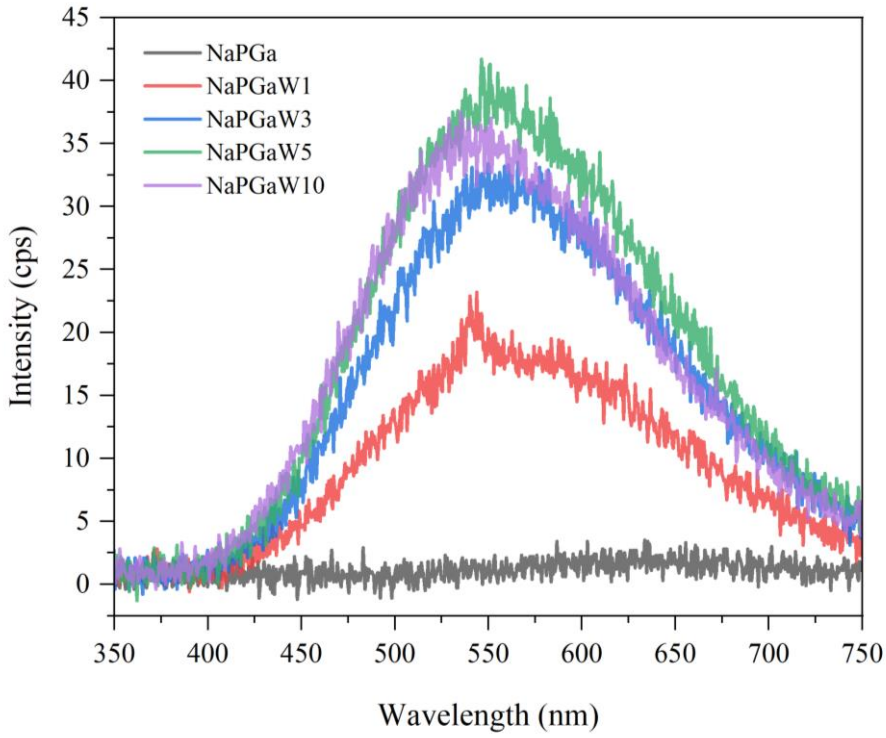

Although it is not the aim of this work to propose our glasses as promising substitutes for well established commercial scintillator crystals as BGO, a comparison of emission intensities of samples with very similar dimension and under the same experimental conditions (Fig. S2) indicates that the emission of the glasses are incomparably lower than the crystal, which is not surprising, given the different compositions and nature of the materials. Still, this result indicates that, given the previously mentioned cost and production constraints of crystal obtainment, there are many opportunities for the development of glass scintillators with, so far, very few reports in the literature. As to the new tungsten gallium-phosphate glasses, they might find use in specific applications not requiring high levels of intensity.

5.4 Conclusions

Tungsten gallium-phosphate glasses were successfully synthesized by the melt-quenching technique with high stability and excellent optical quality aiming at application in scintillating detectors. The synthesized glasses present high optical transparency (~ 90%) in the 300-2000 nm region enabling their use in a wide spectral region. XPS analysis indicate the sole or predominant presence of W^{6+}, in agreement with luminescence results suggesting WO_4^{2-}

complexes as the luminophore. The NaPGaW glasses present a broad visible emission under UV and X-ray excitation ascribed to the radiative decay of self-trapped excitons characteristic of the WO_4^{2-} complexes. When at cryogenic temperatures, the NaPGaW glasses showed enhanced luminescence. The average luminescence decay lifetime for the NaPGaW glasses is the order of 20-32 μs, compatible with applications demanding a fast response. In summary, the results suggest the NaPGaW glasses to have potential as a glass scintillator, including at cryogenic temperatures.

AUTHOR CONTRIBUTIONS

Thiago A. Lodi: Conceptualization, Methodology, Investigation, Data curation, Writing- Original draft preparation.: **Gustavo Galleani**: Conceptualization, Data curation, Investigation, Writing - Reviewing and Editing. **Leonnam G. Merízio**: Investigation, Data curation, Formal analysis, Writing - Original draft preparation. **Luiz G. Jacobsohn***:* Investigation, Data curation, Writing- Reviewing and Editing.**: Valmor R. Mastelaro:** Investigation, Writing- Reviewing and Editing, Supervision.: **Andrea S. S. de Camargo:** Conceptualization, Writing- Reviewing and Editing, Supervision, Funding.

ACKNOWLEDGEMENTS

Authors would like to acknowledge the Brazilian funding agencies CAPES - Coordenação de Aperfeiçoamento de Pessoal de Nível Superior, CNPq - Conselho Nacional de Desenvolvimento Científico e Tecnológico (Universal project 130562/2018-1) and FAPESP - Fundação de Amparo à Pesquisa do Estado de São Paulo (Process number 2013/07793-6, CEPID program). GG acknowledges funding by FAPESP, (grant number 2018/03931-9). LGM acknowledges funding by FAPES, (grant number 2019/21770-5). L.G. Jacobsohn's work was supported by the National Science Foundation under Grant No. 1653016.

REFERENCES

[1] P. Lecoq, A. Gektin, M. Korzhik, Inorganic Scintillators for Detector Systems, Second edi, Springer, Berlim, Germany, 2017.

[2] C.W.E. van E. Delft, Inorganic scintillators in medical imaging, Phys Med Biol. 85 (2002) R85–R106. https://doi.org/10.1016/S0168-9002(03)01542-0.

[3] S.N. Ahmed, Physics and Engineering of Radiation Detection, 2o Edition, 2015.

[4] A.M. Abdelghany, A.H. Hammad, The effect of WO_3 dopant on the structural and optical properties of ZnO-P_2O_5 glass and the effect of gamma irradiation, J Mol Struct. 1081 (2015) 342–347. https://doi.org/10.1016/j.molstruc.2014.10.055.

[5] J.D. Musgraves, J. Hu, L. Calvez, Handbook of Glass, 1a Edition, 2019.

[6] I.C. Pinto, G. Galleani, L.G. Jacobsohn, Y. Ledemi, Y. Messaddeq, A.S.S. de Camargo, Fluorophosphate glasses doped with Eu^{3+} and Dy^{3+} for X-ray radiography, J Alloys Compd. 863 (2021) 158382. https://doi.org/10.1016/j.jallcom.2020.158382.

[7] L.G. Merízio, T.A. Lodi, E. Bonturim, A.S.S. de Camargo, Persistent luminescent phosphor-in-glass composites based on $NaPO_3$ – Ga_2O_3 glasses loaded with $Sr2MgSi_2O_7$:Eu^{2+},Dy^{3+}, Opt Mater (Amst). 134 (2022) 113046. https://doi.org/10.1016/j.optmat.2022.113046.

[8] M.A. Ouis, M.A. Azooz, H.A. Elbatal, Optical and infrared spectral investigations of cadmium zinc phosphate glasses doped with WO_3 or MoO_3 before and after subjecting to gamma irradiation, J Non Cryst Solids. 494 (2018) 31–39. https://doi.org/10.1016/j.jnoncrysol.2018.04.053.

[9] M. Lu, F. Wang, Q. Liao, K. Chen, J. Qin, S. Pan, FTIR spectra and thermal properties of TiO_2-doped iron phosphate glasses, J Mol Struct. 1081 (2015) 187–192. https://doi.org/10.1016/j.molstruc.2014.10.029.

[10] E. El-Meliegy, M.M. Farag, J.C. Knowles, Dissolution and drug release profiles of phosphate glasses doped with high valency oxides, J Mater Sci Mater Med. 27 (2016) 1–10. https://doi.org/10.1007/s10856-016-5711-8.

[11] K. Girija, S. Thirumalairajan, V.R. Mastelaro, D. Mangalaraj, Photocatalytic degradation of organic pollutants by shape selective synthesis of β-Ga_2O_3 microspheres constituted by nanospheres for environmental remediation, J Mater Chem A Mater. 3 (2015) 2617–2627. https://doi.org/10.1039/c4ta05295a.

[12] Z. Wang, D. Kong, M. Wang, G. Wang, N. Li, D. Li, Sealing effect of surface porosity of Ti-P composite films on tinplates, RSC Adv. 9 (2019) 12990–12997. https://doi.org/10.1039/c8ra10523e.

[13] D. Manzani, R.G. Fernandes, Y. Messaddeq, S.J.L. Ribeiro, F.C. Cassanjes, G. Poirier, Thermal, structural and optical properties of new tungsten lead-pyrophosphate glasses, Opt Mater (Amst). 33 (2011) 1862–1866. https://doi.org/10.1016/j.optmat.2011.02.041.

[14] V. Kumar, Z. Luo, A review on x-ray excited emission decay dynamics in inorganic scintillator materials, Photonics. 8 (2021) 1–27. https://doi.org/10.3390/photonics8030071.

[15] Z. Lou, M. Cocivera, Cathodoluminescence of $CaWO_4$ and $SrWO_4$ thin films prepared by spray pyrolysis, Mater Res Bull. 37 (2002) 1573–1582. https://doi.org/10.1016/S0025-5408(02)00851-6.

[16] V. Yakovyna, Y. Zhydachevskii', V.B. Mikhailik, I. Solskii, D. Sugak, M. Vakiv, Effect of thermo-chemical treatments on the luminescence and scintillation properties of $CaWO_4$, Opt Mater (Amst). 30 (2008) 1630–1634. https://doi.org/10.1016/j.optmat.2007.11.003.

[17] V.B. Mikhailik, H. Kraus, G. Miller, M.S. Mykhaylyk, D. Wahl, Luminescence of $CaWO_4$, $CaMoO_4$, and $ZnWO_4$ scintillating crystals under different excitations, J Appl Phys. 97 (2005). https://doi.org/10.1063/1.1872198.

[18] N. Ahmed, H. Kraus, H.J. Kim, V. Mokina, V. Tsiumra, A. Wagner, Y. Zhydachevskyy, V.B. Mykhaylyk, Characterisation of tungstate and molybdate crystals ABO_4 (A = Ca, Sr, Zn, Cd; B = W, Mo) for luminescence lifetime cryothermometry, Materialia (Oxf). 4 (2018) 287–296. https://doi.org/10.1016/j.mtla.2018.09.039.

[19] G. Poirier, Y. Messaddeq, S.J.L. Ribeiro, M. Poulain, Structural study of tungstate fluorophosphate glasses by Raman and X-ray absorption spectroscopy, J Solid State Chem. 178 (2005) 1533–1538. https://doi.org/10.1016/j.jssc.2004.10.032.

[20] A.B. Campos, A.Z. Simões, E. Longo, J.A. Varela, V.M. Longo, A.T. de Figueiredo, F.S. de Vicente, A.C. Hernandes, Mechanisms behind blue, green, and red photoluminescence emissions in CaWO4 and CaMoO4 powders, Appl Phys Lett. 91 (2007) 1–4. https://doi.org/10.1063/1.2766856.

[21] V.B. Mikhailik, S. Galkin, H. Kraus, V. Mokina, A. Hrytsak, V. Kapustianyk, M. Panasiuk, M. Rudko, V. Rudyk, ZnTe cryogenic scintillator, J Lumin. 188 (2017) 600–603. https://doi.org/10.1016/j.jlumin.2017.05.021.

[22] D. Poda, Scintillation in Low-Temperature Particle Detectors, Physics (Switzerland). 3 (2021) 473–535. https://doi.org/10.3390/physics3030032.

[23] H. Kraus, V.B. Mikhailik, Y. Ramachers, D. Day, K.B. Hutton, J. Telfer, Feasibility study of a $ZnWO_4$ scintillator for exploiting materials signature in cryogenic WIMP dark matter searches, Physics Letters, Section B: Nuclear, Elementary Particle and High-Energy Physics. 610 (2005) 37–44. https://doi.org/10.1016/j.physletb.2005.01.095.

[24] M. Fox, Optical Properties of Solids, Second Edi, Oxford University Press, 2010.

[25] H. Kraus, V.B. Mikhailik, D. Wahl, Multiple photon counting coincidence (MPCC) technique for scintillator characterisation and its application to studies of $CaWO_4$ and $ZnWO_4$ scintillators, Nucl Instrum Methods Phys Res A. 553 (2005) 522–534. https://doi.org/10.1016/j.nima.2005.07.011.

[26] T. Scheike, H. Segawa, S. Inoue, Y. Wada, Blue luminescence in the WO_3-P_2O_5-ZnO glass system, Opt Mater (Amst). 34 (2012) 1488–1492. https://doi.org/10.1016/j.optmat.2012.03.014.

[27] P. Lecoq, I. Dafinei, E. Auffray, M. Schneegans, M. v. Korzhik, O. v. Missevitch, V.B. Pavlenko, A.A. Fedorov, A.N. Annenkov, V.L. Kostylev, V.D. Ligun, Lead tungstate ($PbWO_4$)

scintillators for LHC EM calorimetry, Nuclear Inst. and Methods in Physics Research, A. 365 (1995) 291–298. https://doi.org/10.1016/0168-9002(95)00589-7.

[28] J.H. Ryu, J.W. Yoon, K.B. Shim, Blue luminescence of nanocrystalline $PbWO_4$ phosphor synthesized via a citrate complex route assisted by microwave irradiation, Solid State Commun. 133 (2005) 657–661. https://doi.org/10.1016/j.ssc.2004.12.046.

[29] T. Yanagida, Study of rare-earth-doped scintillators, Opt Mater (Amst). 35 (2013) 1987–1992. https://doi.org/10.1016/j.optmat.2012.11.002.

6 PROMISING Tb^{3+}-DOPED GALLIUM TUNGSTEN-PHOSPHATE GLASS SCINTILLATOR: SPECTROSCOPY, ENERGY TRANSFER AND UV/X-RAY SENSING

Thiago A. Lodi [a,*], Jéssica F. M. dos Santos [a,*], Gustavo Galleani [a], Luis G. Jacobsohn [b], Tomaz Catunda [a], Andrea S.S de Camargo [a,*]

[a] São Carlos Institute of Physics, University of São Paulo, Av. Trabalhador Saocarlense 400, São Carlos, SP, 13566-590, Brazil.

[b] Department of Materials Science and Engineering, Clemson University, 515 Calhoun Dr, Clemson, SC, 29634, United States of America.

DOI: *10.1016/j.jallcom.2022.164016*

ABSTRACT

In view of their promising application as UV and X-ray scintillators, undoped and Tb^{3+}-doped (0.5 – 10 mol%) gallium tungsten-phosphate glasses, in the new compositional system $NaPO_3$-Ga_2O_3-Na_2WO_4, have been prepared and characterized by UV-vis absorption, photoluminescence excitation and emission, and excited state decay measurements. A detailed study of ion-ion energy transfer, based on the analysis of decay curves by the Inokuti-Hirayama model, indicated that the energy transfer process affecting the emitting level $^5D_3$ of Tb^{3+} is related to dipole–dipole interaction. Additionally, a theoretical model was successfully employed to establish a correlation between the emission color variation due to changes in the green to blue emission ratio (I_G/I_B). The emission spectra of the undoped and Tb^{3+}-doped glasses were measured under UV and X-ray excitation. From the viewpoint of UV-sensing, samples doped with up to 7.0 mol% Tb^{3+} do not present visible emission quenching, whereas X-ray sensing is not prone to quenching at all. These characteristics, associated to the high density, chemical and mechanical stability of the glasses evidence their promising use in scintillating devices.

6.1 Introduction

A scintillator functions as a wavelength shifter. It converts the energy of a charged particle (α and β, for example) or high energy photons, such as UV, X-rays and γ-ray, into several low energy photons in the visible or near-visible range of the electromagnetic spectrum. These photons, in turn, can be easily detected by photodetectors such as photodiodes (PD) and photomultiplier tubes (PMTs) [1], enabling scintillators for diverse applications such as in industrial and medical imaging, homeland security and high energy experiments [2,3]. The luminescence centers in scintillators can be intrinsic or extrinsic in nature. Intrinsic luminescence mainly involves ions or chemical groups composing the scintillator. Extrinsic luminescence, on the other hand, originates from metallic dopant ions, commonly involving the f-f and f-d transitions of Tb^{3+}, Eu^{2+} and Ce^{3+} [1,4,5]. Typically, scintillators are made from inorganic single crystals with high emission efficiency and energy resolution, such as $LaBr_3$:Ce and BGO that are commercially available scintillators [6]. However, the growth of single-crystals is time-consuming, expensive, and results in materials with limited sizes and shapes. For this reason, increasing interest has been demonstrated for glass scintillators, which can provide cost-effective, large-scale production, being easily processed into complex geometries such as optical fibers [7].

Despite the fact that many compositions have been explored for optical applications, phosphate glasses remain, perhaps, the most interesting materials on account of their top-notch physical properties such as high thermal expansion coefficient and easy processing due to the low melting temperature (compared to silicate glasses) [8-11]. Besides, phosphate glasses allow higher rare earth (RE) ions solubility than other oxide glassy matrices such as silicates and borates, i.e., the RE luminescence quenching phenomenon usually occurs at very high (> 5 mol%) RE doping concentration. However, these glasses have relatively poor chemical stability, which often limits their applications. In this context, considerable work has been carried out on improving the physical-chemical properties of phosphate glasses by introducing several glass formers and modifiers such as CaO, MoO_3, Ga_2O_3, WO_3, Ta_2O_3, Sb_2O_3, etc., [12-15]. Through the proper choice of these metal oxides, the structural network of phosphate - based glasses can be modified to increase their chemical, thermal and mechanical stability, their luminescence characteristics, biocompatibility, etc. The new glass system investigated in this work is based on the composition $NaPO_3$-Ga_2O_3-Na_2WO_4 (NaPGaW). The addition of both Na_2WO_4 [14,16] and Ga_2O_3 [17,18] modifiers is known to enhance mechanical, and thermal

stabilities, chemical durability of phosphate glasses and makes this glass system interesting for optical applications. Moreover, the incorporation of tungsten is responsible for increasing the glass density and possibly for decreasing the phonon energy of the phosphate network. The increase of the glass density can also enhance the probability of interaction of the ionizing radiation with matter, an essential feature for scintillators [19].

Among the RE ions that present 4f-4f transitions, known to have strong emission in the UV-Vis-IR region, Tb^{3+} is one of the most interesting dopants with potential for application in solid state lasers, scintillators, biological detectors, white light generators, field emission and other fluorescent devices [20-22]. The characteristic emissions of this ion originating from the metastable levels $^5D_3$ (379-456 nm) and $^5D_4$ (487-620 nm), are susceptible to the presence of energy transfer (ET) mainly through the cross-relaxation mechanism (W_{43}^{CR}, in Fig. 1). In this process, electronic population is transferred from the level $^5D_3$ to $^5D_4$ [21-23], imposing a quenching to the emission from the donor level $^5D_3$ and favoring the emission from $^5D_4$.

Typical host media (insulators or wide bandgap semiconductors) exert limited influence on the RE transitions due to the effective screening of 4f electrons by the outer shell orbitals 5p, 5d and 6s. Since the first that terbium-activated glass was reported [24], numerous glass compositions have been proposed, such as barium silicate [25], tungsten gadolinium borate [26] and borogermanate glasses [27]. However, to the best of our knowledge, Tb^{3+}-doped gallium tungsten-phosphate glass scintillators have not been investigated. The high Tb concentration limit prior to quenching, associated to long radiative lifetime values (ms) and the green emission which matches commercial photodetectors, such as charge coupled device (CCD) and silicon PMT, allow detection of high-energy excitation radiation [28].

In this work, we present detailed spectroscopic investigation of these novel NaPGaW glasses with special emphasis on energy transfer studies of the Tb^{3+} doped samples. Because the excited states $^5D_3$ and $^5D_4$ are connected via a cross relaxation mechanism, whose efficiency depends on Tb^{3+} concentration, a thorough characterization is important to determine the optimum range of dopant concentration for the intended application as a scintillator glass. The fluorescence decay curves, which carry the excited state dynamics information, were fit by the Inokuti-Hirayama (IH) model, and the color of the samples, associated to the ratio of green to blue emission intensity ratio I_G/I_B was modeled and correlated to the quantum efficiencies. Last but not least, the characterization of the doped glasses intense emission spectra upon UV and X-ray excitation is presented, which, associated to the excellent mechanical and chemical stability, and high density of the glasses indicates their promising use as scintillators.

Figure 1. Partial energy level diagram of Tb^{3+} illustrating the pump power rate (R_{14}), radiative decay rates (A_{31}, A_{32}, A_{41}, A_{42}, A_{43}), the cross-relaxation process (W_{43}^{CR}) and W_{43}^{*} which corresponds to the sum of all independent decay rates from $^5D_3$.

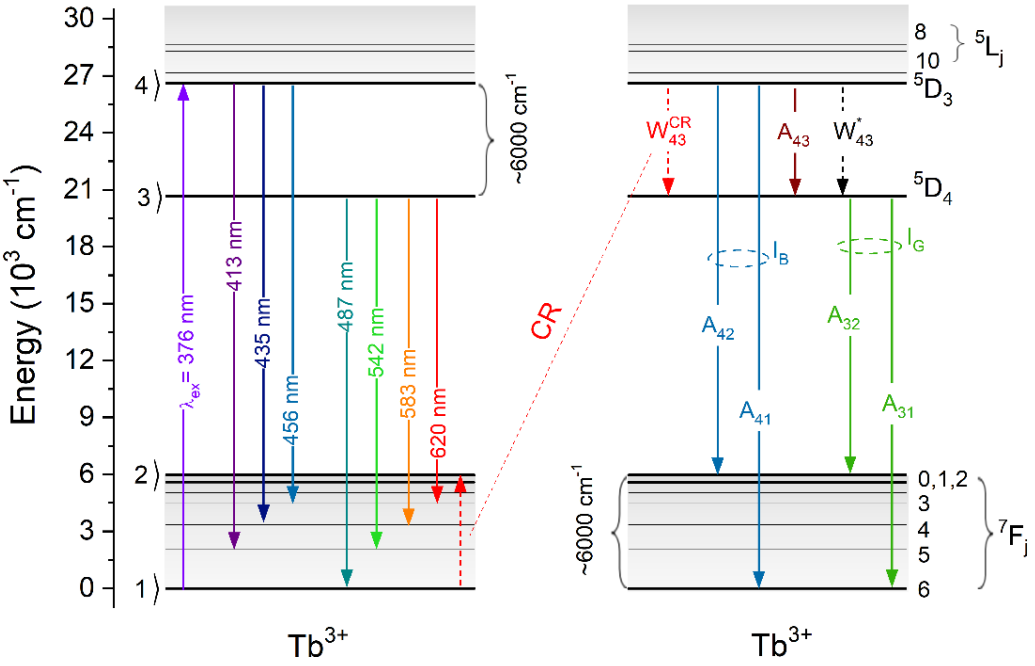

6.2 Experimental procedure

Undoped and Tb^{3+} doped gallium tungsten-phosphate glasses with composition $60NaPO_3$–$(20-x)Ga_2O_3$–$20Na_2WO_4.2H_2O$–$xTbCl_3.6H_2O$ (x = 0, 0.5, 1, 3, 5, 7 and 10 mol%) were obtained by the melt-quenching technique. Stoichiometric batches of the solid starting materials (≥ 99,9% purity) were mixed in an agate mortar and melted in a platinum crucible, in an electric furnace at 1000-1100ºC, for 1h, in air atmosphere. Immediately after the quenching, the melt was poured into a preheated stainless-steel mold at 280 ºC. In order to minimize the internal mechanical stress, the glasses were annealed at 300 °C for 4 h and then slowly cooled to ambient temperature. Finally, the glasses were cut and optically polished with 2 mm thickness. The nominal compositions and respective sample labeling are given in Table 1 along with the values of volumetric density (ρ) which were calculated according to the Archimedes principle, using distilled water as an immersion liquid, at room temperature.

The UV–Vis-NIR ground state absorption spectra of the samples were recorded using a Perkin-Elmer Lambda 1050 double-beam spectrometer in the range 250-800 nm with a spectral resolution of 1 nm. The photoluminescence (PL) excitation and emission spectra of the undoped and Tb^{3+}-doped glasses were recorded in a HORIBA Jobin Yvon spectrofluorimeter model

Fluorolog-3, equipped with 450 W CW Xenon arc lamp as an excitation source. The excited state lifetime values were measured in the same spectrofluorimeter, using a pulsed Xe lamp. Radioluminescence (RL) measurements were recorded in a Freiberg Instruments Lexsyg Research spectrofluorometer equipped with a Varian Medical Systems VF-50J X-ray tube with a tungsten target. These measurements were performed in collaboration with the Jacobsohn research group at the University of Clemson, in the USA.

Table 1. Glass label, nominal composition (mol%) and volumetric density (ρ).

Glass label	Nominal composition (mol%)				ρ (g/cm^3)
	$NaPO_3$	Ga_2O_3	Na_2WO_4	$TbCl_3$	
NaPGa	80	20	-	-	3.04
NaPGaW20	60	20	20	0	3.62
NaPGaW0.5Tb	60	19.5	20	0.5	3.63
NaPGaW1Tb	60	19	20	1	3.63
NaPGaW3Tb	60	17	20	3	3.60
NaPGaW5Tb	60	15	20	5	3.72
NaPGaW7Tb	60	13	20	7	3.70
NaPGaW10Tb	60	10	20	10	3.82

6.3 Results and discussion

All the glass samples were obtained colorless and transparent with good chemical stability under the ambient atmosphere. Photographs of the undoped NaPGaW and NaPGaW:Tb^{3+} samples under ambient light and UV lamp excitation are shown in Figure 2.

Figure 2. Photographs of the undoped glass under (a) ambient light, and (b) UV excitation (326 nm). (c) Photographs of the Tb^{3+} doped glasses under UV lamp excitation (376 nm), in ascending order of Tb-concentration (0.5, 1.0, 3.0, 5.0, 7.0 and 10.0 mol%) from left to right.

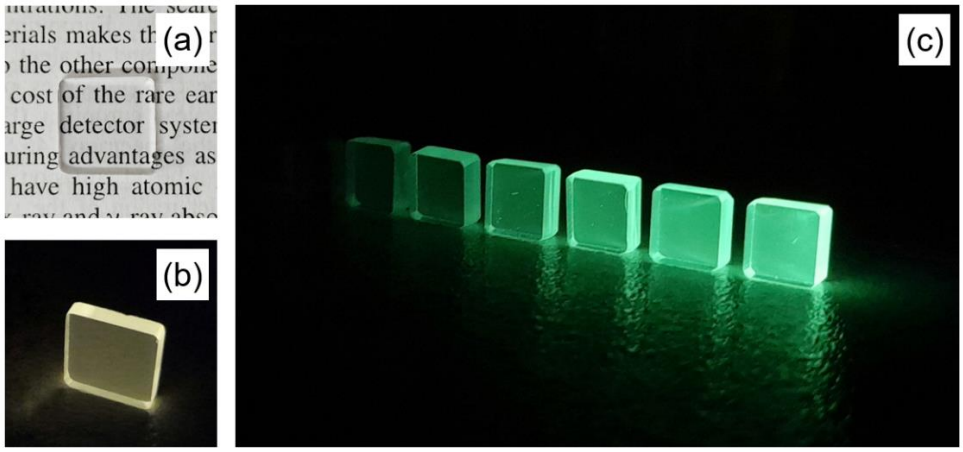

Undoped glasses

According to Table 1, the undoped NaGaW20 glass presented higher density than the analogue glass NaPGa without sodium tungstate. This result is expected due to the higher molar density of $Na_2WO_4.2H_2O$ ($\rho \sim 4.18$ g.cm^{-3}) when compared to that of $NaPO_3$ ($\rho \sim 2.48$ g.cm^{-3}). The volumetric density of the NaPGaW20 glass is similar to commercially available inorganic single crystal scintillator NaI:Tl (3.67g/cm^3) [29] and superior to the ^{6}Li-glass scintillator (Ce^{3+}-doped ^{6}Li silicate, GS20®) (2.5 g/cm^3) [30].

Figure 3 presents the absorption spectra of the NaPGa and NaPGaW20 samples, recorded in the wavelength range 250-800 nm. A wide transmittance window indicates that both glasses are suitable for several rare earth doping. It can also be seen that when adding Na_2WO_4, the absorption edge of the NaPGaW20 glass in the UV shifts towards longer wavelengths (redshift) when compared to the NaPGa glass. This behavior can be explained by the increase of the covalent character of the vitreous network, attributed to the insertion of WO_n polyhedral, which link PO_4 forming a highly covalent three-dimensional network [31,32].

It is well known that tungsten cations present four oxidation states, W^{3+} to W^{6+}, and the amount of each state is dependent on the composition and melting conditions of the glass. The strong UV absorption band around 350 nm due to the charge transfer of hexavalent tungsten state (W^{6+}), and the absence of an absorption band at ~780 nm, as well as of blueish color in the glasses, indicates the existence of mainly hexavalent tungsten in the studied glasses [16].

Figure 3. Ground state absorption spectra of NaPGa and NaPGaW20 glasses in the UV-Vis region.

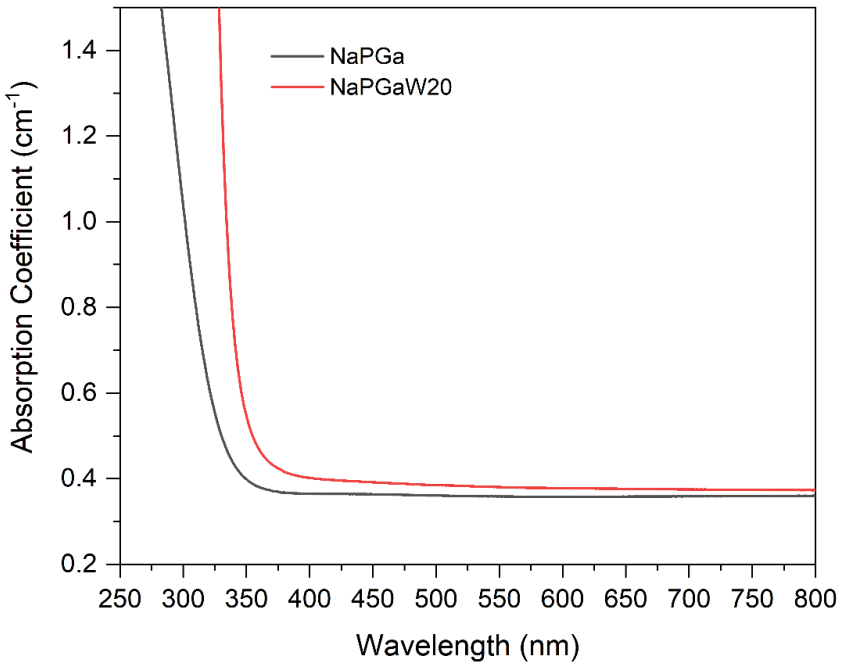

Figure 4 shows the PL excitation and emission spectra of the NaPGaW20 glass and the PL emission spectra of the NaPGa glass for comparison. In the case of NaPGaW20, a wide emission band centered at approximately 570 nm, corresponding to the yellow emission seen in Fig. 2(b), can be observed. Scheike et al. [33] reported an emission centered at λ = 530 nm in WO_3-P_2O_5-ZnO glass. Wen et al.[34], observed a similar emission band centered at 465 and 496 nm in the tungsten-doped glasses $(Na_2WO_4.2H_2O)_{0.01}(PbO)_{49.99}(B_2O_3)_{50}$ and $(Na_2WO_4.2H_2O)_{0.5}(PbO)_{49.5}(B_2O_3)_{50}$, upon excitation at 332 and 343 nm, respectively. The $(WO_3)_{0.5}(SiO_2)_{49.5}(Na_2O)_{25}(B_2O_3)_{25}$ glass showed a broader and stronger emission band at 520 nm under excitation at 300 nm[34]. In crystals, such as $ZnWO_4$, $CdWO_4$ and $MgWO_4$, the broad band at approximately 540 nm is ascribed to the radiative decay of self-trapped excitons (STEs) at the (WO_4^{2-}) complex[35]. Based on these observations, the emission at about 570 nm was ascribed to the (WO_4^{2-}) ion.

In the last years, attempts were made to explain the STE radiative decay such as the model proposed by Korzhik et al.[36] and the model proposed by Leonelli and Brebner[37]. While differing in many aspects, one point is consensus: Luminescence seems to be associated with defects promoted by distortions in the structure.

Recently, a new model known as broadband model was proposed. This model assumes that there are energetically distributed states related to point defects such as oxygen vacancies. These states, located above the valence band and below the conduction band, can promote the

captured electrons to the conduction band by photons absorption, creating small polarons. This polarons interact with holes trapped in the crystal defects or impurities forming STEs that are responsible for the emission in the visible range[38,39].

The excitation spectrum of the NaPGaW20 glass monitored at 576 nm shows a broad excitation band peaked around 326 nm. In $ZnWO_4$ crystals[40] and other forms[41], this excitation band is assigned to charge-transfer transitions from the oxygen (O^{2-}) to the tungsten (W^{6+}) ions in the WO_6 molecular complexes.

Figure 4. Photoluminescence excitation and emission spectra of NaPGa (black spectrum) and NaPGaW20 (red spectra) glasses.

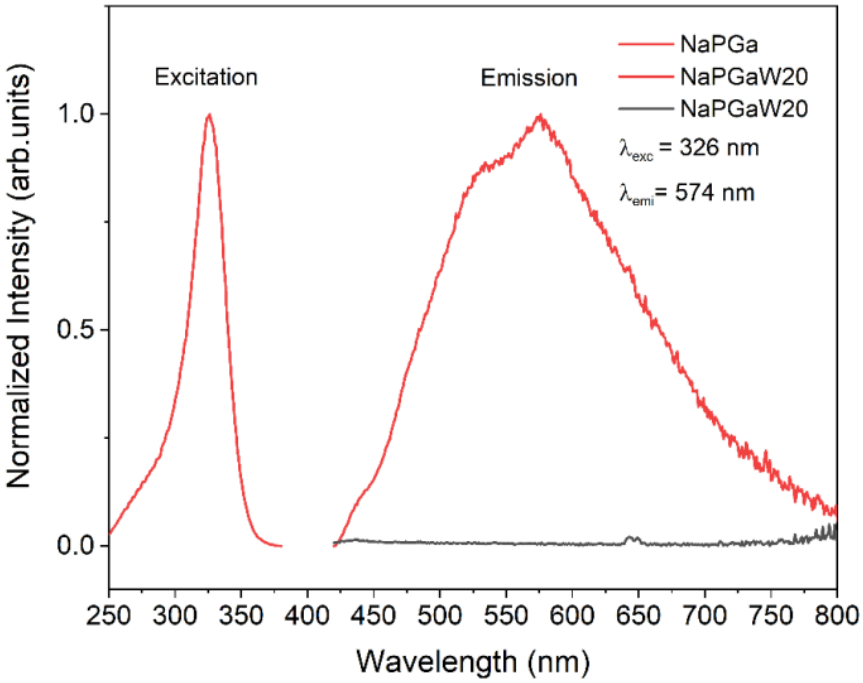

Besides UV excitation, the emission spectra of the undoped gallium tungsten-phosphate glasses were also investigated under X-ray excitation. The room temperature RL spectra shown as Figure 5 presents a broadband emission band centered at 540 nm, very similar to the band observed upon UV excitation, and which was attributed to the radiative decay of STEs at WO_6^{6-} complexes. Also, similar to the case of UV excitation, the NaPGa glass did not present any luminescence in the investigated range. It is worth noticing that this broad emission band observed under both, UV and X-ray excitation, overlaps quite well with the absorption range of CCD detectors and silicon photomultipliers [29], allowing for the use of these glasses as optical sensors.

Figure 5. Radioluminescence spectra of NaPGa and NaPGaW20 glasses under X-ray excitation.

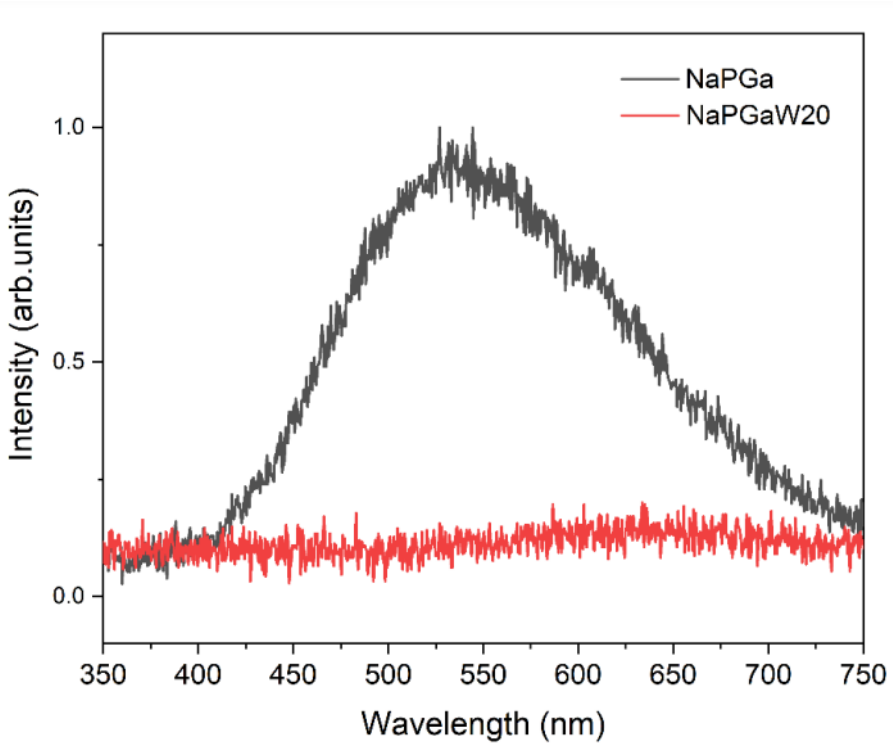

Tb^{3+} doped samples

As it can be seen in Table 1, the volumetric density values of doped glasses increase with the increasing substitution of Ga_2O_3 by $TbCl_3.6H_2O$. As well as in the NaPGaW20 glass, the volumetric density of the Tb^{3+} gallium tungsten-phosphate glasses is similar to that of the commercially available inorganic single crystal scintillator NaI:Tl (3.67g/cm^{3+}) [29], and superior to Tb silicate glass (3.03 g/cm^3) [42] and ^{6}Li-glass scintillator (Ce^{3+}-doped ^{6}Li silicate, GS20®) (2.5 g/cm^3) [30].

Figure 1 shows the partial energy level diagram of Tb^{3+} in the energy scale up to 30 × 10^3 cm^{-1} above the ground state multiplet $^7F_6$ of the $4f^8$ configuration. Selected radiative transitions are indicated by continuous lines whereas non-radiative relaxation processes are indicated by dashed and curved lines. The rich energy level diagram favors detrimental intra- and interionic energy transfer processes. In particular, the resonant CR efficiently quenches the $^5D_3$-fluorescence at high doping levels [59–61], as it will be discussed throughout this section.

UV-Vis-NIR absorption spectra of the NaPGaW:Tb^{3+} glasses are shown in Figure 6. In the UV-Vis region, four absorption bands at 351 nm, 368 nm, 377 nm and 485 nm are assigned to the optical transitions of Tb^{3+} ($^7F_6 \rightarrow {}^5L_9$, $^5L_{10}$, $^5D_3$ and $^5D_4$), respectively. The broad UV-

absorption band overlapped in the range 320 - 400 nm is associated with tungsten absorption. In the NIR region (inset), two absorption bands can be observed centered around 1900 nm and 2218 nm, assigned to the transitions $^7F_6 \rightarrow {}^7F_{0,1,2,3}$, as indicated. Furthermore, it was found that all the absorption bands intensities increased with increasing $TbCl_3$ concentration.

Figure 6. Absorption spectra of NaPGaW:Tb^{3+} glasses in the UV-vis and IR region (inset).

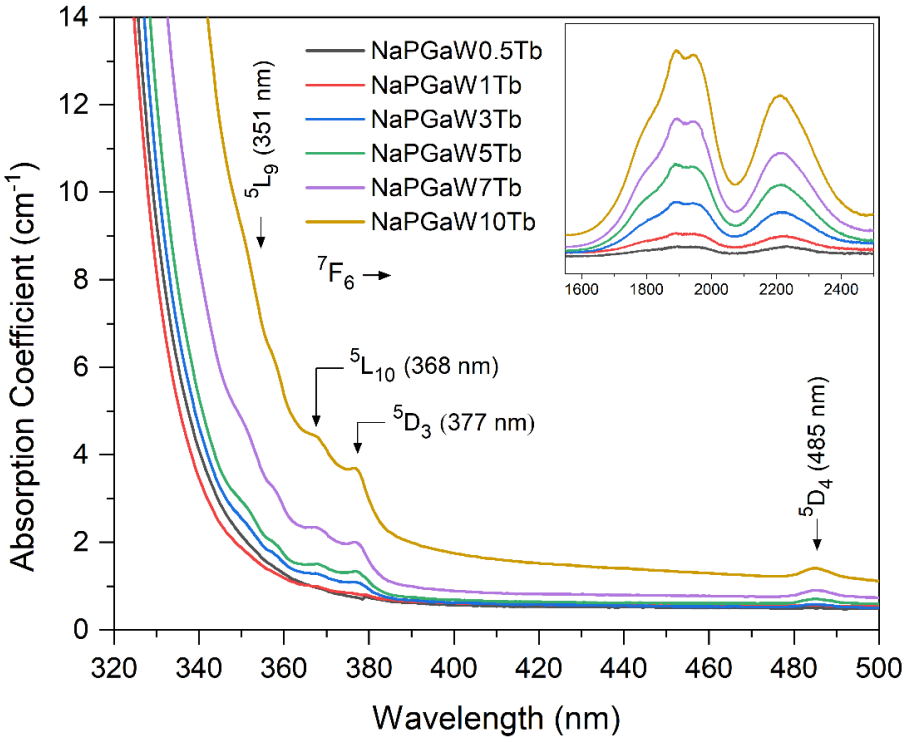

Fig. 7(a) shows the excitation spectrum of the NaPGaW:5.0Tb glass measured by monitoring the green emission of Tb^{3+} ions at 542 nm. The excitation spectrum (black line) can be divided in two regions. One is a broadband predominant at wavelengths lower than 330 nm attributed to tungsten transitions. The other is composed of several peaks at 302, 316, 338, 350, 357, 367, 376 and 484 nm which correspond to the excitation transitions from the ground state ($^7F_6$) of Tb^{3+} to the excited states $^5H_6$, $^5H_7$, $^5L_7$, ($^5G_4$ + $^5L_9$), $^5G_5$, $^5L_{10}$, $^5D_3$ and $^5D_4$, respectively. The other Tb^{3+}-doped NaPGaW glasses showed identical excitation peaks position as the NaPGaW:5Tb glass sample. The linear dependence of the integrated area of $^7F_6 \rightarrow {}^5D_3$ (blue) and $^7F_6 \rightarrow {}^5D_4$ (green) absorption bands on the dopant concentration is shown in Fig. 7(b) and (c), respectively. The $^5D_3$ and $^5D_4$ levels are particularly important, since they are the only metastable levels of Tb^{3+} in the visible range.

Figure 7. (a) Excitation spectrum of NaPGaW:5.0Tb glass, λ_{em} = 542 nm. (b)-(c) The dependence of the Tb^{3+} concentration on $^5D_3$ and $^5D_4$ absorption bands (integrated area).

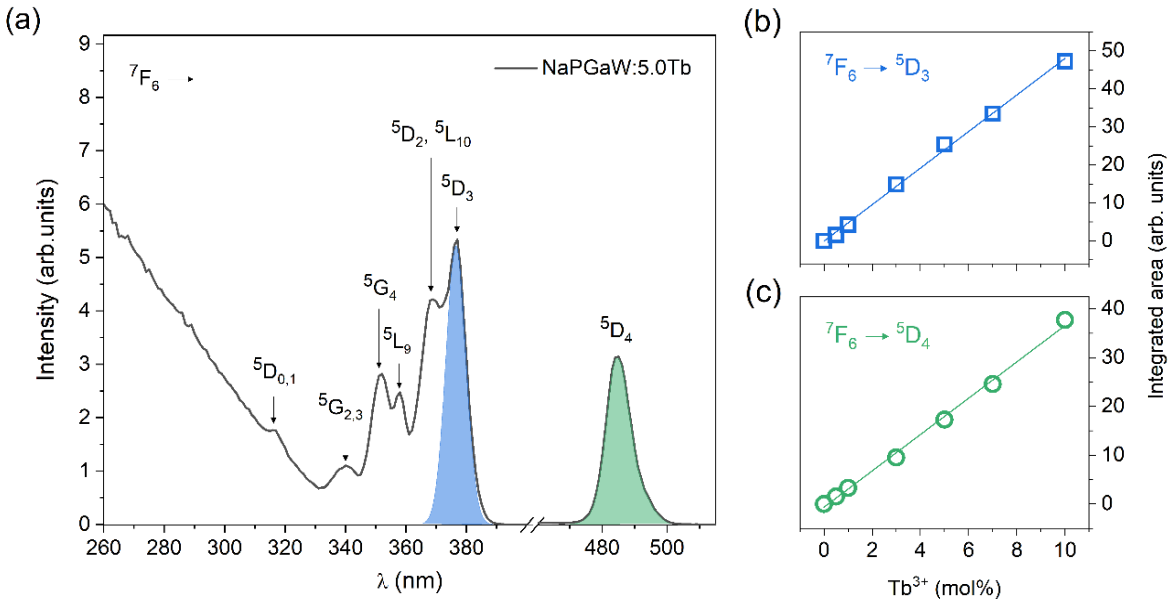

The emission spectra of the NaPGaW:Tb^{3+} glasses were measured with excitation at 376 nm ($^7F_6 \rightarrow {}^5D_3$ transition, Fig. 1) and are shown in Fig. 8. In order to highlight the ET process and the luminescence behavior, each spectrum in Fig. 8 was normalized to the intensity of its highest peak ($^5D_4 \rightarrow {}^7F_5$). The peaks in the blue spectral region, IB, (413, 435, 456 nm) are assigned to the $^5D_3 \rightarrow {}^7F_J$ (J = 5, 4, 3) transitions. The peaks in the green-red region, IG, (487, 542, 583 and 620 nm) are assigned to $^5D_4 \rightarrow {}^7F_J$ (J = 6, 5, 4, 3) transitions. Among these transitions, the magnetic dipole one, corresponding to the green emission $^5D_4 \rightarrow {}^7F_5$ at 542 nm, is the most intense one, satisfying the selection rule $\Delta J = \pm 1$. All the emissions involving the $^5D_3$ state are markedly affected by the Tb^{3+} ion concentration. The blue to green color change of the fluorescence (see inset in Fig. 8) of the fluorescence is mainly due to the following CR mechanism [45–47]:

$$^5D_3 + {}^7F_0 \rightarrow {}^5D_4 + {}^7F_6, \quad (1)$$

since the energy gaps between $^5D_3$ - $^5D_4$ and $^7F_6$ - $^7F_0$ are remarkably similar (Fig. 1).

Figure 8. Concentration dependence of the $^5D_3 \rightarrow {}^7F_J$ = 5-3 (blue) and $^5D_4 \rightarrow {}^7F_J$ = 6-3 (green) emission spectra under UV excitation (λ_{exc}= 376 nm) of Tb^{3+}- doped NaPGaW glass. All spectra were normalized by the peak of the $^5D_4 \rightarrow {}^7F_5$ transition (542 nm). Inset: $^5D_3 \rightarrow {}^7F_j$ = 3-5 (blue circle) and $^5D_4 \rightarrow {}^7F_j$ = 3-6 (green square) non-normalized integrated area as a function of Tb^{3+} concentration.

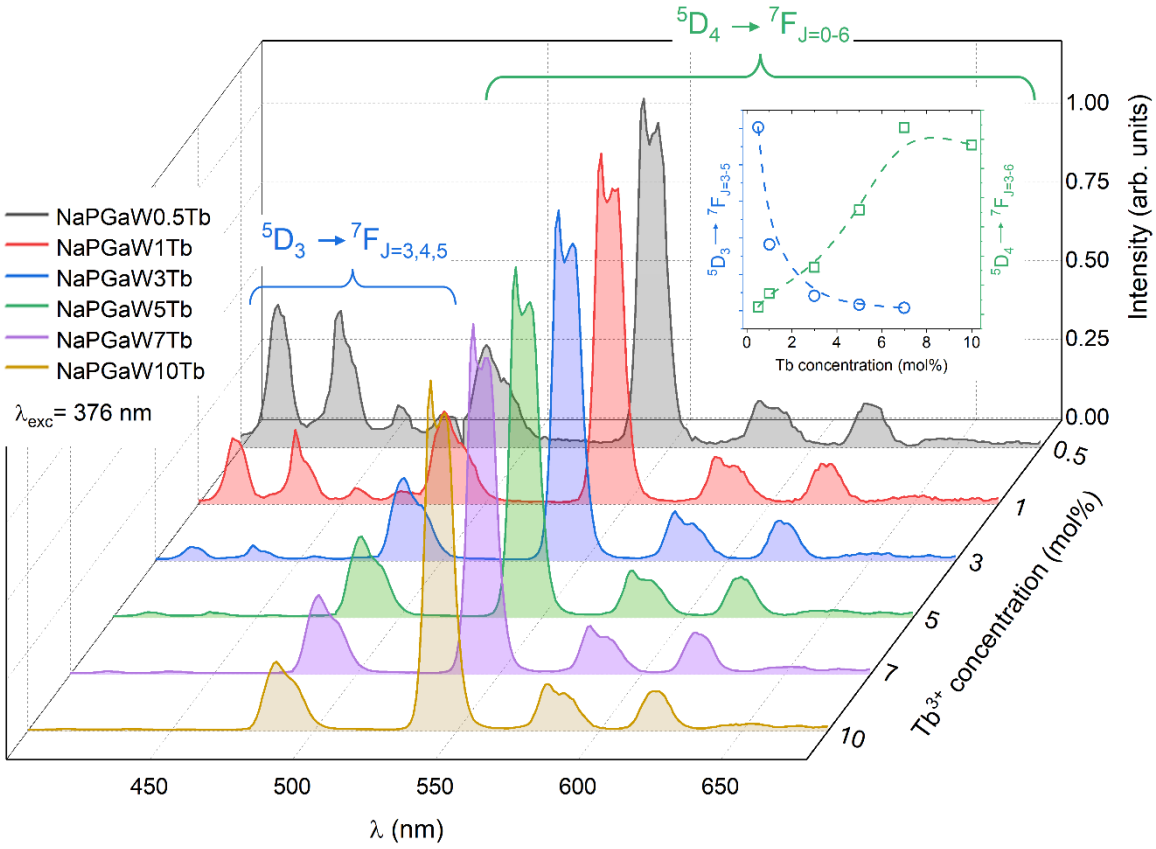

As discussed above, the glasses present variations of the relative emissions intensities depending on the doping content. The CIE 1931 coordinates of the Tb^{3+}-doped NaPGaW glasses were computed, as illustrated in Fig. 9 and Table 2. With a change in the Tb^{3+} ion concentration in the range of 0.5–10 mol%, the color coordinates of the samples were tuned from (0.2606, 0.38533) to (0.3261, 0.6042), namely, multicolor emissions could be achieved. Notably, the emitting-color of the samples gradually changes from blue to green, with an increase in the Tb^{3+} ion content. The CIE chromaticity coordinate of NaPGaW7.0Tb is close to commercial fluorescent powder $MgAl_{11}O_{19}$:0.67Ce^{3+},0.33Tb^{3+} (0.3300, 0.5950), suggesting that NaPGaWTb can also be a potential candidate in the solid white light field.

Table 2. Tb population density (N_t), concentration dependence of the blue-to-green intensity ratio under 376 nm excitation (I_B/I_G), the CIE chromaticity coordinates (x,y), the decay times τ_3^{exp} ($^5D_4$), τ_4^{exp} ($^5D_3$) and the $^5D_4$-fluorescence quantum efficiency, η_3.

Tb^{3+} (mol)	**Tb^{3+} ($\times 10^{19}$ cm^{-3})**	**I_G/I_B**	**CIE (x,y)**	τ_3^{exp} (± 0.04) **ms**	τ_4^{exp} (± 0.03) **ms**	η_3 (± 0.09)
0.5	2.90	2.1	0.2606, 0.3853	2.59	0.82	1.0
1.0	5.80	5.0	0.2909, 0.4890	2.27	0.62	0.88
3.0	17.4	22.1	0.3152, 0.5722	2.07	0.31	0.80
5.0	29.8	54.5	0.3211, 0.5916	2.03	0.17	0.78
7.0	41.8	112	0.3238, 0.5987	1.84	0.11	0.71
10.0	61.3	*	0.3261, 0.6042	1.61	0.066	0.62

*The I_G/I_B ratio was not calculated because $I_B \rightarrow 0$.

Figure 9. CIE 1931 chromaticity diagram for Tb^{3+}-doped NaPGaW glasses under UV (376 nm) excitation.

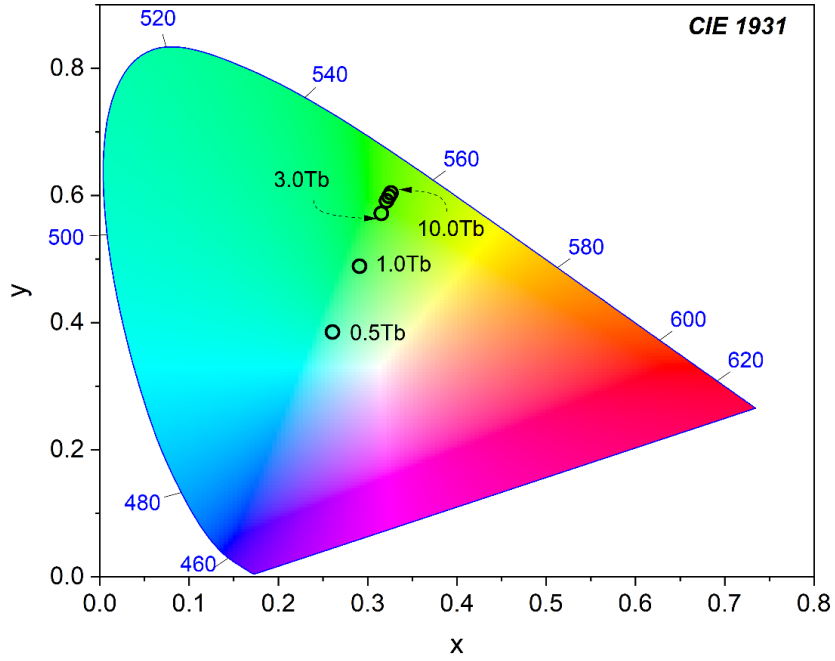

Fluorescence decay analysis is very helpful to understand the ET mechanisms and quenching behavior of Tb^{3+}-luminescence. Indeed, the fluorescence decay is determined by the addition of the radiative decay rate (A) to nonradiative processes due to ET processes (self-

quenching, multiphonon emission (W^{MP}), hydroxyl groups (OH^-) and other impurities)[48]. Thus, the measured lifetime (τ^{exp}) can be expressed as follows

$$\frac{1}{\tau^{exp}} = A + W^{ET} + W^{MP} + W^{OH} + \cdots \ldots \quad (2)$$

Experimental emission $^5D_4$ and $^5D_3$ decay under UV (376 nm) excitation are presented in Fig. 10(a) and (b), respectively. The effective lifetimes were obtained from the fluorescent decay curves, I (t), by:

$$\tau^{exp} = \frac{\int_0^\infty t\, I(t)\, dt}{\int_0^\infty I(t)\, dt} \quad (3)$$

The $^5D_4 \rightarrow {}^7F_5$ emission decay curves presented in Fig. 10(a), were well fit by a single exponential function for all doping concentrations up to 10 mol%. However, the lifetime values decrease from 2.59 to 1.61 ms when Tb^{3+} concentration increases from 0.5–10 mol%. Such a behavior of the $^5D_4$ excited state lifetime is due to the large population of this level, which increases the probability of energy migration. As a minor effect, it could also directly lead to losses, e.g., energy transfer to some other undesired impurity or defect. How- ever, the concentration dependence is weak, similarly to what was reported for Tb^{3+}-doped zinc phosphate [46] and fluoroborate [43] glasses. W^{MP} should be negligible due to the very large energy gap (~15000 cm^{-1}) below the $^5D_4$ level, corresponding to ~ 16-phonons considering the phonon cut-off frequency of the NaPGaW20 glass (~950 cm−1). Therefore, we can conclude that the experimentally observed lifetime in the Tb3+ zero-concentration limit (τ_{30}^{exp}) should be close to $^5D_4$ radiative lifetime, $\tau_3^{rad} \sim \tau_{30}^{exp}$ = (2.59 ± 0.05) ms. Consequently, the concentration dependence of the $^5D_4$ quantum efficiency can be estimated by $\eta_3 = \tau_3^{exp}/\tau_{30}^{exp}$, as shown in Table 2.

The decay curves from the $^5D_3$ (level 4 in Fig. 1), on the other hand, exhibit a clear non-exponential character, as shown in Fig. 10(b). Their effective lifetimes, τ_4^{exp}, decrease from 0.82 to 0.07 ms, upon increasing the Tb^{3+} concentration from 0.5 m to 10 mol%. A similar behavior was observed in most Tb^{3+} doped materials (crystal and glasses) and attributed to the CR process given by Eq.(1) depicted in Fig. 1.

Figure 10. Decay curves for (a) the $^5D_3 \rightarrow {}^7F_4$ emission and (b) for the $^5D_3 \rightarrow {}^7F_4$ emission of Tb^{3+}-doped NaPGaW glasses. Solid gray lines are given by Eq.(3).

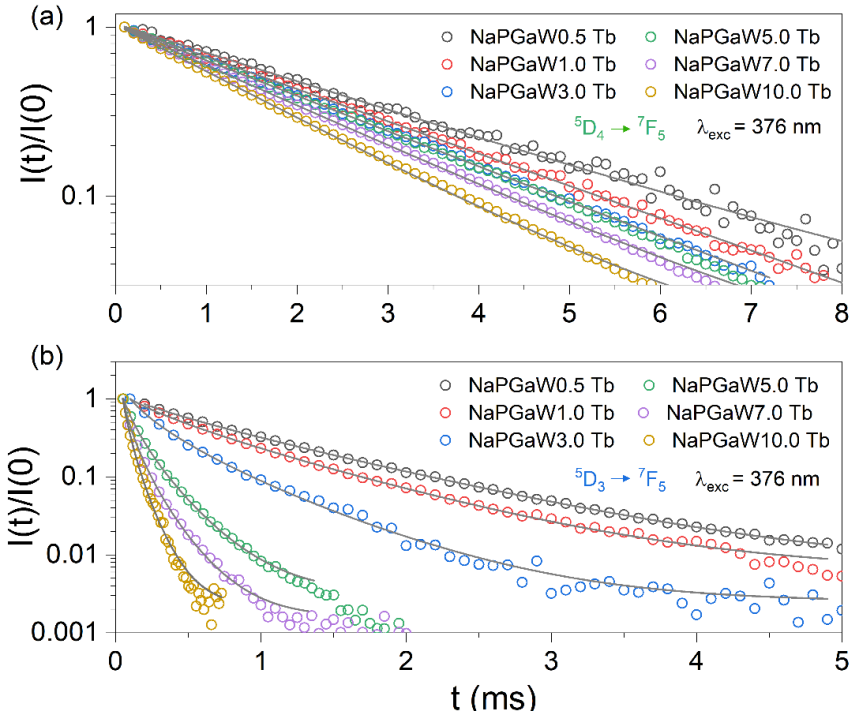

The decay curves can also provide some insight about the energy transfer microscopic parameters using the Inokuti–Hirayama (IH) model that assumes Tb^{3+} ions are randomly distributed in the glass structure [46,49–51]. For instance, considering $^5D_3$ - $^5D_4$ cross-relaxation, it is possible to obtain the critical distance R0 from the concentration quenching data. R_0 is defined as the critical separation between donor and acceptor at which the non-radiative rate equals to the radiative rate of the internal single-ion relaxation. According to IH model, fluorescence decay is given by [49].

$$I(t) = I_0 \exp\left[-\frac{t}{\tau_0^{IH}} - Q\left(\frac{t}{\tau_0^{IH}}\right)^{3/s}\right] \quad (4)$$

The first term (t/τ_0^{IH}) represents the emission of Tb^{3+} ions without ET processes, Q is an ET energy transfer parameter and s determines the nature of the involved electric multipole interaction (s = 6, 8, 10 corresponds to the electric dipole-dipole, dipole-quadrupole, and quadrupole-quadrupole interactions, respectively). $Q = \Gamma\left(1 - \frac{3}{s}\right)\frac{N_t}{N_0}$, where Γ is the Gamma

function, N_t is the number of acceptors per unit volume, N_0 is the volume of donor's sphere of influence and τ_0^{IH} is intrinsic lifetime.

Figure 11 shows the plot of $ln\left[-ln\left(\frac{I(t)}{I_0}\right)-\frac{t}{\tau_0^{IH}}\right]$ as a function of $ln\left(\frac{t}{\tau_0^{IH}}\right)^3$, which from Eq.(4) should yield a straight line with a slope of 1/*s*. From these fits, the average value of s = 6.2 ± 0.7 was obtained, close to 6 as expected for a dipole-dipole interaction and observed in most Tb^{3+} doped glasses [43,44,46,49]. Using s = 6 we have $Q=\sqrt{\pi}\frac{N_t}{N_0}$, resulting in N_0 = (1.23± 0.06) ×10^{20} cm^{-3}. In this paper N_t represents the Tb^{3+} ion concentration and the N_t/N_0 ratio indicates the number of acceptors in the donor's sphere of influence. Since $N_0= 3/(4\pi R_0^3)$ and the donor-acceptor ET parameter $C_{DA} = {R_0^6}/{\tau_0}$, we obtained R_0 = (18.0 ± 0.8) Å and C_{DA} = (4.5 ± 0.5) ×10^{-39} cm^6/s. These results are similar to the values obtained in Tb^{3+}-doped phosphate glasses [43].

Figure 11. Plots of experimental data $ln\left[-ln\left(\frac{I(t)}{I_0}\right)-\frac{t}{\tau_0^{IH}}\right]$ *versus* $ln\left(\frac{t}{\tau_0^{IH}}\right)^3$ relative to the blue emission. Solid gray lines are Inokuti–Hirayama (IH) curves fit given by Eq(4).

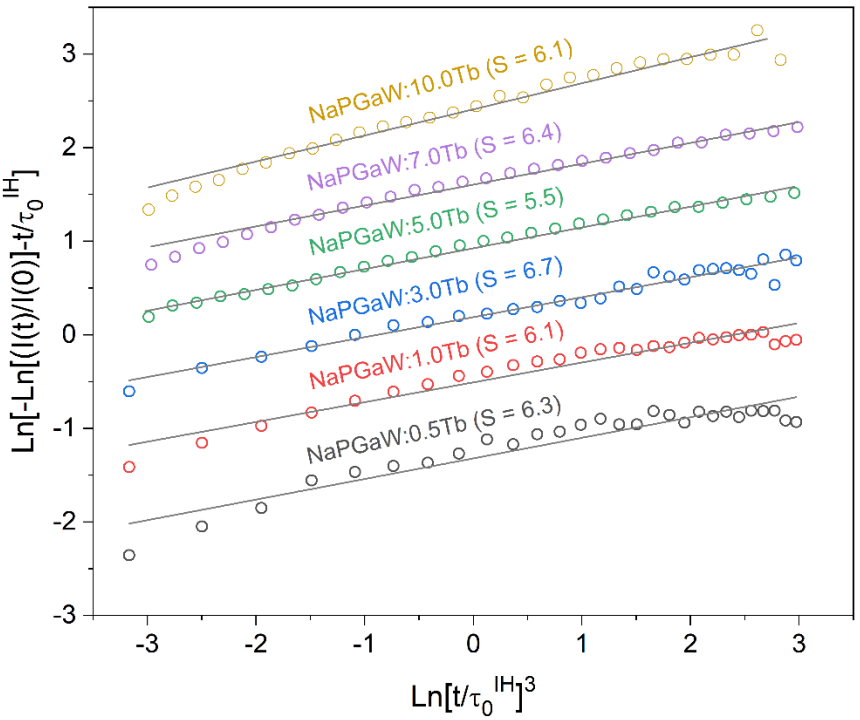

After this detailed analysis of the fluorescence decay, we can quantitatively analyze the link between the ratio I_G/I_B and the CR process (see Table 2 and Fig. 1). The luminescence ratio is given by

$$\left.\frac{I_G}{I_B}\right|_{lum} = \left(\frac{A_{31}+A_{32}}{A_{41}+A_{42}}\right).\left(\frac{N_3}{N_4}\right) \tag{5}$$

where A_{ij} is the radiative decay rate from levels $i \rightarrow j$ (Figure 4) and N_i is the level i population density. So, from rate equations we obtain:

$$\frac{N_3}{N_4} = \frac{W_{43}}{W_{3T}} = \frac{A_{43}+W_{43}^{*}+W_{43}^{CR}}{W_{3T}} \tag{6}$$

In Eq.(6) it was assumed that CR is the only process responsible for the concentration dependence of its fluorescence dynamics $^5D_3$ (level 4 in Fig. 1), while W_{43}^{*} is a concentration independent term, which can be attributed to phonons, OH^-, host impurities, etc.

The concentration dependence of the fluorescence decay is usually fitted by the empirical expression [48]

$$\tau_4^{exp} = \frac{\tau_{40}^{exp}}{1+\left(\frac{N_t}{N_c}\right)^p} \tag{7}$$

where τ_{40}^{exp} represents the zero-concentration limit of τ_4^{exp} and N_c the critical concentration. The parameters N_c and p are usually obtained from the fit of the experimental data. In this paper, we assumed that the total level 4 decay is given by $W_{4T} = \left(\tau_4^{exp}\right)^{-1} = A_4 + W_{43}^{*} + W_{43}^{CR}$. Since W_{43}^{CR} is the only contribution to W_{4T} responsible for its concentration dependence, from Eq.(7) we can infer that $W_{43}^{CR} = (A_4 + W_{43}^{*})(N_t/N_c)^{p/3}$. It should be noticed that level 4 fluorescence quantum efficiency can be estimated by $\eta_4 = \tau_4^{exp}.A_4$. Therefore, from Eq.(4)-(6), we obtained:

$$\frac{I_G}{I_B} = \frac{\eta_3}{1-\beta_{43}}\left[\beta_{43} + \frac{W_{43}^{*}}{A_4} + \eta_{04}^{-1}.\left(\frac{N_t}{N_c}\right)^p\right] \tag{8}$$

where $\beta_{43} = A_{43}/A_4$ represents the branching ratio of the $^5D_3 \rightarrow {}^5D_4$ transition, η_3 and η_4 are level 3 and 4 quantum efficiencies, respectively, η_{40} represents the zero-concentration limit of η_4 given by $\eta_{04}^{-1} = (A_4 + W_{43}^*)/A_4$.

In the literature of RE^{3+}-doped materials the Judd–Ofelt (JO) method has been applied successfully to determine the radiative lifetime in several important cases [48]. However, we could not obtain reliable JO calculations in our glasses due to the strong overlapping of the UV absorption lines with the broadband associated with the charge transfer in tungstate groups and the glass UV edge. In fact, there are very few detailed and reliable JO analyses in the literature of Tb^{3+} doped materials [50], since at higher energies the 4f → 4f transitions are superimposed on more intense absorption bands which arise from $4f^n \rightarrow 4f^{n-1}5d$ transitions. However, Yamashita and Ohishi [21] obtained $\beta_{43} \sim 0.05$ for Tb^{3+}-doped borosilicate glasses, which is the biggest β_{43} value we found in the literature for Tb^{3+} doped materials. Therefore, in order to fit the experimental that we assumed $\beta_{43} << 1$, in Eq.(8) to obtain:

$$\eta_3^{-1}.\frac{I_G}{I_B} \sim \beta_{43} + \frac{W_{43}^*}{A_4} + \eta_{04}^{-1}.\left(\frac{N_t}{N_c}\right)^p \qquad (9)$$

where $(\beta_{43} + W_{43}^* / A_4) = \left.\frac{I_G}{I_B}\right|_0$ represents the zero-concentration limit of $\frac{I_G}{I_B}$. Figure 11 shows the concentration dependence of τ_4^{exp} and $\frac{I_G}{I_B}$, fit by Eqs. (7) and (9), respectively. These fits were performed imposing the same N_c and p values for both fit curves, since our model establish a link between these data. The fit curves in Fig. 12 resulted in N_c = (1.04 ± 0.07)×10^{20} ions.cm^{-3}, p = (1.9 ± 0.1), τ_{40}^{exp} = (1.1 ± 0.1) ms and $\left.\frac{I_G}{I_B}\right|_0$ = 2.0 ± 0.4. These values are in good agreement with N_0 = (1.2± 0.2) × 10^{20} cm^{-3}, τ_0^{IH} = (1.05 ± 0.07) ms, and s/3 = (2.1 ± 0.2), respectively; obtained previously by IH analysis (Fig.10). Since we expect that $\beta_{43} \ll 1$ then $W_{43}^*/A_4 \sim 2.0$, $\eta_{04} \sim [1 + W_{43}^*/A_4]^{-1} \sim 0.33$ and $A_4 \sim \eta_{04}/\tau_{40}^{exp}$ = 300 s^{-1}. These results are very interesting because allow us to estimate $\eta_4 = A_4\,\tau_4^{exp}$.

Figure 12. $1/\tau_4$ (black square) and $(I_G/I_B)h_3$ (red circle) Tb concentration dependence fitted by Eq. (7) and (9), respectively.

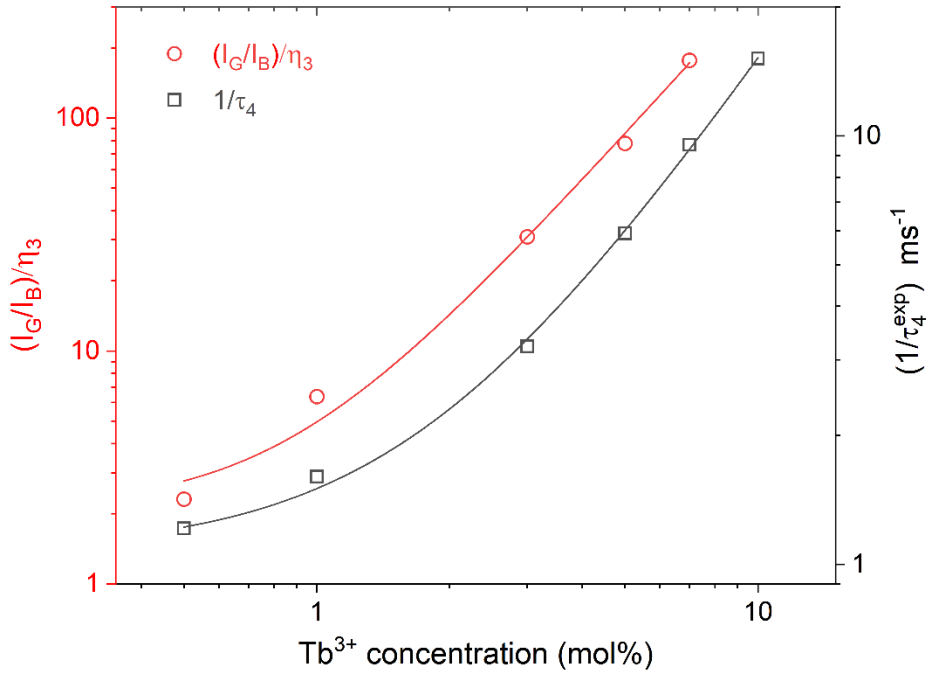

It is interesting to remark that in order to estimate η_3 in Table 2, we assumed that $\tau_3^{rad} \sim \tau_{30}^{exp}$, which appears to be a reasonable assumption due to the large energy gap below $^5D_4$ level. However, the above analyses of $\frac{I_G}{I_B}\Big|_0$ reveals that this assumption is not valid for the $^5D_3$ level since we estimated $\tau_4^{rad} \sim 3.1\ \tau_{40}^{exp}$. The main difference is the energy gaps bellow $^5D_3$ is ~2.6 smaller than $^5D_4$. This affects not only the phonon decay rate (W^{MP}) but also quenching by hydroxyl. Only two OH^- vibrations are required to cover the $^5D_3 \rightarrow {}^5D_4$ decay. For instance, Y. Wang et.al. [52] observed a monotonic increase of I_G/I_B with the absorption coefficient at 3500 cm^{-1} (α_{OH}). This behavior is in agreement with Eq.(9) considering that $W_{43}^* \sim W^{MP} + W^{OH}$, where W^{OH} is supposed to increase linearly with α_{OH}. Also in sol-gel glasses, the I_G/I_B ratio was used to monitor the fluorescence yield of the $^5D_3$ level with the effect drying agents (to eliminate OH^-) and Al^{3+} co-doping [53]. In fact several papers used I_G/I_B only as a qualitative parameter while this paper allows a quantitative analysis by Eq.(7-9).

Figure 13 presents the XEL spectra of the NaPGaW:Tb^{3+} glasses. The shape of the characteristic emission peaks is very similar to what was observed for excitation in the UV, as shown in Figure 7. Nevertheless, the interaction mechanism of X-ray excitation differs substantially from that of UV excitation, which explains the difference of emission quenching

observed in the XEL spectra. While upon excitation with UV radiation the excitation energy is transferred directly to the Tb^{3+} ions, in the scintillation process, some steps occur before the rare-earth ion emission [54]. These steps are complex, but they are usually simplified into three consecutive ones. In the first step, *conversion*, the host absorbs the high-energy particle creating electrons and holes. In the second step, known as *migration*, electrons and holes will migrate through the conduction and valence bands and a fraction of excited electrons and holes recombine at the luminescence centers. This recombination can be radiative, when scintillation occurs, or non-radiative when the energy is lost into heat. This step is called the relaxation [2,5]. RL intensity continuously increases for higher Tb concentrations, as shown in the inset of Fig. 13. In the same way, as in the case of the NaPGaW20 glass, the emission of the Tb3+ doped samples under UV and X-ray excitation match well with CCD detectors and silicon photomultipliers.

Figure 13. RL spectra of Tb^{3+} doped gallium tungsten-phosphate glasses. The inset shows the integrated intensity of the $^5D_4 \rightarrow {}^7F_5$ emission line as a function of Tb concentration.

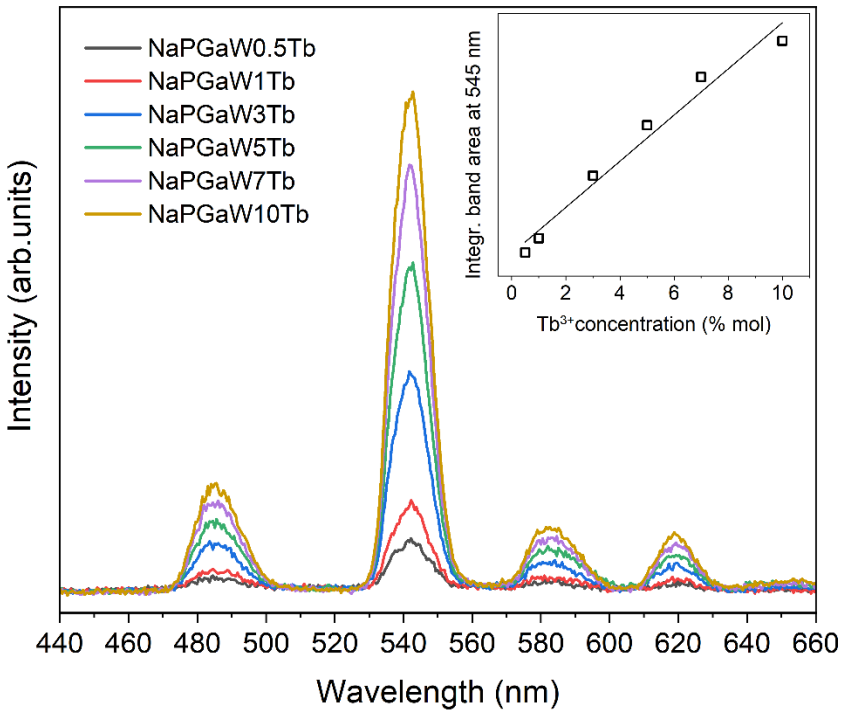

6.4 Conclusions

Undoped and Tb^{3+} doped gallium tungsten-phosphate glasses have been successfully synthesized by the conventional melt-quenching technique with excellent chemical stability and optical quality. Both, undoped and Tb^{3+}-doped samples present molar density values that are similar or superior to those of commercially available scintillators. The undoped glass presents a broad visible emission (400-750 nm) under UV light and X-ray excitation, ascribed to the radiative decay of STE, characteristic of the tungstate's groups. The doped glasses show intense emissions in the blue-green region and the I_G/I_B depends on the Tb^{3+} concentration. The CIE chromaticity coordinate of the Tb^{3+}-doped NaPGaW glasses were computed. The coordinates tuned from (0.2606, 0.38533) to (0.3261, 0.6042), with an increase in the Tb^{3+} ion content. The chromaticity coordinate of NaPGaW7.0Tb is close to that of the commercial fluorescent powder $MgAl_{11}O_{19}$:$0.67Ce^{3+}$,$0.33Tb^{3+}$ (0.3300, 0.5950), suggesting that NaPGaWTb is a potencial candidate for white lighting application. The decay curves of the $^5D_3$ level are found to be non-exponential in nature for all the studied concentrations due to ion-ion energy transfer through cross-relaxation. The lifetime values are in the range 2.6 to 1.6 ms decreasing for higher Tb concentration. The critical Tb–Tb distance R_c = 18 Å was estimated using the IH-model. It was found that the dipole-dipole interaction mechanism dominates in this glass. This R_c value is similar to values previously reported in other Tb^{3+} doped glasses. A simple model was applied to correlate the I_G/I_B change with the $^5D_3$ fluorescence concentration quenching. This model allows a quantitative estimation of the fluorescence quantum yield of the $^5D_3$ levels without the need of Judd-Ofelt calculations, which are difficult to obtain in Tb^{3+} doped glasses. Despite the presence of the cross-relaxation energy transfer, the optimum concentrations of dopant was determined to be around 7 mol% under UV excitation. From the viewpoint of scintillation, the glasses do not present luminescence quenching (at least up to 10 mol% Tb doping). These results indicate that both, undoped and doped glasses might be a promising alternative as an X-ray scintillating for slow events.

AUTHORS CONTRIBUTIONS

TAL e JFMS contributed equally to this manuscript. **Thiago A. Lodi:** Conceptualization, Methodology, Investigation, Data curation, Writing- Original draft preparation.: **Jéssica F. M. dos Santos:** Conceptualization, Investigation, Data curation, Formal analysis, Writing - Original draft preparation. **Gustavo Galleani:** Conceptualization, Investigation, Writing - Reviewing and Editing. **Luis G. Jacobsohn:** Data curation, Writing- Reviewing and Editing. **Tomaz Catunda:** Investigation, Writing- Reviewing and Editing, Supervision. **Andrea S. S. de Camargo:** Conceptualization, Writing- Reviewing and Editing, Supervision.

ACKNOWLEDGMENTS

Authors would like to acknowledge the Brazilian funding agencies FAPESP - Fundação de Amparo à Pesquisa do Estado de São Paulo (Process number 2013/07793-6, CEPID program); CAPES - Coordenação de Aperfeiçoamento de Pessoal de Nível Superior; CNPq - Conselho Nacional de Desenvolvimento Científico e Tecnológico (Universal project 130562/2018-1) and GG acknowledges funding by FAPESP, (grant number 2018/03931-9). L.G. Jacobsohn's contribution was supported by the National Science Foundation under Grant No. 1653016.

REFERENCES

[1] P. Lecoq, A. Gektin, M. Korzhik, Inorganic Scintillators for Detector Systems, Second edi, Springer, Berlim, Germany, 2017.

[2] G. Bizarri, Scintillation mechanisms of inorganic materials: From crystal characteristics to scintillation properties, J. Cryst. Growth. 312 (2010) 1213–1215. https://doi.org/10.1016/j.jcrysgro.2009.12.063.

[3] C. Dujardin, E. Auffray, E. Bourret, P. Dorenbos, P. Lecoq, M. Nikl, A. N.Vasil'ev, A. Yoshikawa, R. Zhu, NEEDS, TRENDS and ADVANCES IN INORGANIC SCINTILLATORS, IEEE Trans. Nucl. Sci. 65 (2018) 1977–1997. https://doi.org/10.1109/TNS.2018.2840160.

[4] M.J. Weber, Inorganic scintillators: Today and tomorrow, J. Lumin. 100 (2002) 35–45. https://doi.org/10.1016/S0022-2313(02)00423-4.

[5] T. Yanagida, Inorganic scintillating materials and scintillation detectors, Proc. Jpn. Acad. 94 (2018) 75–97. https://doi.org/10.2183/pjab.94.007.

[6] T. Yanagida, Study of rare-earth-doped scintillators, Opt. Mater. (Amst). 35 (2013) 1987–1992. https://doi.org/10.1016/j.optmat.2012.11.002.

[7] R.J. Ginther, J.H. Schulman, Glass Scintillators, IRE Trans. Nucl. Sci. 5 (1958) 92–95. https://doi.org/10.1109/TNS2.1958.4315633.

[8] X. Sun, M. Gu, M. Zhang, S. Huang, Influence of CeO_2 on scintillating properties of Tb^{3+}-doped silicate glasses, J. Rare Earths. 28 (2010) 340–344. https://doi.org/10.1016/S1002-0721(09)60267-2.

[9] J.C. Filho, S.C. Zilio, D.N. Messias, V. Pilla, A.C. Almeida Silva, N.O. Dantas, A.A. Andrade, Effects of aluminum substitution by potassium in the P_2O_5–Al_2O_3–Na_2O–K_2O phosphate glasses, J. Alloys Compd. 815 (2020). https://doi.org/10.1016/j.jallcom.2019.152359.

[10] I.C. Pinto, G. Galleani, L.G. Jacobsohn, Y. Ledemi, Y. Messaddeq, A.S.S. de Camargo, Fluorophosphate glasses doped with Eu^{3+} and Dy^{3+} for X-ray radiography, J. Alloys Compd. 863 (2021) 158382. https://doi.org/10.1016/j.jallcom.2020.158382.

[11] M.W. Kielty, L. Pan, M.A. Dettmann, V. Herrig, U. Akgun, L.G. Jacobsohn, Luminescence of Ce- doped aluminophosphate glasses, J. Mater. Sci. Mater. Electron. 30 (2019) 16774–16780. https://doi.org/10.1007/s10854-019-01301-4.

[12] J.C. Knowles, K. Franks, I. Abrahams, Investigation of the solubility and ion release in the glass system K_2O-Na_2O-CaO-P_2O_5, Biomaterials. 22 (2001) 3091–3096. https://doi.org/10.1016/S0142-9612(01)00057-6.

[13] G. Li, C. Zhang, P. Song, P. Zhu, K. Zhu, J. He, Luminescence properties in Tb^{3+}/Yb^{3+} codoped phosphate glasses for solar cells, J. Alloys Compd. 662 (2016) 89–93. https://doi.org/10.1016/j.jallcom.2015.12.074.

[14] S.M. Salem, Dielectric properties, conductivity, UV-visible and infrared spectroscopy of PbO P_2O_5 NaF glasses containing WO_3, J. Non. Cryst. Solids. 358 (2012) 1410–1416. https://doi.org/10.1016/j.jnoncrysol.2012.03.020.

[15] A. Łapa, M. Cresswell, I. Campbell, P. Jackson, W.H. Goldmann, R. Detsch, A.R. Boccaccini, Gallium- and Cerium-Doped Phosphate Glasses with Antibacterial Properties for Medical Applications, Adv. Eng. Mater. 22 (2020) 1901577. https://doi.org/10.1002/adem.201901577.

[16] M.S. Sadeq, B.O. El-bashir, A.H. Almuqrin, M.I. Sayyed, The tungsten oxide within phosphate glasses to investigate the structural, optical, and shielding properties variations, J. Mater. Sci. Mater. Electron. 32 (2021) 12402–12413. https://doi.org/10.1007/s10854-021-05871-0.

[17] A.M. Deliormanlı, Synthesis and characterization of cerium- and gallium-containing borate bioactive glass scaffolds for bone tissue engineering, J. Mater. Sci. Mater. Med. 26 (2015) 67. https://doi.org/10.1007/s10856-014-5368-0.

[18] J. Ren, H. Eckert, Intermediate role of gallium in oxidic glasses: Solid state NMR structural studies of the Ga_2O_3-$NaPO_3$ system, J. Phys. Chem. C. 118 (2014) 15386– 15403. https://doi.org/10.1021/jp504023k.

[19] N. Wantana, E. Kaewnuam, B. Damdee, S. Kaewjaeng, S. Kothan, H.J. Kim, J. Kaewkhao, Energy transfer based emission analysis of Eu^{3+} doped Gd_2O_3-CaO-SiO_2-B_2O_3 glasses for laser and X-rays detection material applications, J. Lumin. 194 (2018) 75–81. https://doi.org/10.1016/j.jlumin.2017.10.004.

[20] C.C. Lin, W.T. Chen, C.I. Chu, K.W. Huang, C.W. Yeh, B.M. Cheng, R.S. Liu, UV/VUV switch-driven color-reversal effect for Tb-activated phosphors, Light Sci. Appl. 5 (2016) e16066-6. https://doi.org/10.1038/lsa.2016.66.

[21] T. Yamashita, Y. Ohishi, Concentration and temperature effects on the spectroscopic properties of Tb^{3+} doped borosilicate glasses, J. Appl. Phys. 102 (2007) 123107. https://doi.org/10.1063/1.2821789.

[22] Q. Chen, D. Valiev, S. Stepanov, J. Ding, L. Liu, C. Li, H. Lin, Y. Zhou, F. Zeng, Influence of the Tb^{3+} concentration on the luminescent properties of high silica glass, Opt. Mater. (Amst). 86 (2018) 606–610. https://doi.org/10.1016/j.optmat.2018.10.008.

[23] K. Linganna, V.B. Sreedhar, C.K. Jayasankar, Luminescence properties of Tb^{3+} ions in zinc fluorophosphate glasses for green laser applications, Mater. Res. Bull. 67 (2015) 196–200. https://doi.org/10.1016/j.materresbull.2015.02.062.

[24] G.B. Spector, T. McCollum, A.R. Spowart, Advances in terbium-doped, lithium-loaded scintillator glass development, Nucl. Inst. Methods Phys. Res. A. 326 (1993) 526–530. https://doi.org/10.1016/0168-9002(93)90855-C.

[25] S. Jia, L. Huang, D. Ma, Z. Tai, S. Zhao, D. Deng, H. Wang, G. Jia, Y. Hua, Q. Yang, S. Xu, Luminescence properties of Tb^{3+}-doped oxyfluoride scintillating glasses, J. Lumin. 152 (2014) 241–243. https://doi.org/10.1016/j.jlumin.2013.12.036.

[26] N. Wantana, E. Kaewnuam, Y. Ruangtaweep, D. Valiev, S. Stepanov, K. Yamanoi, H.J. Kim, J. Kaewkhao, Radio, cathodo and photoluminescence investigations of high density WO_3-Gd_2O_3-B_2O_3 glass doped with Tb^{3+}, Radiat. Phys. Chem. 164 (2019) 108350. https://doi.org/10.1016/j.radphyschem.2019.108350.

[27] S. QIAN, L. HUANG, S. ZHAO, S. XU, Luminescent properties of Tb^{3+} doped high density borogermanate scintillating glasses, J. Rare Earths. 35 (2017) 787–790. https://doi.org/10.1016/S1002-0721(17)60977-3.

[28] X.Y. Sun, Q.M. Yang, P. Gao, H.S. Wu, P. Xie, Luminescence, energy transfer properties of Tb^{3+}/Gd^{3+}-coactivated oxyfluoride borogermanate scintillating glasses, J. Lumin. 165 (2015) 40–45. https://doi.org/10.1016/j.jlumin.2015.04.021.

[29] C.W.E. van E. Delft, Inorganic scintillators in medical imaging, Phys. Med. Biol. 85 (2002) R85–R106. https://doi.org/10.1016/S0168-9002(03)01542-0.

[30] Y. Zou, W. Zhang, C. Li, Y. Liu, H. Luo, Construction and test of a single sphere neutron spectrometer based on pairs of ^{6}Li-and ^{7}Li-glass scintillators, Radiat. Meas. 127 (2019) 106148. https://doi.org/10.1016/j.radmeas.2019.106148.

[31] D. Manzani, R.G. Fernandes, Y. Messaddeq, S.J.L. Ribeiro, F.C. Cassanjes, G. Poirier, Thermal, structural and optical properties of new tungsten lead-pyrophosphate glasses, Opt. Mater. (Amst). 33 (2011) 1862–1866. https://doi.org/10.1016/j.optmat.2011.02.041.

[32] M. Nalin, G. Poirier, S.J.L. Ribeiro, Y. Messaddeq, L. Cescato, Glasses in the $SbPO_4$ - WO_3 system, J. Non. Cryst. Solids. 353 (2007) 1592–1597. https://doi.org/10.1016/j.jnoncrysol.2007.01.031.

[33] T. Scheike, H. Segawa, S. Inoue, Y. Wada, Blue luminescence in the WO_3-P_2O_5-ZnO glass system, Opt. Mater. (Amst). 34 (2012) 1488–1492. https://doi.org/10.1016/j.optmat.2012.03.014.

[34] H. Wen, B. Cheng, P.A. Tanner, Optical properties of selected 4d and 5d transition metal ion-doped glasses, RSC Adv. 7 (2017) 26411–26419. https://doi.org/10.1039/C7RA04062H.

[35] V.N. Kolobanov, I.A. Kamenskikh, V. V. Mikhailin, I.N. Shpinkov, D.A. Spassky, B.I. Zadneprovsky, L.I. Potkin, G. Zimmerer, Optical and luminescent properties of anisotropic tungstate crystals, Nucl. Instruments Methods Phys. Res. Sect. A Accel. Spectrometers, Detect. Assoc. Equip. 486 (2002) 496–503. https://doi.org/10.1016/S0168-9002(02)00760-X.

[36] M. V. Korzhik, V.B. Pavlenko, T.N. Timoschenko, V.A. Katchanov, A. V. Singovskii, A.N. Annenkov, V.A. Ligun, I.M. Solskii, J.P. Peigneux, Spectroscopy and origin of radiation centers and scintillation in $PbWO_4$ single crystals, Phys. Status Solidi Appl. Res. 154 (1996) 779–788. https://doi.org/10.1002/pssa.2211540231.

[37] R. Leonelli, J.L. Brebner, Time-resolved spectroscopy of the visible emission band in strontium titanate, Phys. Rev. B. 33 (1986) 8649–8656. https://doi.org/10.1103/PhysRevB.33.8649.

[38] E. Orhan, F.M. Pontes, C.D. Pinheiro, E. Longo, P.S. Pizani, J.A. Varela, E.R. Leite, T.M. Boschi, A. Beltrán, J. Andrés, Theoretical and experimental study of the relation between photoluminescence and structural disorder in barium and strontium titanate thin films, J. Eur. Ceram. Soc. 25 (2005) 2337–2340. https://doi.org/10.1016/j.jeurceramsoc.2005.03.053.

[39] L.S. Cavalcante, M.F.C. Gurgel, A.Z. Simões, E. Longo, J.A. Varela, M.R. Joya, P.S. Pizani, Intense visible photoluminescence in Ba ($Zr_{0.25}Ti_{0.75}$)O_3 thin films, Appl. Phys. Lett. 90 (2007) 14–17. https://doi.org/10.1063/1.2425013.

[40] M. Itoh, T. Katagiri, T. Aoki, M. Fujita, Photo-stimulated luminescence and photoinduced infrared absorption in $ZnWO_4$, Radiat. Meas. 42 (2007) 545–548. https://doi.org/10.1016/j.radmeas.2007.01.049.

[41] L. Wang, Y. Ma, H. Jiang, Q. Wang, C. Ren, X. Kong, J. Shi, J. Wang, Luminescence properties of nano and bulk $ZnWO_4$ and their charge transfer transitions, J. Mater. Chem. C. 2 (2014) 4651–4658. https://doi.org/10.1039/c4tc00245h.

[42] P. Pavan, G. Zanella, R. Zannoni, P. Polato, Radiation damage and annealing of scintillating glasses, Nucl. Inst. Methods Phys. Res. B. 61 (1991) 487–490. https://doi.org/10.1016/0168-583X(91)95326-9.

[43] T.O. Sales, R.J. Amjad, C. Jacinto, M.R. Dousti, Concentration dependent luminescence and cross-relaxation energy transfers in Tb^{3+} doped fluoroborate glasses, J. Lumin. 205 (2019) 282–286. https://doi.org/10.1016/j.jlumin.2018.09.031.

[44] A.D. Sontakke, K. Biswas, K. Annapurna, Concentration-dependent luminescence of Tb^{3+} ions in high calcium aluminosilicate glasses, J. Lumin. 129 (2009) 1347–1355. https://doi.org/10.1016/j.jlumin.2009.06.027.

[45] J.F.M. Dos Santos, I.A.A. Terra, N.G.C. Astrath, F.B. Guimarães, M.L. Baesso, L.A.O. Nunes, T. Catunda, Mechanisms of optical losses in the $^5D_4$ and $^5D_3$ levels in Tb^{3+} doped low silica calcium aluminosilicate glasses, J. Appl. Phys. 117 (2015). https://doi.org/10.1063/1.4906781.

[46] C.R. Kesavulu, A.C. Almeida Silva, M.R. Dousti, N.O. Dantas, A.S.S. De Camargo, T. Catunda, Concentration effect on the spectroscopic behavior of Tb^{3+} ions in zinc phosphate glasses, J. Lumin. 165 (2015) 77–84. https://doi.org/10.1016/j.jlumin.2015.04.012.

[47] D. De Graaf, S.J. Stelwagen, H.T. Hintzen, G. De With, Tb^{3+} luminescence as a tool to study clustering of lanthanide ions in oxynitride glasses, J. Non. Cryst. Solids. 325 (2003) 29–33. https://doi.org/10.1016/S0022-3093(03)00324-7.

[48] W.J. Miniscalco, Optical and Electronic Properties of Rare Earth Ions in Glasses, in: Rare-Earth-Doped Fiber Lasers and Amplifiers, 2nd Edition, CRC Press, New York, 2001: p. 798. https://doi.org/https://doi.org/10.1201/9780203904657.

[49] M. Inokuti, F. Hirayama, Influence of energy transfer by the exchange mechanism on donor luminescence, J. Chem. Phys. 43 (1965) 1978–1989. https://doi.org/10.1063/1.1697063.

[50] J.F.M. dos Santos, V.S. Zanuto, A.C.C. Soares, E. Savi, L.A.O. Nunes, M.L. Baesso, T. Catunda, Evaluating the link between blue-green luminescence and cross-relaxation processes in Tb^{3+}-doped glasses, J. Lumin. 240 (2021) 118430. https://doi.org/10.1016/j.jlumin.2021.118430.

[51] K. Linganna, S. Ju, C. Basavapoornima, V. Venkatramu, C.K. Jayasankar, Luminescence and decay characteristics of Tb^{3+}-doped fluorophosphate glasses, J. Asian Ceram. Soc. 6 (2018) 82–87. https://doi.org/10.1080/21870764.2018.1442674.

[52] Y. Wang, S. Liu, J. Mao, X. Li, L. Li, H. Zeng, G. Chen, Study on mechanism controlling 5D3/5D4emissions of Tb^{3+} in glasses, J. Lumin. 185 (2017) 241–246. https://doi.org/10.1016/j.jlumin.2017.01.028.

[53] A.J. Silversmith, N.T.T. Nguyen, D.L. Campbell, D.M. Boye, C.P. Ortiz, K.R. Hoffman, Fluorescence yield in rare-earth-doped sol-gel silicate glasses, J. Lumin. 129 (2009) 1501–1504. https://doi.org/10.1016/j.jlumin.2009.03.026.

7 CONCLUSION

All glasses studied in this work were successfully synthesized by the melting-quenching technique with high stability and excellent optical quality. The structural studies indicate that the partial substitution of the $NaPO_3$ by Na_2WO_4 results in significant network reconstruction resulting in an increase in molar volume as well as a decreased oxygen packing density. An increase in Tg values is observed peaking for the compositions with x up = 10 to 15 while the thermal stability decreases when Na_2WO_4 is added at first and then increases with increasing Na_2WO_4 content. The solid-state NMR results indicate that the Q^1 units are successively depleted and found to be absent for the glasses with x above 10, and that the network is dominated by Q^0 units, connected to both gallium and tungstate species. The glass series synthesized to evaluate the intrinsic emission presented high optical transparency. The XPS analysis confirmed that the broad band emission observed for these samples in the visible region is attributed to the hexavalent tungsten of the WO_4^{2-} complexes.When exposed to cryogenic temperatures, the emission intensity of these NaPGaW glasses is enhanced. The Tb^{3+} doped NaPGaW glasses presented volumetric density values similar or superior to those of commercially available scintillators and show intense emissions in the blue-green with chromaticity coordinate of NaPGaW7.0Tb very close to that of the commercial fluorescent powder $MgAl_{11}O_{19}$:$0.67Ce^{3+}$,$0.33Tb^{3+}$ (0.3300, 0.5950). These findings suggest that NaPGaWTb can also be a promising candidate for white lighting application. The lifetime values are in the range 2.6 to 1.6 ms decreasing for higher Tb^{3+} dopant concentrations. Overall, the results indicate that undoped NaPGaW glasses are promising for application as extrinsic and cryogenic scintillators, while the Tb^{3+} doped glasses constitute a promising alternative for slow events X-ray scintillators.

LIST OF PUBLICATIONS (2018-2023)

Lodi, Thiago A.; Galleani, Gustavo; Merízio, Lennam G.; Oliveira Junior, Marcos; Santagneli, Silvia H.; Eckert, Hellmut; De Camargo, Andrea S.S. **Preparation, characterization, and structural studies of new sodium gallium tungstate phosphate glasses.** Journal of Non-crystalline Solids, v. 603, p. 122100, 2023.

Lodi, Thiago A.; Galleani, Gustavo; Merízio, Lennam G.; Mastelaro, Valmor, R.; De Camargo, Andrea S.S. **Tungsten Gallium-phosphate glasses as a promising intrinsic scintillator**. Journal of Non-crystalline Solids, v. 603, p. 122097, 2023.

Merízio, Lennam G.; Lodi, Thiago A.; Bonturim, Everton; De Camargo, Andrea S.S. **Persistent luminescent phosphor-in-glass composites based on $NaPO_3$ – Ga_2O_3 glasses loaded with $Sr_2MgSi_2O_7$:Eu^{2+}, Dy^{3+}.** Optical Materials, v. 134, p. 113046, 2022

Galleani, Gustavo; Lodi, Thiago A.; Mastelaro, Valmor, R.; Jacobsohn, Luiz G.; De Camargo, Andrea S.S. **Photoluminescence and X-ray induced Scintillation in Gd^{3+} -modified fluorophosphate glasses doped with Ce^{3+}.** Optical Materials, v. 133, p. 112934, 2022.

Lodi, Thiago A.; Dos Santos, Jéssica F.M.; Galleani, Gustavo; Jacobsohn, Luiz G.; Catunda, Tomaz; De Camargo, Andrea S.S. **Promising Tb^{3+}-doped Gallium Tungsten-phosphate glass Scintillator: Spectroscopy, energy transfer and UV/X-ray sensing**. Journal of Alloys and Compounds, v. 904, p. 164016, 2022.

Neto, Otávio. C. S.; Lodi, T. A.; Neto, João. G. O.; De Camargo, Andrea. S. S. ; Pedrochi, Franciana; Steimacher, Alysson. **Tunable Luminescence of Ce^{3+}-Doped Calcium Boroaluminate Glasses for Light Emitting Devices**. Journal of Electronic Materials, v. 50, p. 2378-2388, 2021.

Brito, Suzanny L. Lodi, Thiago A.; Muniz, Robson F.; Steimacher, Alysson; Pedrochi, Franciana. **Energy transfer investigation of Sm^{3+}/Eu^{3+} CaBAl glasses**. Journal of Luminescence, v. 219, p. 116947, 2020.

Lodi, Thiago A.; Dantas, Natacya F.; Gonçalves, Tassia S.; De Camargo, Andrea S.S.; Pedrochi, Franciana; Steimacher, Alysson. **Dy^{3+} doped calcium boroaluminate glasses and Blue Led for smart white light generation**. Journal of Luminescence, v. 207, p. 378-385, 2019.

Lodi, Thiago A.; Sandrini, Marcelo; Medina, Antonio N.; Barboza, Marcio J.; Pedrochi, Franciana; Steimacher, Alysson. **Dy:Eu doped CaBAl glasses for white light applications**. Optical Materials, v. 76, p. 231-236, 2018.

APPENDIX

Supporting Materials Section of: Preparation, characterization, and structural studies of new sodium gallium tungstate phosphate glasses

Figure S3. DSC spectrum of $0.5LiPO_3$-$0.5Na_2WO_4$ glass.

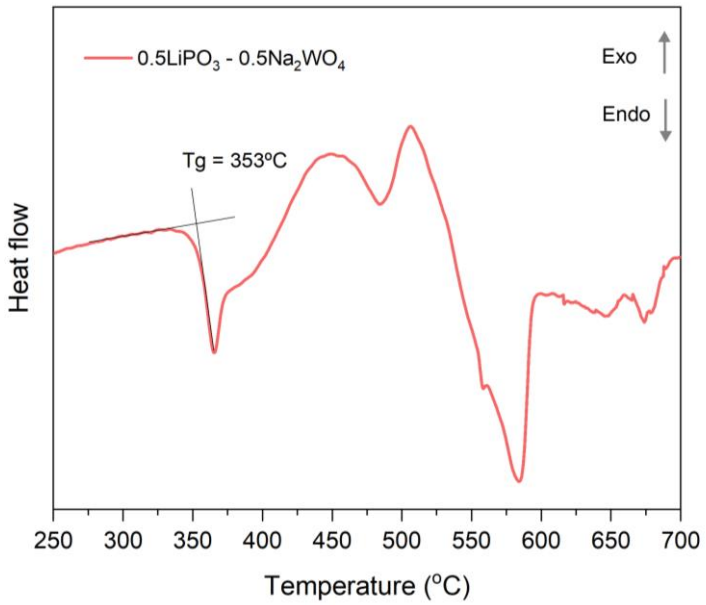

Figure S2. Photographs of of $(NaPO_3)_{80-x}(Ga_2O_3)_{20}(Na_2WO_4)_x$ (x = 0, 10 and 25 mol%) glass. under ambient light.

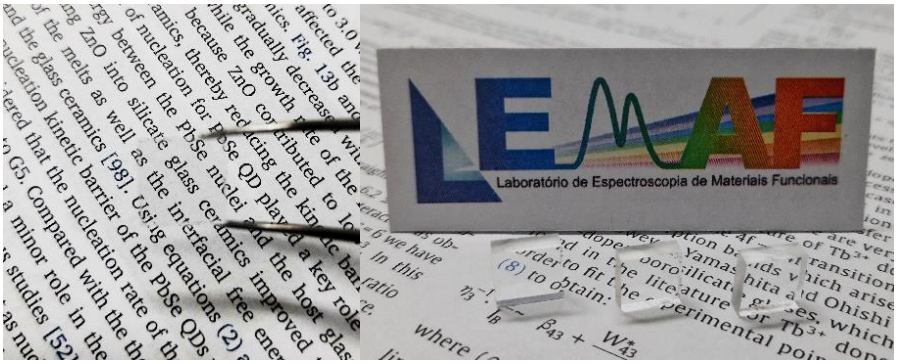

Figure S3. X-ray diffraction pattern of of $(NaPO_3)_{80-x}(Ga_2O_3)_{20}(Na_2WO_4)_x$ (x = 0, 5, 10, 15, 20 and 25 mol%) glasses.

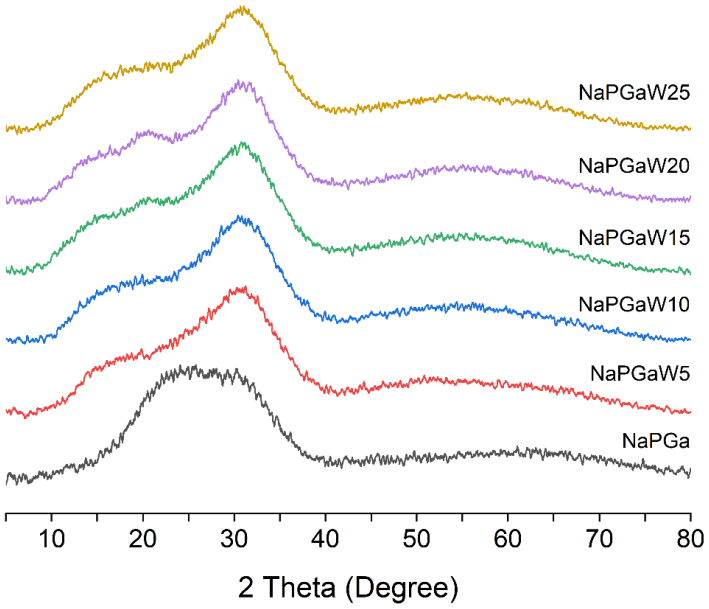

.

Figure S4. Tentative deconvolution of the Raman spectra of $(NaPO_3)_{80-x}(Ga_2O_3)_{20}(Na_2WO_4)_x$ (x = 0, 5, 10, 15, 20 and 25 mol%) glasses.

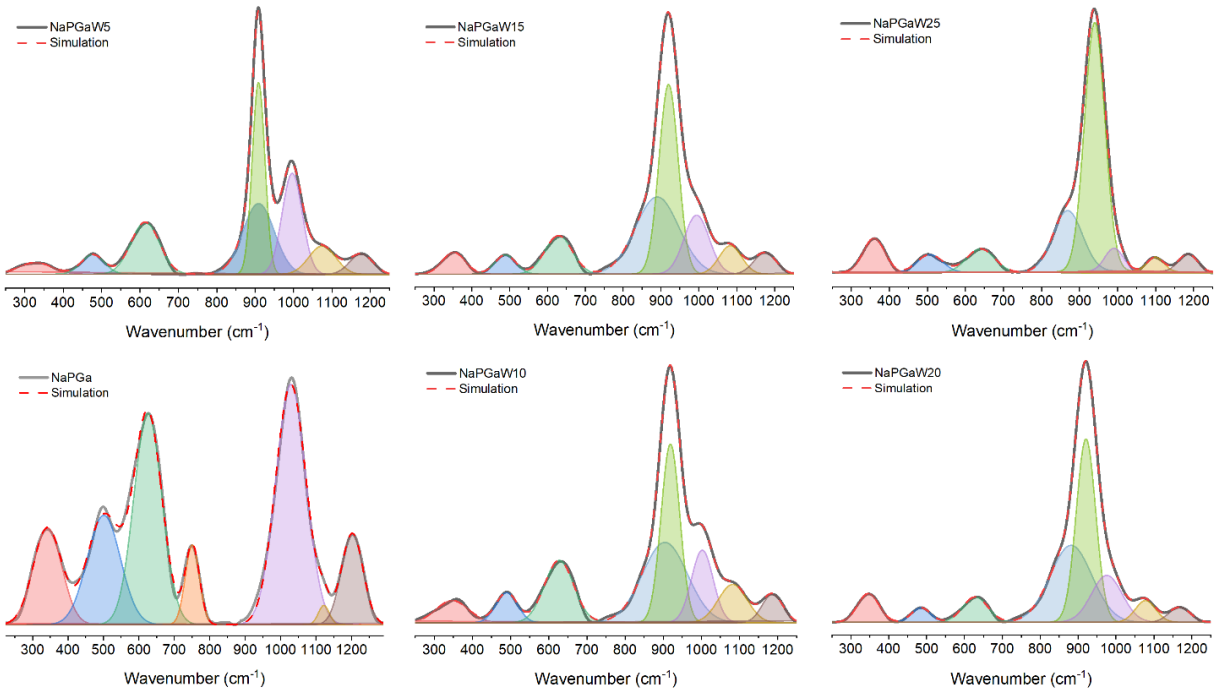

Figure S5. Deconvolution of the ^{31}P Refocused INADEQUATE spectrum of $(NaPO_3)_{80-x}(Ga_2O_3)_{20}$ glass with the parameters published in reference 7 and with the new set of parameters proposed in the present study.

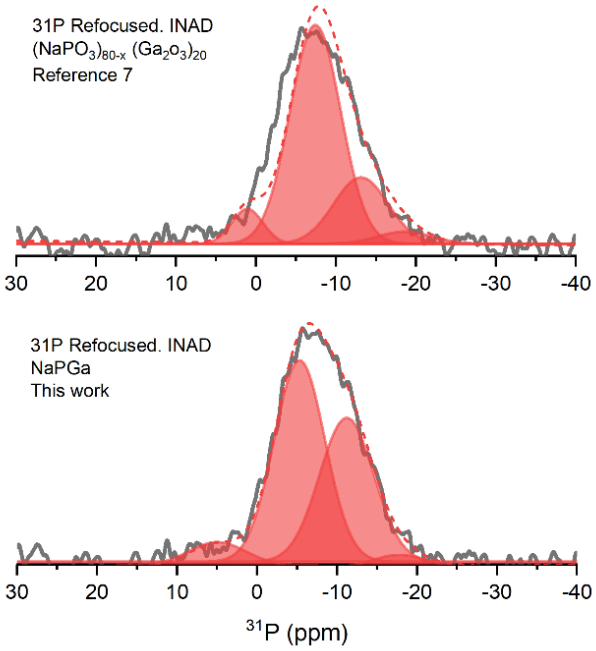

Figure S6. Percentage of Q^1 units in function of Na_2WO_4 content.

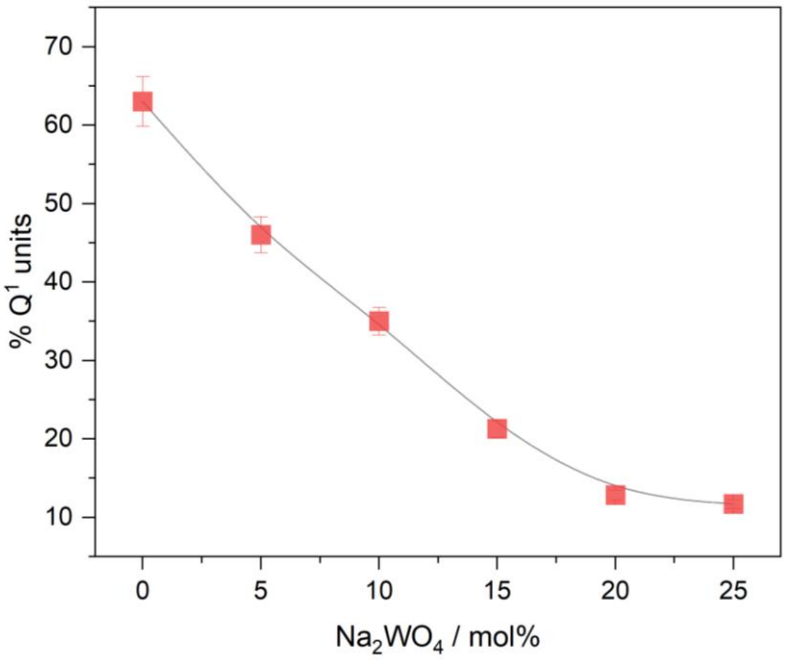

Supporting Materials Section of: Tungsten Gallium-phosphate glasses as a promising intrinsic scintillator

Figure S1. Decay curves of the NaPGaW5 (representative glass) and the pulsed laser (290 nm) at room temperature.

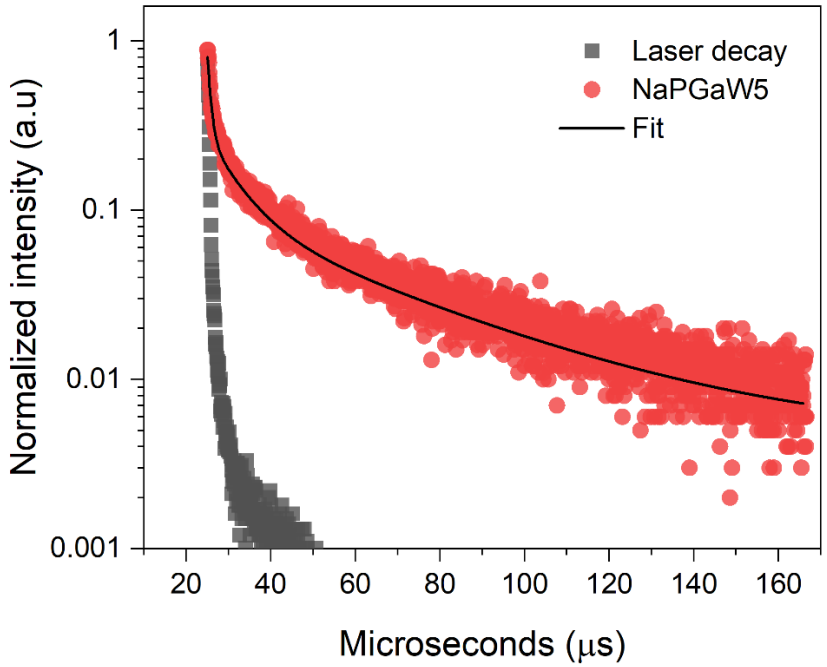

Figure S2. Comparison between the emission intensity of BGO crystal and NaPGaW5 glass.